Chemistry & Materials Science
Progress Report

Weapons Supporting Research
and
Laboratory Directed Research and Development

FY 1994

MASTER

DISCLAIMER

DISCLAIMER

Portions of this document may be illegible in electronic image products. Images are produced from the best available original document.

Contents

Group Projects _____ 31

Laboratory Directed Research and Development

Director's Initiatives _____ 59

Individual Projects _____ 67

Foreword

The research reported here in summary form was conducted during FY 1994 under the auspices of Weapons-Supporting Research (WSR) and Laboratory Directed Research and Development (LDRD).

WSR is an important source of discretionary funds to support fundamental research in the Chemistry and Materials Science (C&MS) Department. WSR provides the scientific and technological base required in the longer term for the success of the Weapons Program.

Administratively, work funded by WSR is organized into three categories:

- Block-funded programs ("thrust areas"), each of which typically involves several senior scientists in a coordinated, focused approach to a scientific or technological problem.
- Research groups consisting of two or three scientists.
- A few smaller projects led by individual investigators.

LDRD-funded work, which broadens the exploratory research base of C&MS, consists of several categories of discretionary research activities. Of these, Exploratory Research in the Directorates (ERD) and Director's Initiatives are included in this report. The former incorporates Exploratory Research in the Departments (Departmental), Exploratory Research in the Institutes, and Exploratory Research in the Programs (formerly SR).

The results reported here are for work in progress; as such, they may be preliminary, fragmentary, or incomplete. Before quoting or otherwise referring to any report herein, readers should consult one of its authors to obtain current information.

Jeffrey Wadsworth
Associate Director
Chemistry and Materials Science

Weapons-Supporting Research

Thrust Areas

Surface Science Research

L. L. Chase

Thrust Area Leader

Our research objectives are to investigate the growth, structure, and chemical reactivity of surfaces and thin films. The two main themes of our research are (1) growth, structure, and electronic properties of thin films and modified surface layers, and (2) interaction of surfaces and thin films with the environment.

The fullerenes, which are composed of cage structures of carbon atoms, have attracted much interest as surface reactants for thin-film deposition processes. Recent examples of these applications are the synthesis of diamond and silicon carbide films using the "buckeyball" molecule, C_{60}, as a reactive source of carbon. To understand and quantify the surface reaction mechanisms and rates for these new molecules, we are investigating the physical and chemical properties of C_{60} and other fullerene molecules on insulator, semiconductor, and metal surfaces. We are using in this research a molecular beam instrument that provides detailed information regarding these properties. One of the investigations on this topic in FY94 involves the dissociation of C_{60} on silica and graphite, leading to the deposition of carbon on the surfaces, accompanied by the ejection of C_{58} as a reaction product.

The detailed physical structure of surfaces can play an important role in determining their chemical and physical properties. New characterization methods offering higher sensitivity and spatial resolution are needed to complement existing techniques. In FY94, a unique combination of two probes of surface structure with very good spatial resolution—helium atom scattering and spot profile analysis of low-energy electron diffraction—was used to observe novel distortions of silver islands deposited onto the surfaces of silver crystals. This experiment, which was done in collaboration with a group in Julich, Germany, provides a more thorough evaluation of surface structure than could be obtained separately with either of these powerful techniques.

We have been developing methods for probing the magnetic properties of surfaces, interfaces, and thin films. Recent measurements of x-ray magnetic circular dichroism have been used to test calculations based on the single particle approximation, and exchange and spin-orbit splittings twice as large as those reported previously are deduced.

Other investigations in progress involve synthesis and electronic property measurements of nanometer-size silicon clusters, development of an ion-beam instrument to measure reaction parameters important for reactive etching of semiconductors, and deposition of SiC thin films using C_{60}.

Magnetic Linear and Circular Dichroism in Angular Resolved Iron $3p$ Core-Level Photoemission

E. Tamura, G. D. Waddill, J. G. Tobin, and P. A. Sterne

Introduction

Dichroism effects in core-level photoemission from ferromagnetic materials have attracted much interest since it was pointed out that the spectra yield a great deal of information on magnetic structures that can be further separated into spin and orbit contributions using spin-polarized detection.[1]

The magnetic anisotropy, which is especially important for surface magnetism, is determined to a large part by the orbital magnetic moment. So far, theories have been constructed for single atoms with partially occupied outer shells (d or f shells) or for materials well-described by a localized picture. Although many-electron effects can be easily and well described by this picture, multiple scattering effects by neighboring atoms are completely neglected in the photoexcitation process. Consequently, these theories would poorly explain experimental spectra when they are angle-resolved or surface sensitive. In this report, we show our new theoretical approach and numerical result for angle-resolved soft x-ray core-level photoemission.[2,3]

Theory

We take account of the multiple scattering effects fully so that surface information (e.g., geometrical arrangement of atoms and surface potential barrier) can be included as input. Many-electron effects, the interaction between core-hole and the other electrons (core electrons, valence- and conduction-band electrons), are also very important and cannot be neglected. However, it is always true that a single hole in the fully occupied shell can still be described by the single-particle Dirac equation with the effective potential that differs from that obtained in the ground-state calculation.

Our fully relativistic spin-polarized non-magnetic photoemission code[4] is modified so as to apply to magnetic surfaces and to introduce the modified Dirac equation that is capable of calculating core-hole wave functions with arbitrary strength of the exchange and spin-orbit interactions. Because our multiple scattering theory is based on the layer-Koring–Kohn–Rostocker (KKR) Green function method, the code also yields the layer-projected density of states (LDOS), which is itself a unique fully relativistic spin-polarized layer-KKR computer code. The new photoemission code can handle any type of photon polarization and, therefore, be applied to both linear and circular dichroism studies and yields the photocurrent and its spin polarization.

Numerical Results

The calculation is carried out for the normal emission from the body-centered cubic iron(001) surface with 90-eV linear polarized light that is impinged 16 deg parallel to the [100] direction (Fig. 1). With the exception of the experimental secondary electron background, which increases with increasing binding energy and is not calculated, the agreement between the experiment[2] and the theory is excellent: All peak positions are well reproduced, including asymmetries between different magnetizations that can be seen by the crossing points of two curves.

We also calculated the $3p$ core-hole density of states—the imaginary part of the core-hole Green function—that was used in the calculation of the photocurrent and found that the exchange and spin-orbit splittings are 0.9 to 1 eV and 1 to 1.2 eV, respectively. These values are smaller than those of the ground-state calculation but almost twice as large as those previously reported that have been obtained by direct analysis of the experimental data.
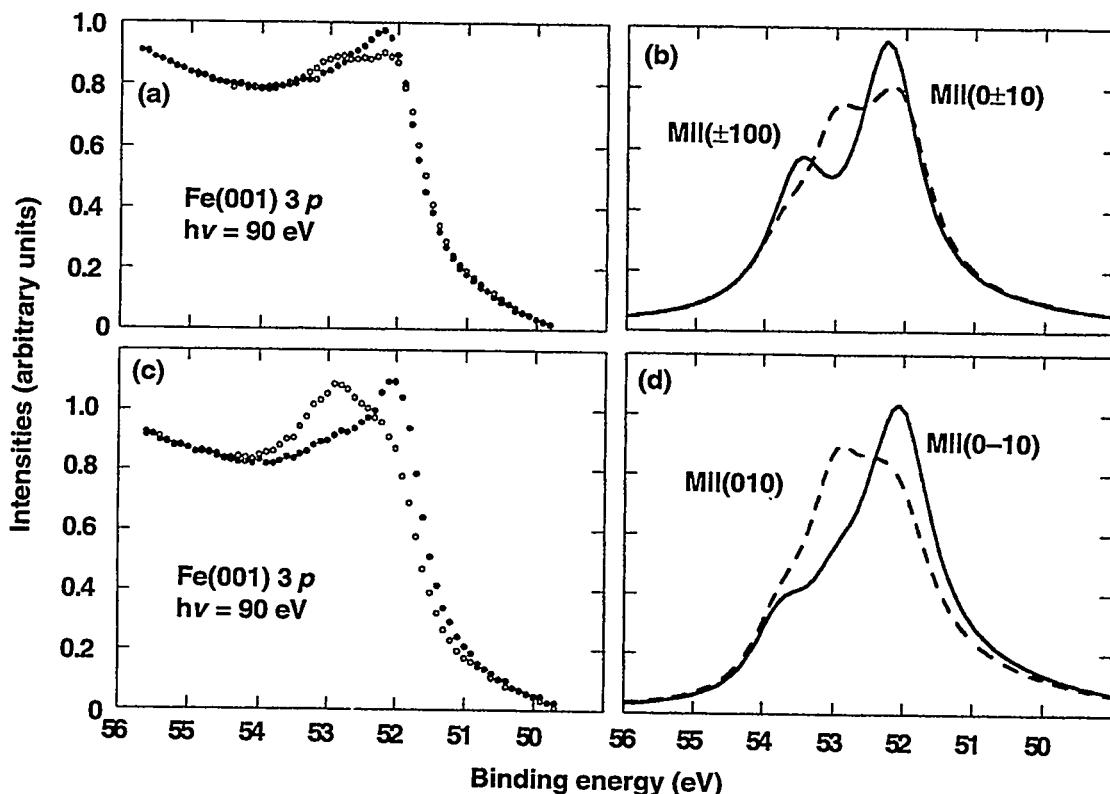
Figure 1. Angle-resolved core-level photoemission spectra from 3p iron(001) surface. The magnetic moment vectors lie in the surface-parallel plane: (a,b) parallel/anti-parallel to the [100] direction (solid circles and solid line) and to the [010] direction (open circles and dashed line) for s-polarized light (the electric field vector parallel to the [010] direction); and (c,d) parallel (solid circles and solid line) and antiparallel (open circles and dashed line) to the [010] direction for p-polarized light (the electric field vector in the plane perpendicular to the [010] direction).

The angular-momentum-specific density of states shows that a strong interference effect between the exchange and spin-orbit interactions causes the odd multiplet structure that cannot be explained within the usual Zeeman effect. Further calculation is also done for circular dichroism on face-centered cubic iron/copper(001), and the agreement with the experiment is satisfactory.[3] The study on this system will be extended theoretically and experimentally to various emission angles to explore the magnetic properties of the iron thin film.

References

1. B. T. Thole and G. van der Laan, *Phys. Rev. Lett.* **67**, 3306 (1991).

2. C. Roth, H. B. Rose, F. U. Hillebrecht, and E. Kisker, *Phys. Rev. Lett.* **70**, 3479 (1993).
3. D. P. Pappas, G. D. Waddill, and J. G. Tobin, *J. Appl. Phys.* **73**, 5926 (1993).
4. E. Tamura and R. Feder, *Europhys. Lett.* **16**, 695 (1991).

Publications

J. Tobin, G. Waddill, and D. Pappas (1993), "Magnetic Circular Dichroism in X-Ray Absorption and Core-Level Photoemission of Fe/Cu(001)," in *Vacuum Ultraviolet Radiation Physics*, F. J. Wiulleumier, Y. Petroff, and I. Nenner, Eds. (World Scientific, Singapore).

G. Waddill, J. Tobin, and D. Pappas (1993), "Magnetic X-Ray Dichroism in 2p Absorption Spectra of Fe/Cu(001)," *J. Appl. Phys.* **73**, 6748.

D. Pappas, G. D. Waddill, and J. Tobin (1993), "Magnetic Dichroism in Core-Level Photoemission from FCC Fe/Cu(0010) Films," *J. Appl. Phys.* **73**, 5936 (1993).

J. Tobin and G. Waddill (1993), "X-Ray Absorption Magnetic Circular Dichroism: Simplified Spin-Alignment Analysis of F-Electron System," *Mod. Phys. Lett. B* **7**, 317.

J. G. Tobin (1993), "Photoemission and Inverse Photoemission," in *Determination of Optical Properties, Vol. VIII, in Physical Methods of Chemistry,* B. W. Rossiter and R. C. Bretzold, Eds. (John Wiley and Sons, New York), 2nd Ed.

G. D. Waddill, J. G. Tobin, and A. F. Jankowski (1993), "Magnetic Circular Dichroism in X-Ray Absorption of Fe/Pt Multilayers," *J. Appl. Phys.* **74**, 6999.

G. D. Waddill, J. G. Tobin, X. Guo, and S. Y. Tong (1994), "Spin-Polarized Photoelectron Diffraction Using Circularly-Polarized X-Rays," *Phys. Rev. B* **73**, 1533.

A. F. Jankowski, G. D. Waddill, and J. G. Tobin (in press), "Dependence of X-Ray Absorption Magnetic Circular Dichroism on Layer Periodicity in Iron-Platinum Multilayers," *J. Vac. Sci. Tech. A* **12**(4).

J. G. Tobin and G. D. Waddill (accepted), "Resonant Photoemission and Magnetic X-Ray Circular Dichroism in the M Shell of Ultrathin Films of Fe," *J. Appl. Phys.*

J. G. Tobin, G. D. Waddill, H. Li, and S. Y. Tong (1993), "Experimental Optimization for Imaging with Photoelectron Diffraction," in *Mat. Res. Soc. Symp. Proc.* **295**, 213.

A. F. Jankowski, G. D. Waddill, and J. G. Tobin (1993), "Observation of X-Ray Absorption Magnetic Circular Dichroism in Well-Characterized Iron-Cobalt-Platinum Multilayers," in *Mat. Res. Soc. Symp. Proc.* **313**, 227.

J. G. Tobin, G. D. Waddill, T. H. Gouder, C. A. Colmenares, and D. P. Pappas (1993), "Magnetic Circular Dichroism in X-Ray Absorption and Core-Level Photoemission," in *Mat. Res. Soc. Symp. Proc.* **313**, 614.

Invited talks

J. G. Tobin, "Imaging of Surface Alloy with Energy-Dependent Photoelectron Diffraction," 20th SSRL Users Meeting, Stanford, CA (October 1993).

J. G. Tobin, "Experiments with Magnetic X-Ray Circular Dichroism," GMR Workshop, Minneapolis, MN (November 1993).

Contributed talks at conferences (and published abstracts)

J. G. Tobin and G. D. Waddill, "Resonant Photoemission and Magnetic X-Ray Circular Dichroism in the M Shell of Ultrathin Films of Fe," 38th Magn. and Magn. Materials Conference, Minneapolis, MN (November 1993).

J. G. Tobin, A. F. Jankowski, G. D. Waddill, and P. A. Sterne, "Magnetic X-Ray Circular Dichroism in Fe Co Pt Multilayers," 1994 Spring Materials Research Society Meeting (April 1994).

E. Tamura, G. D. Waddill, J. G. Tobin, and P. A. Sterne, "Linear and Circular Dichroism in Angle-Resolved Fe 3*p* Core-Level Photoemission," *Bulletin APS* **39**, 329 (1994); March Meeting of the American Physical Society, Pittsburgh, PA (1994).

A. F. Jankowski, G. D. Waddill, and J. G. Tobin, "Magnetic X-Ray Circulary Dichroism in Ni/Au(111) Superlattices," *Bulletin APS* **39**, 419 (1994); March Meeting of the American Physical Society, Pittsburgh, PA (1994).

G. D. Waddill, A. F. Jankowski, and J. G. Tobin, "Magnetic X-Ray Circular Dichroism in Fe Co Pt Multilayers," *Bulletin APS* **39**, 419 (1994); March Meeting of the American Physical Society, Pittsburgh, PA (1994).

J. G. Tobin, G. D. Waddill, X. Guo, and S. Y. Tong, "Spin-Specific Photoelectron Diffraction Using Magnetic X-Ray Circular Dichroism," *Bulletin APS* **39**, 420 (1994); March Meeting of the American Physical Society, Pittsburgh, PA (1994).

C_{58} Production from Dissociation of C_{60} by Scattering from Silica and Highly Oriented Pyrolytic Graphite

A. V. Hamza, M. Balooch, and M. Moalem

The stability of nanoclusters, in general, and fullerenes, in particular, on surfaces is of potential technological importance. The surface–cluster and cluster–cluster interactions determine the structures of nanocluster thin films. Both experimental and theoretical investigations of the C_{60} fragmentation reaction to C_{58} and C_2 in the gas phase suggest an energy barrier of 5 to 12 eV.[1-4] Using modulated molecular-beam mass spectrometry, we found a reduced barrier to the dissociation of C_{60} to C_{58} on the surface of silica and highly oriented pyrolytic graphite (HOPG) at surface temperatures greater than 900 K. The modulated molecular-beam experiments offer unique capabilities for determining surface reaction kinetics and surface dynamical processes (e.g., reactant sticking and energy accommodation).

The molecular-beam system has been described in detail.[5] The source chamber houses the reactant gas, or cluster source, and the mechanical chopper that operates at 20 Hz. A silicon wafer (6 mm diam) was oxidized in oxygen for 1 h at 1100 K to produce a SiO_2 layer a few tens of nanometers thick. An HOPG sample (6 mm diam) was cleaved just prior to being placed in vacuum. Both samples were mounted on a button heater in the target chamber, and the temperature was monitored with an infrared pyrometer. The C_{60} was incident on the target at 45 deg to the surface normal. The quadrupole mass spectrometer (QMS) (detection up to 1400 amu) in the detector-chamber samples reflected or desorbed molecules at the specular reflection angle of –45 deg. The QMS signal is processed by lock-in amplification to obtain the amplitude and phase of the signal's first Fourier component.

The production of C_{58} from C_{60} is observed on both silica and HOPG surfaces above surface temperatures of 800 K. Figure 1 shows the increase in the C_{58} signal with increasing temperature from 800 to 1400 K. The reaction probability and apparent activation energy of C_{58} are different on the two surfaces below surface temperatures of 1000 K. Therefore, we ascribe C_{58} production to a surface-specific, surface-catalyzed process.

In a separate system equipped with Auger electron spectroscopy (AES), C_{60} was continuously deposited on a silica surface at 1110 K for 30 min. After exposure a carbon residue was observable. The buildup of carbon is due to either reaction of C_{60} with the SiO_2 surface or decomposition to form C_{60} to C_{58} leaving C_1 or C_2 fragments on the surface. Above 1000 K, the reaction probability of C_{58} is the same for both HOPG and silica. As shown below, we ascribe the yield above 1000 K to the establishment of a surface equilibrium between adsorbed C_{60} and C_{58} because carbon is readily available on both surfaces.

The elementary steps at the surface involved in C_{58} production (assuming C_2 is the surface fragment) are described by Eq. (1). The C_{60} is adsorbed on the surface with sticking probability η. Adsorbed C_{60} then can either desorb with first-order rate constant k_d or react to form adsorbed C_{58} and C_2 with rate constant k_1. The recombination reaction occurs with rate constant k_2. Adsorbed C_{58} then desorbs with first-order rate constant $k_{d'}$:

$$
\begin{array}{ccccc}
 & \eta & & k_d & \\
C_{60(g)} & \rightarrow & C_{60(a)} & \rightarrow & C_{60(g)} \\
 & & k_2 \uparrow\downarrow k_1 & & \\
 & & C_{58(a)} + C_{2(a)} & & \\
 & & \downarrow k_{d'} & & \\
 & & C_{58(g)} & &
\end{array}
\tag{1}
$$
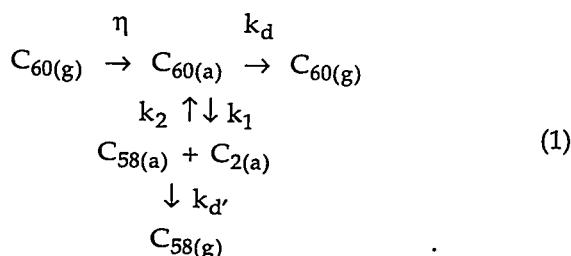
Using the appropriate surface-mass balance for the nonequilibrium case and assuming that the rate of C_{60} desorption is much greater than the rate of C_{60} to C_{58} dissociation, the reaction probability, ε_{58}, for C_{58} is approximately given by

$$
\varepsilon_{58} \cong \eta\left(\frac{k_1}{k_d}\right) .
\tag{2}
$$
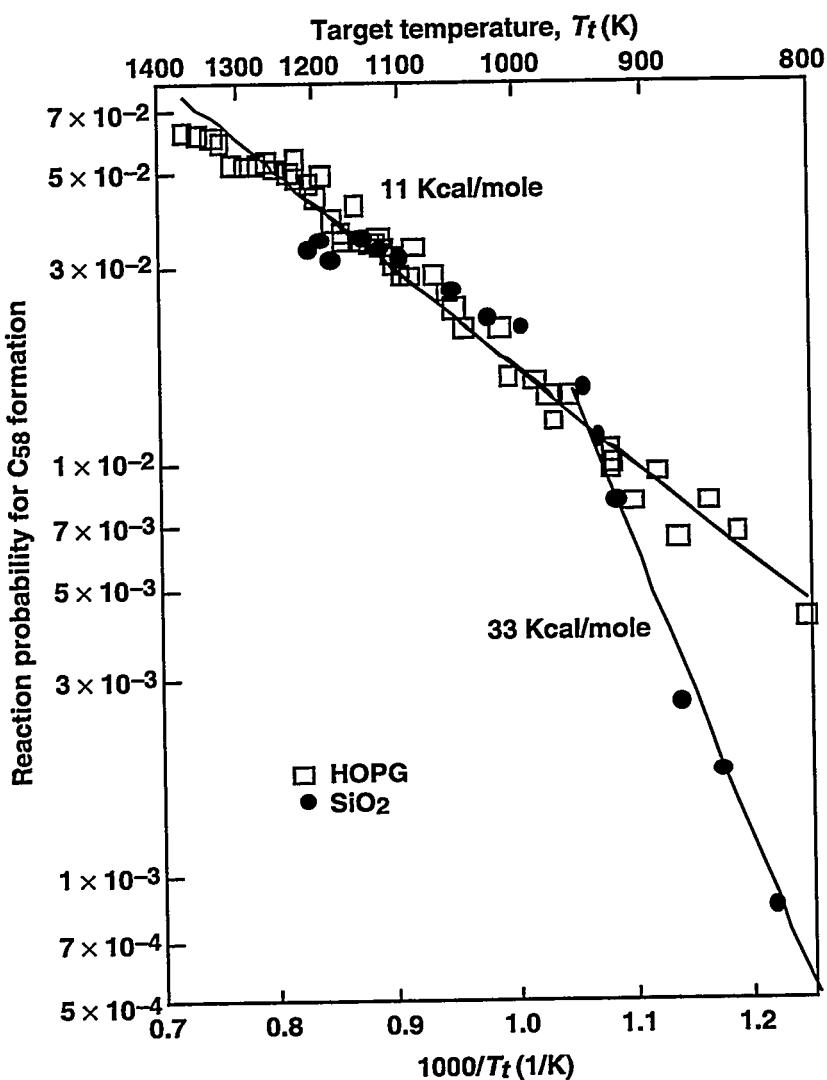
Figure 1. C_{58} signal amplitude vs surface temperature for silica and HOPG. The squares and the filled circles represent the ratios of the C_{58} signal amplitudes to the signal caused by the incident C_{60} flux from HOPG and silica, respectively.

For the silica surface at surface temperatures below 1000 K, surface equilibrium is not established because of the short residence time of C_{60} on the surface and the negligible carbon buildup. Hence, the C_{58} signal follows Eq. (2). Because η is near unity and k_d for silica (E_d = 23 kcal/mol) is known,[5] the activation energy of the rate constant k_1, representing dissociation of C_{60} to C_{58} on the surface of silica, is calculated to be about 56 kcal/mol. The lower activation energy for decomposition of C_{60} on surfaces (~2.5 eV) relative to the gas phase (5–10 eV) is probably caused by the stabilization of the C_1 or C_2 products by the surface.

On HOPG and silica at surface temperatures above 1000 K, surface equilibrium between $C_{60(a)}$ and $C_{58(a)}$ is established because of the smaller desorption rate constant relative to the surface decomposition and recombination rates and to the higher surface carbon concentration. The higher reaction probability to form C_{58} on HOPG vs silica below 1000 K is also explained by the smaller desorption rate constant for C_{60} on HOPG than silica, as seen experimentally by the phase lag measured from 700 to 1000 K for scattering of C_{60} from HOPG and the higher activation energy for C_{60} desorption from HOPG.

When surface equilibrium is established, the reaction product for C_{58} can be approximated by

$$\varepsilon_{58} \cong \eta K_e \,, \tag{3}$$

where K_e is the equilibrium constant for the C_{60} to C_{58} reaction on the surface. Because the difference in the activation energies for the forward and reverse rates is the apparent activation energy for the C_{58} signal for HOPG and silica above 1000 K, the activation energy for the reverse or recombination reaction (i.e., k_2) is estimated to be about 45 kcal/mol.

References

1. P. Sandler, C. Lifshitz, and C. E. Klots, *Chem. Phys. Lett.* **200**, 445 (1992).
2. H.-G. Busmann, T. Lill, B. Reif, and I. V. Hertel, *Surf. Sci.* **272**, 146 (1992).
3. H.-G. Busmann, T. Lill, B. Reif, I. V. Hertel, and H. G. Maguire, *J. Chem. Phys.* **98**, 7574 (1993).
4. K. R. Lykke and P. Wurz, *J. Phys. Chem.* **96**, 3191 (1992).
5. M. Moalem, M. Balooch, A. V. Hamza, W. J. Siekhaus, and D. R. Olander, *J. Chem. Phys.* **99**, 4855 (1993).

Publications

A. V. Hamza, M. Balooch, M. Moalem, and D. R. Olander (1994), "C_{58} Production from Dissociation of C_{60} by Scattering from Silica and Highly Oriented Pyrolytic Graphite," *Chem. Phys. Lett.* **228**, 117–121.

Invited Talks

M. Balooch, M. Moalem, A. V. Hamza, W. Siekhaus, and D. R. Olander, "Scattering of C_{60} from Surfaces," Electrochemical Society Fall Meeting, New Orleans, LA, October 10–15, 1993.

A. V. Hamza, "Interaction of C_{60} with Surfaces," University of California, Davis, Physics Department Condensed Matter Seminar, May 5, 1994.

Contributed Talks

A. V. Hamza, M. Moalem, D. R. Olander, M. Balooch, and W. J. Siekhaus, "Surface Mobility and Dissociation of C_{60} and SiO_2 and Highly Oriented Pyrolytic Graphite," 40th National Symposium of the American Vacuum Society, Orlando, FL, November 14–19, 1993.

M. Moalem, M. Balooch, A. V. Hamza, W. J. Siekhaus, and D. R. Olander, "Modulated Molecular Beam Study of the Interaction of C_{60} and Graphite," Materials Research Society Spring Meeting, San Francisco, CA, April 4–8, 1994.

High-Resolution Diffraction Studies of Epitaxial Silver Islands on Si(100)

P. Bedrossian, B. Poelsema,*[†] G. Rosenfeld,* L. Jorritsma,[†] N. N. Lipkin,* and G. Comsa*

Overview

We investigated silver homoepitaxy on Si(100) over a wide temperature range using a unique, new configuration incorporating both thermal energy helium atom scattering (TEAS), a nondestructive, real-time probe whose eminent surface sensitivity arises from the weak interaction of helium atoms with surface electrons, and spot-profile analysis low-energy electron diffraction (SPA-LEED), which offers rapid, rigorous, and quantitative measurements of step densities, island separations, and other periodic phenomena. Because the scattering mechanisms of TEAS and LEED differ, with the former more sensitive to surface electron distribution and the latter to atomic core positions, the combination of the techniques offers a more thorough evaluation of surface structure than would be accessible with either technique separately.

TEAS measurements detected the specular reflection of a 67-meV supersonic helium beam from an atomically clean Si(100) surface in a geometry that permitted rotation of both sample and detector through several in- and anti-phase scattering conditions. LEED spot profiles were measured with the substrate held at 77 K following silver deposition at an elevated temperature.

Apparent Giant Applanation of Small, Epitaxial Silver Islands

Figure 1 displays two specular, TEAS rocking curves following deposition of 1/2 monolayer (ML) of silver on Si(100). The peaks

and valleys observed following deposition at 300 K correspond closely to the calculated in- and anti-phase scattering conditions, respectively, whereas the rocking curve acquired after deposition at 200 K displays an increased period corresponding to an apparent lattice contraction of the outermost layer of 23%. The apparent contraction after 200 K deposition occurs only near 1/2 ML coverage; a normal rocking curve is observed for both the starting surface and one exposed to 1 monolayer silver deposition.

The appearance of strong temporal oscillations in TEAS during deposition at both temperatures establishes a layer-by-layer growth mode with planar islands. The occurrence of the rocking-curve distortion at low temperatures for 1/2 ML coverage, therefore,
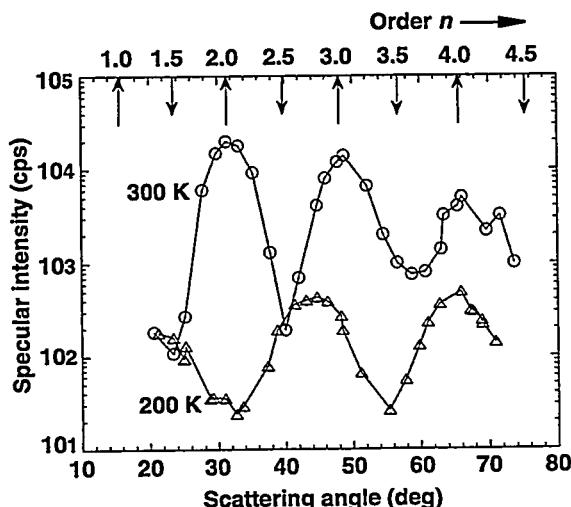
Figure 1. Specular TEAS rocking curves acquired following 1/2 monolayer deposition of silver on Si(100) at the substrate temperatures indicated. The calculated in- and anti-phase conditions are indicated by up (↑) and down (↓) arrows, respectively.

* Institut fur Grenzflachenforschung und Vakuumphysik, Julich, Germany.
† University of Twente, The Netherlands.

suggests that the effect is connected with the presence of a high density of small, flat, closely spaced islands. SPA-LEED offers a quantitative description of surface conditions that give rise to the TEAS anomaly. Prominent rings surround the central specular diffraction spikes in the anti-phase condition, and the radii of such rings in k-space are related simply to the reciprocal of the mean island separation on the surface. Figure 2 presents the appearance of such a ring in SPA-LEED surrounding four incident electron beam energies near the
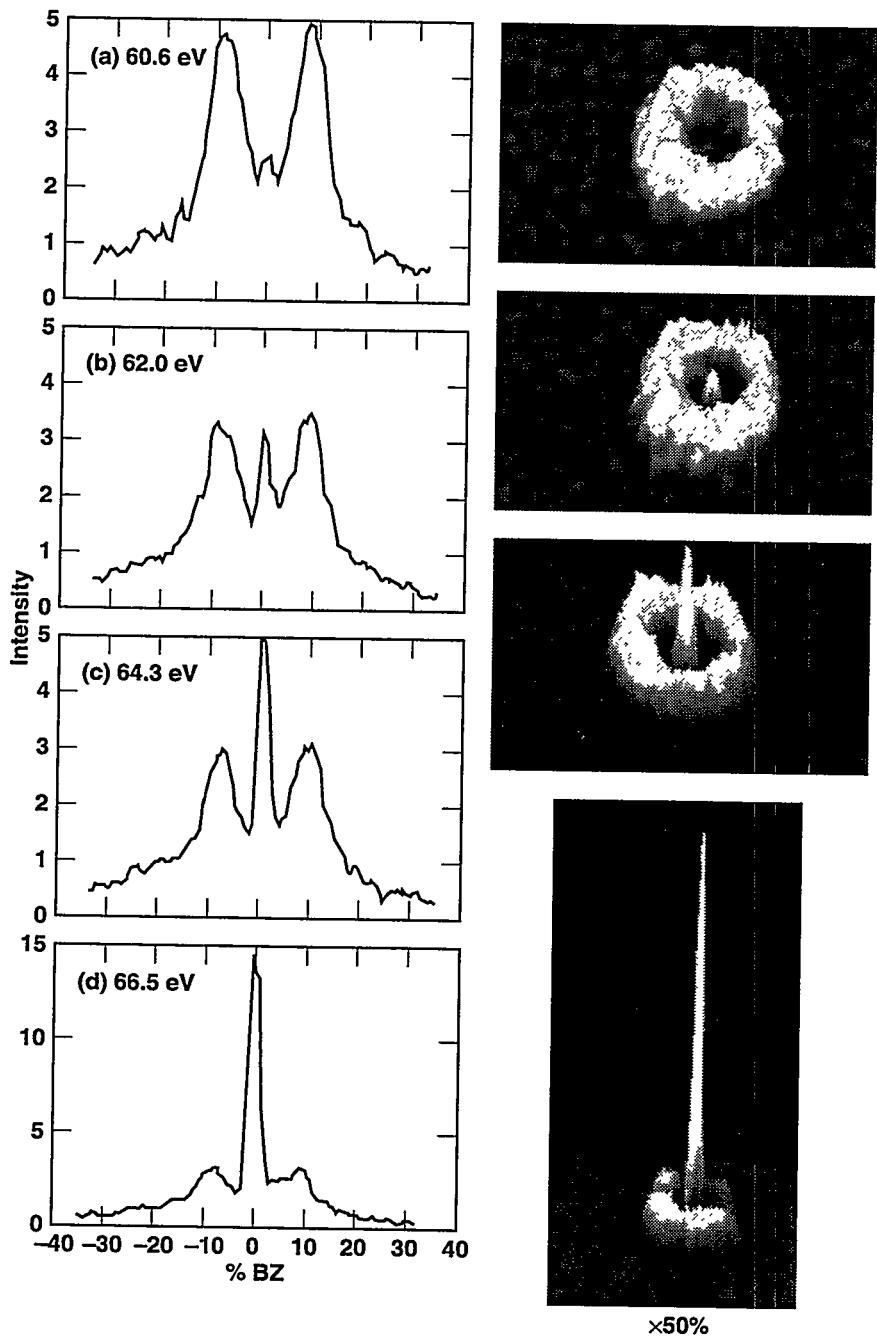
Figure 2. Profiles of the specular LEED spot near an anti-phase diffraction condition for beam energies indicated following 1/2 monolayer silver deposition on Si(100) at 200 K. The plots on the left represent one-dimensional cuts through the corresponding two-dimensional intensity maps on the right.

$n = 5/2$ anti-phase condition, following 1/2 ML silver deposition on Si(100). The two-dimensional scans acquired with SPA-LEED are presented on the right side of the figure as three-dimensional surface plots for which the displayed height scales linearly with the recorded, diffracted intensity as a function of k-space position. Destructive interference of the reflected beams from the islands and the substrate result in a minimum of the central spike with respect to the surrounding ring in the anti-phase condition (e.g., the uppermost pair in Fig. 2).

Because the energies at which the central spike reaches a minimum with respect to the surrounding ring following 1/2 ML deposition at both 200 and 300 K coincide in SPA-LEED, we do not detect any giant lattice relaxation for atomic cores in small, silver islands corresponding to that observed in TEAS. Because the apparent applanation is observed in TEAS

but not LEED, we deduce that it arises from the valence electron density at the surface rather than from the positions of the atomic cores, which retain a spacing close to their bulk separation within the islands on the surface. The occurrence of the anomaly in TEAS at low temperatures for 1/2 ML coverage suggests that it is most pronounced for a high density of small islands (~30 silver atoms/island at 175 K, deduced from the ring radius in SPA-LEED). According to the Smoluchowski effect, the interaction of the valence electrons of closely spaced, monolayer-high structures would tend to smooth the charge distribution in the outermost layer. We propose then that our results are consistent with a picture in which the interaction of small, closely spaced islands formed by Ag/Si(100) homoepitaxy induces a smoothening of the surface valence electronic density that in turn leads to an apparent applanation of the outermost layer in TEAS.

Nucleation and Ordering at Mo–Si(100) Interfaces

P. J. Bedrossian

Introduction

The binary molybdenum–silicon system has a particularly rich bulk phase diagram with a variety of stoichiometries.[1] The influence of interfacial energies on film microstructure is underscored by the ready observation of a hexagonal, C40 phase of thin disilicide films grown on silicon, which does not appear in the bulk binary phase diagram. While it has been reported widely that (1) the tetragonal, C11 disilicide is the thermodynamically stable thin-film phase and (2) a metastable, hexagonal, C40 disilicide is observed at temperatures below those at which the C11 phase forms (700–900°C, variously), the precise transition temperatures and the occurrence of other intermediate phases appear strongly process dependent.[2–4]

Several studies have used photoemission and x-ray absorption to investigate initial stages of interface formation resulting from submonolayer molybdenum deposition on atomically clean and well-defined silicon surfaces in ultrahigh vacuum (UHV) but have failed to define the resulting interfacial order.[5–8] We find that two distinct, well-defined, ordered superstructures are associated with this interfacial material, but that their short-range character precludes detection by conventional surface diffraction probes, such as low-energy electron diffraction (LEED).

The complexity of the molybdenum–silicon interfacial system and the strong dependence of physical film properties on processing procedure point to a need to diagnose and control disilicide growth by explicitly connecting those microstructural details that are strongly process dependent with conventional diagnostic measurements such as diffraction probes. Here, we demonstrate, using such an approach, what we believe to be the first investigation of MoSi$_2$ film nucleation incorporating both STM and glancing angle x-ray diffraction.

Experimental Procedure

Experiments were conducted in a UHV chamber with base pressure below 10^{-10} Torr. Si(100) substrates cut from a commercial wafer were cleaned by flashing to 1200°C in vacuum to obtain a strong 2 × 1 superstructure in both LEED and STM. The lateral lengths assigned to STM images below are calibrated with the dimer row spacing of Si(100)–2 × 1, and vertical distances are calibrated with the Si(100) atomic step height.

Substrate temperatures were recorded with an infrared pyrometer calibrated with a Type C thermocouple. Molybdenum was deposited by evaporation from a resistively heated, thoroughly outgassed, 0.010-in.-diam molybdenum wire, and deposition rates were calibrated by ex situ Rutherford backscattering spectrometry (RBS). Clean substrates were recovered in vacuum with 1-kV xenon sputtering followed by annealing at 950°C. Following deposition, samples were quenched to room temperature for analysis by in situ STM.

Homogeneous Molybdenum Incorporation ($T < 650°C$)

The STM image in Fig. 1 displays a Si(100) surface exposed to 1/2 monolayer (ML) molybdenum deposition at 475°C (1 ML = 6.73×10^{14} atoms/cm^2). Although the resulting surface previously was thought to be amorphous, the STM displays distinct, well-defined, one-dimensional superstructures of limited (4.0 nm) extent. Their short-range order precluded previous detection with LEED. Despite the local coherence of molybdenum-induced superstructures, the average molybdenum coverage is still globally homogeneous, and the presence of regularly spaced, single atomic steps indicates that molybdenum incorporation has not disrupted the original terrace structure

of the starting substrate. Within terraces, the periodicity and orientation of the original silicon dimer rows are still apparent. Further molybdenum deposition under similar conditions does not lead to growth of the thinly reacted material (Fig. 1). Instead, saturation of the outermost surface layer with molybdenum is followed by nucleation of three-dimensional islands, as in Fig. 2.

Figure 3 displays a detail of one of the molybdenum-induced superstructures in Figs. 1 and 2. While individual silicon atoms appear in the filled-states image (Fig. 3[a]), the empty-states image (Fig. 3[b]) displays a new periodicity along dimer rows, consisting of repeated units of three dimers such that the dimer in the middle of each unit is darkened relative to its two neighbors. This new period-

icity is short-ranged and one-dimensional because there is no consistency in the alignment of the repeated units between adjacent rows.

The symmetry of Figs. 3(a) and (b), together with an associated RBS coverage measurement of one molybdenum atom for every six surface silicon atoms, constrain the lateral position of the molybdenum adsorbate to a vertical line bisecting the darkened dimers in the empty-states image (Fig. 3[b]). Figure 3(c) displays the possible lateral molybdenum adsorption sites associated with this surface phase. Although the STM alone cannot constrain the vertical position of the molybdenum adsorbate, Auger electron spectroscopy measurements suggest that molybdenum atoms substitute for subsurface silicon atoms directly underneath dimers.
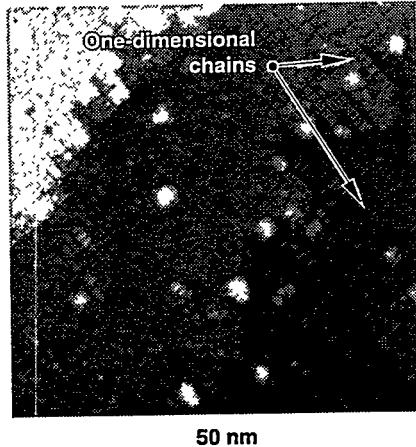
50 nm

Figure 1. Fifty-nanometer STM image following 1/2-ML deposition of molybdenum on Si(100) at 475°C. Sample bias = +1.4 V (empty sample states).

Disilicide Growth and Islanding (*T* > 650°C)

Figure 4(a) displays a 50-nm region of a Si(100) substrate following deposition of 1 ML of molybdenum at 650°C. In contrast to the smooth surface morphology at lower temperatures described above, several three-dimensional islands now appear and are surrounded by clean silicon dimer rows with the 2 × 1 periodicity. The vertical scale of the figure is defined by the single atomic step height of 0.136 nm, and the tallest structure shown reaches 1.2 nm above the surrounding silicon. Figure 4(b) presents a detail of the surface,

Filled states   Empty states
12 nm
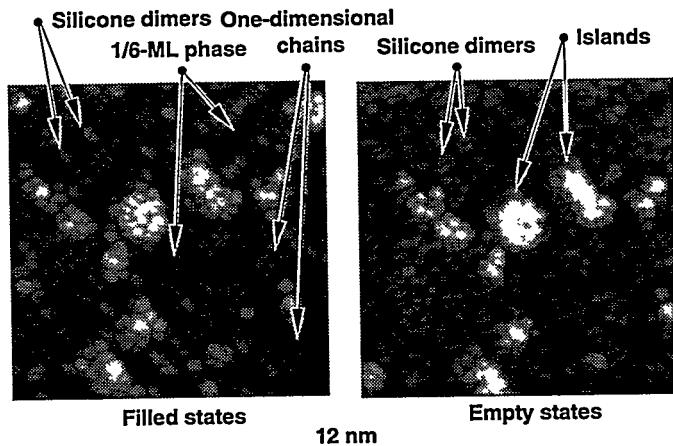
Figure 2. Twelve-nanometer detail of Fig. 1, indicating locally ordered structures. (a) Sample bias = –1.4 V (filled sample states); (b) Sample bias = +1.4 V (empty states).

(a)

(b)

−1.4-V Sample   2.5 nm   +1.4-V Sample
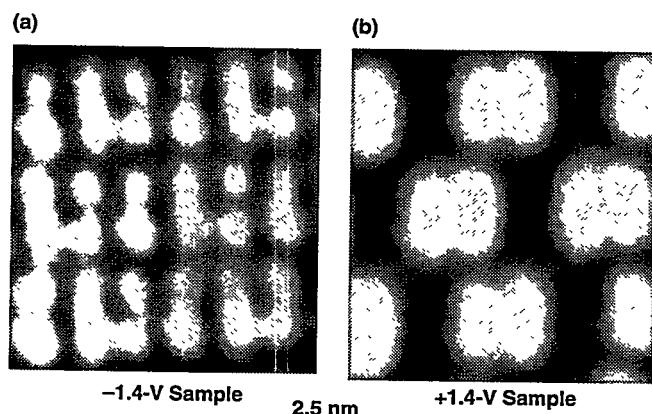
Figure 3. (a) Detail of one surface phase induced by submonolayer molybdenum incorporation in Si(100)–2 × 1. Sample bias = +1.4 V (empty states); (b) detail of same region with sample bias = −1.4 V (filled states); (c) model showing lateral molybdenum adsorption position. The crosses mark the vertical lines along which the molybdenum is constrained to lie.

(c)   Lateral molybdenum position

(a)

50 nm

(b)

C$_{40}$ (hex)

MoSi$_2$
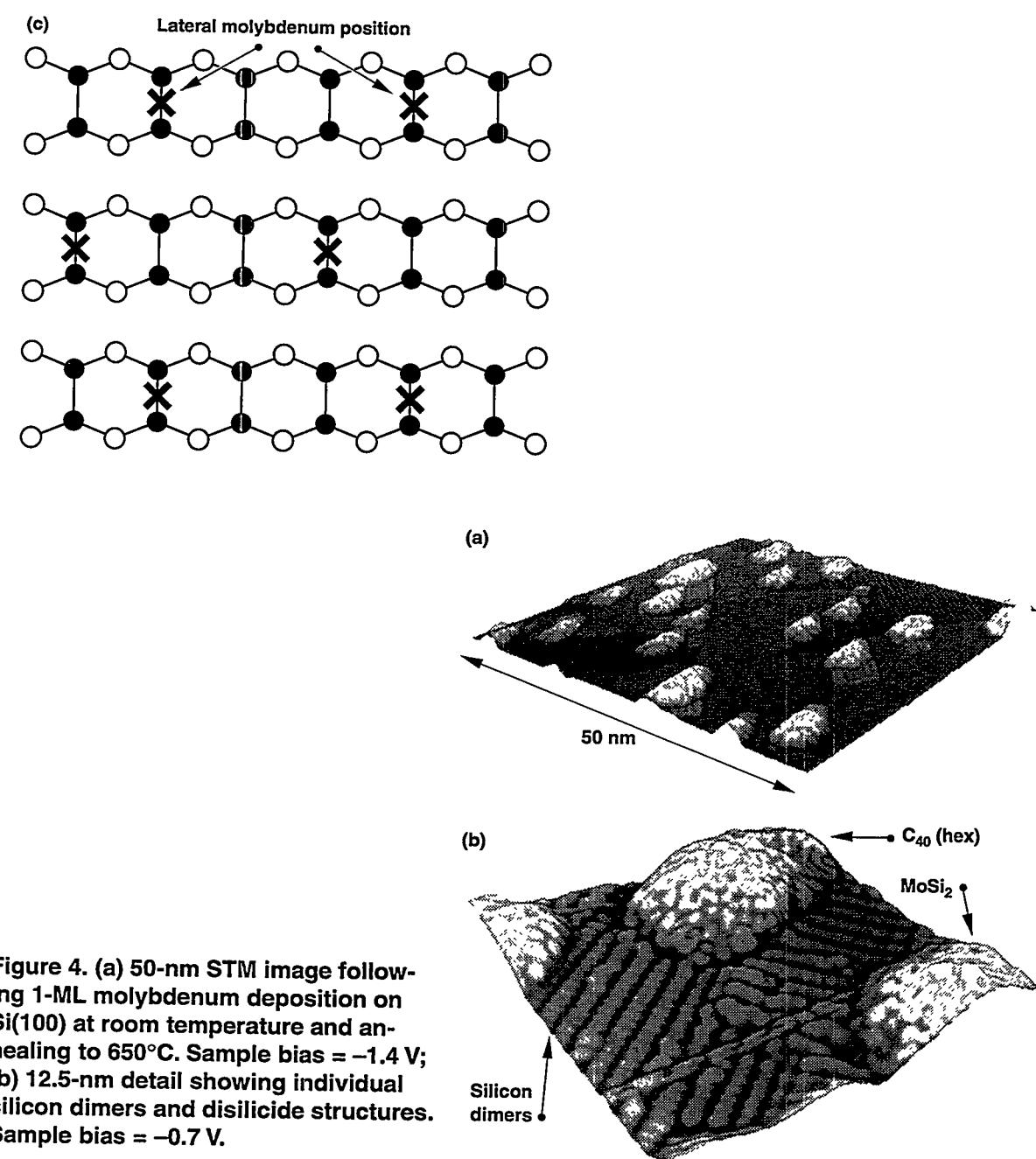
Silicon dimers

Figure 4. (a) 50-nm STM image following 1-ML molybdenum deposition on Si(100) at room temperature and annealing to 650°C. Sample bias = −1.4 V; (b) 12.5-nm detail showing individual silicon dimers and disilicide structures. Sample bias = −0.7 V.

showing individual silicon dimers on the substrate. While the STM, which is surface-sensitive, cannot display the internal details of the three-dimensional structures, and they are too confined laterally to yield a characteristic LEED pattern, their internal structure was determined by glancing angle x-ray diffraction. In situ exposure of the surface in Fig. 4 to copper $K\alpha$ radiation in a Read camera yielded strong rings at the diffraction angles for C40 $MoSi_2$, so the three-dimensional structures in Fig. 4 can be associated with the hexagonal C40 disilicide structure. The assignment defines those islands as precursors for hexagonal $MoSi_2$ thin-film growth and is consistent with previous thin-film studies described above.

Figure 4 also indicates that the Si(100) substrate itself has roughened as a result of the silicide nucleation. It was shown above that molybdenum deposition on Si(100) at 450°C preserves the density and orientation of atomic steps relative to those of the clean starting substrate. In contrast, Fig. 4 displays a greatly enhanced density of single atomic silicon steps that meander among the disilicide microcrystals. The transition from a flat, laterally homogeneous surface in Fig. 1 to the rougher,

inhomogenous surface of Fig. 4(a) requires mass transport of silicon into the disilicide material, which in turn roughens the silicon substrate. The high activation barrier associated with this mass transport of silicon into segregated disilicide structures, together with the introduction of a high density of atomic steps, define the upper limit to the temperature range of stability of the globally homogeneous, thinly reacted surface of Figs. 1 and 2.

Molybdenum deposition at higher temperatures results in the thermodynamically stable, C11 disilicide. Figure 5 displays an STM image following 4-ML molybdenum deposition on clean Si(100) at 770°C; glancing incidence x-ray diffraction confirmed the presence of the C11 $MoSi_2$. Each atomic arrangement in the image suggests a superstructure simply related to the periodicity of a low-index face of C11 $MoSi_2$, as shown. For example, the small circles in the three diagrams on the right all represent the atomic arrangement of the [001] planes of C11 $MoSi_2$. The large, shaded circles represent atomic sites in a superstructure corresponding to the periodicity observed in the regions of the STM image indicated. In the diagram on the left, the small white (dark) circles represent
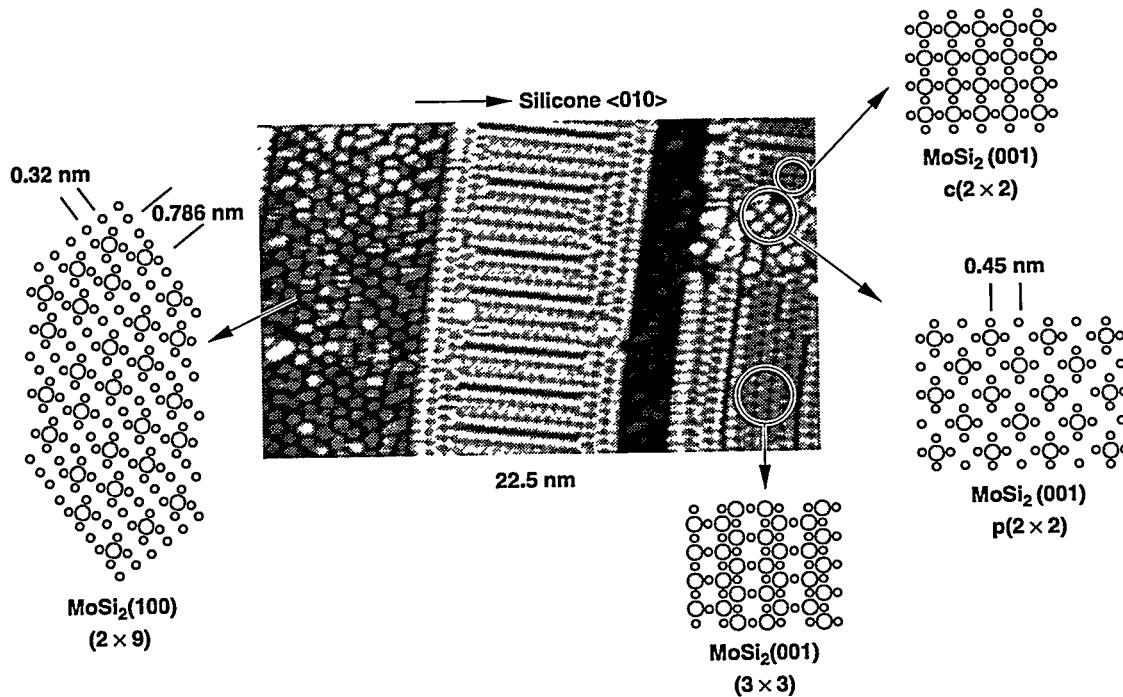
Figure 5. STM image of the surface resulting from 4-ML molybdenum deposition on Si(100) at 770°C. The diagrams indicating the registry of the superstructures suggested by the image are described in the text. Sample bias = −1.4 V.

silicon (molybdenum) atoms in [100] planes, and the large shaded disks constitute a super-structure with the periodicity in the indicated region of the image, rotated 37 deg with respect to the neighboring regions, as required for coincidence between a disilicide crystallite growing along its <100> axis and one growing along <001>.

The STM image alone is not sufficient either to assign the observed periodicities to the superstructures suggested or to associate the periodic elements with individual atomic species. Nevertheless, the correspondence of observed periodicities to simple superstruc-tures of low-index faces of C11 $MoSi_2$ suggests that superstructures form on growing faces of C11 $MoSi_2$ and that grain boundaries arising from the coalescence of independently nucle-ated disilicide microcrystallites propagate through a growing film at the temperature studied. Further study is needed to clarify the detailed nature of those superstructures and their influence on the energetics of disilicide film growth.

Conclusions

The molybdenum–silicon interface exhibits novel phases with no bulk analog. A combina-tion of microscopic and diffraction probes is necessary to define the structure of phases with short-range order. Below 650°C, a metastable, globally homogeneous surface molybdenum–silicon alloy wets Si(100) below 1-ML molybde-num fluence. The activation barrier to nucleation of $MoSi_2$ is overcome for $T > 650$°C, when disilicide segregation coincides with surface roughening. Submonolayer molybde-num deposition suffices to nucleate $MoSi_2$ above 650°C.

References

1. A. Gokhale and G. Abbaschian, *J. Phase Equil.* **12**, 493–498 (1991).
2. T. Chou and T. Nieh, *Thin Solid Films* **214**, 48–57 (1992).
3. C. Doland and R. Nemanich, *J. Mater. Res.* **5**, 2854–2864 (1990).
4. A. Perio and J. Torres, *J. Appl. Phys.* **59**, 2760–2764 (1986).
5. I. Abbati, L. Braicovich, B. D. Michelis, A. Fasana, and A. Rizzi, *Surf. Sci.* **177**, L901–L906 (1986).
6. H. Balaska, R. Cinti, T. Nguyen, and J. Derrien, *Surf. Sci.* **168**, 225–233 (1986).
7. H. Meyerheim, U. Dobler, A. Puschmann, and K. Baberschke, *Phys. Rev. B* **41**, 5871–5880 (1990).
8. J. Slaughter, A. Shapiro, P. Kearney, and C. Falco, *Phys. Rev. B* **44**, 3854–3863 (1991).

Fundamentals of the Physics and Processing of Metals

W. H. Gourdin

Thrust Area Leader

Our study of the influence of segregated boron on the mechanical strength of individual grain boundaries in Ni_3Al concluded this year. Prior to her departure from the Laboratory early in the year, Pat Johnson completed the first tensile tests of heat-treated natural bicrystals. From her results, she tentatively concluded that the behavior of individual boundaries can be intermediate between the ductile–brittle extremes noted in polycrystalline samples. She summarized her findings in a presentation at the fall meeting of the Materials Research Society in December 1993. This work will also appear in the published proceedings from that conference.

Late in the year, Stuart Weinland and I completed a series of tensile tests on artificial $\Sigma5(210)$ bicrystal specimens prepared in Wayne King's diffusion-bonding machine. Like the natural bicrystals, these were heat-treated in such a way as to encourage or discourage the segregation of boron to the interface. Although some specimens had clearly not bonded completely, our results nevertheless demonstrate that boron strengthens even these highly symmetric boundaries.

The theoretical portion of this work shifted its focus this year to "supercell" calculations. Such calculations, as their name implies, explicitly calculate the electron structure over a volume larger than a single unit cell and so require significantly more computation. Some of the theoretical effort during this period, therefore, was devoted to improving the efficiency of the codes. This has paid substantial dividends: The calculations can now be executed an order of magnitude faster, making it practical to use workstations rather the CRAY computers. The results of these calculations confirm that the effects of boron and hydrogen solutes are primarily local in nature and that boron tends to promote an electron distribution normally associated with increased lattice cohesion, whereas hydrogen has the opposite effect. We also found that the effects of boron on the electron distribution are not greatly altered when boron and hydrogen are placed in adjacent sites within the lattice.

The study of stoichiometric interlayer bonding under the direction of Mike Strum continued to show excellent progress. Mike and his coworkers characterized the structure and evolution of the bond interface in NiAl and extended the technique to $MoSi_2$.

Bonding of Intermetallics Using Stoichiometric Interlayers

M. J. Strum and G. A. Henshall

Overview

Our present goal is to develop a predictive understanding of the isothermal bonding process in which elemental films placed at the joint interfaces react to form a joint with the same stoichiometry as the parent material. Our joining method is a modification of conventional liquid-assisted diffusion-bonding processes in which melting-point depressants are replaced by segregated films of the intermetallic constituents. Through this method, we obtained NiAl joint compositions and microstructures that closely approximate those of the NiAl parent material. The method is particularly suitable for joining high-temperature materials, including intermetallics and ceramics, which have poor weldability by conventional fusion-welding methods. The refractory intermetallics NiAl and $MoSi_2$ were selected as model systems for investigation of bonds in aluminides and silicides.

Progress

In FY94, we evaluated a series of interrupted bonding treatments between NiAl couples and used the results to predict the influence of time, temperature, and interlayer thickness on homogenization of the bond region. Using a solid-state diffusion model, predictions of bond homogenization rates were calculated as a function of interlayer thickness and reaction temperature. Experiments confirmed that solid-state interdiffusion controls the overall rate of bond homogenization in the transient liquid phase bonds. We also investigated a second intermetallic system, $MoSi_2$. A collaboration was established with J. Petrovic of Los Alamos National Laboratory, who provided hot-pressed $MoSi_2$ ingots for use in our bonding studies. The preliminary evaluations of wetting and interlayer reaction in this system were positive, indicating the suitability of using reaction bonding to join silicide intermetallics.

In NiAl couples, the evolution of microstructure, composition, and microhardness was characterized using thick interlayers. NiAl formed within the bonds by epitaxial growth from the NiAl–aluminum and NiAl–nickel interfaces as evidenced by the absence of grain boundaries, while a polycrystalline zone of NiAl nucleated from the polycrystalline nickel coating at the nickel–aluminum interface. These grain boundaries migrated across the joint interfaces, eliminating the original interfaces.

We measured the composition profiles across the bond region for each heat treatment between 1 and 32 h at 1200°C. We compared compositional profiles after 2 and 32 h at 1200°C and found the aluminum diffusive layer widens rapidly due to the high solubility of nickel in liquid aluminum (Fig. 1). Isothermal solidification was complete within 2 h and complete transformation to NiAl, limited by solid-state nickel diffusion, was achieved within 4 h at 1200°C. After 32 h at 1200°C, the minimum solidus within the bond region is raised to approximately 1600°C or 98% of the melting point of stoichiometric NiAl.

Figure 2 shows that the rate of homogenization within the bond, as defined by the peak nickel and aluminum concentrations, is logarithmic once the bond becomes single-phase NiAl. The homogenization data were combined with a diffusion model to predict bonding times to achieve a minimum solidus of 1600°C for thinner interlayers and higher temperatures. Decreasing the thickness of the interlayers by a factor of 5, from 0.25 mm aluminum and 0.16 mm nickel to 0.05 mm aluminum and 0.033 mm nickel, decreased homogenization times at 1200°C by a factor of 25, from 32 to 1.5 h. Increasing the bonding temperatures above the nickel–Ni_3Al eutectic (1385°C) was of interest as a means of eliminating the polycrystalline layer and increasing the dissolution rate
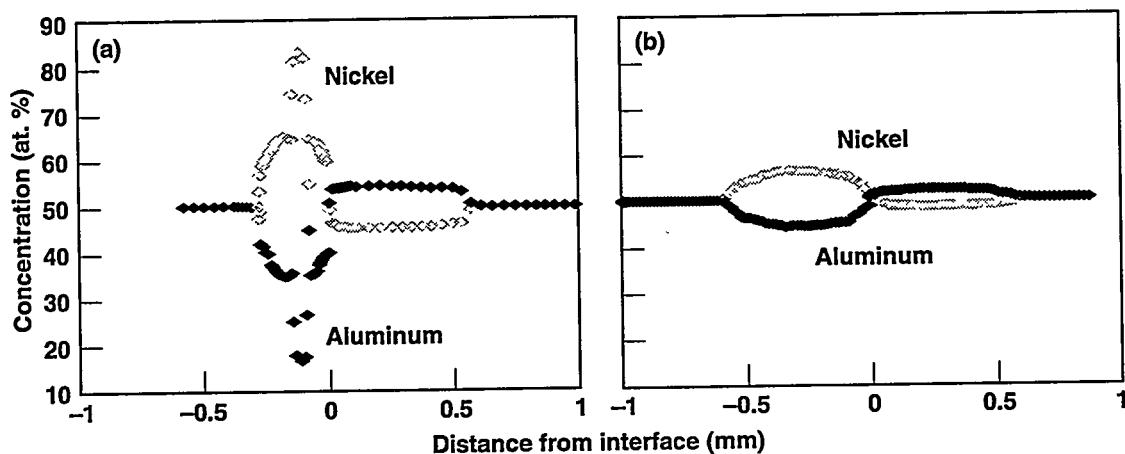
Figure 1. The chemical composition profile across the joint interface after (a) 2 h at 1200°C and (b) 32 h at 1200°C for NiAl substrates coated with 0.25 mm aluminum and 0.165 mm nickel. The compositions were measured by electron microprobe microanalysis.
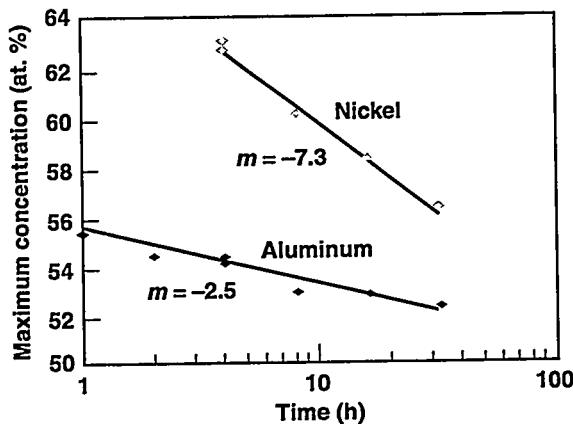
Figure 2. Peak nickel and aluminum concentrations for the NiAl bonded couples as a function of time at 1200°C and the logarithmic fit to the data [$y = m(\log x) + b$].

of the nickel solid solution. Increasing the reaction temperature to 1425°C resulted in a single crystal bond and decreased homogenization times for thick interlayers from 32 h at 1200°C to 3 h at 1425°C, as predicted by the temperature dependence of nickel interdiffusion.

Our work in the MoSi$_2$ system has also yielded promising results. Wetting tests using silicon foils on molybdenum at 1410°C revealed a low contact angle and rapid spreading. Compositional evaluation by energy dispersive x-ray spectroscopy indicated the presence of MoSi$_2$ on the surface of the specimen, and

profile metallography indicated complete consumption of the 0.05-mm silicon foil within 60 s at 1410°C. The fabrication procedure for electron-beam evaporation for molybdenum coatings on MoSi$_2$ substrates was successfully developed (by R. Juntz), producing fully dense coatings that reaction-bond to the MoSi$_2$ substrates. The configuration of interlayers in MoSi$_2$ bonds was found to be important, with molybdenum coating on a single side resulting in resolidification of the silicon prior to complete reaction with the uncoated MoSi$_2$. Coating both substrate surfaces increased the thickness of a stoichiometric silicon foil, and liquid containment was incomplete creating a silicon-deficient bond with MoSi$_2$ formation at the joint interface and Mo$_5$Si$_3$ layers adjacent to the MoSi$_2$ substrates. Fully bonded joints with no liquid loss were produced by decreasing the thickness of the interlayers while maintaining a stoichiometric interlayer composition.

Publications

M. J. Strum and G. A. Henshall (1994), "Liquid-Assisted Diffusion Bonding of NiAl," in *Advanced Joining Technologies for New Materials II* (American Welding Society, Miami, FL, 1994), pp. 76–88.

M. J. Strum and G. A. Henshall (1995), "Reaction Bonding of Intermetallics," submitted to *Metallurgical Transactions*.

Formability of Aluminum Alloys

G. A. Henshall

Background and Objectives

Manufacturers have become increasingly interested in near net-shape forming, particularly of lightweight aluminum alloys, as a means of reducing production costs. Many such forming processes require materials with high tensile ductilities well in excess of 100%. The objective of this project was to begin examining "extended ductility" of aluminum–magnesium alloys in the warm forming regime (roughly 200–400°C). In this regime, solute drag of dislocations leads to strain-rate sensitivities near 0.3 and, therefore, large tensile ductilities. We began evaluating the alloy chemistry, metallurgical variables, and processing conditions controlling ductility and warm formability of aluminum–magnesium-based alloys. This information could be used to better understand the deformation and failure mechanisms in solution-hardened aluminum–magnesium alloys and to define the critical processing variables required to provide optimal formability.

Progress

We performed experiments using two coarse-grained binary alloys: Al–2.8 wt% Mg
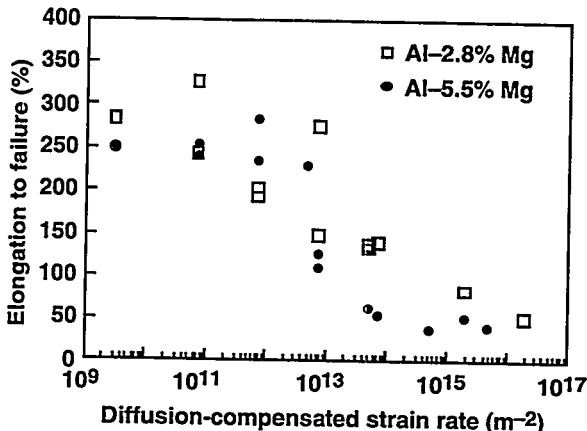
Figure 1. Tensile elongation to failure as a function of the diffusion-compensated strain rate for two binary aluminum–magnesium alloys.

and Al–5.5 wt% Mg. Within this range, the magnesium concentration only slightly affected strength and had no significant effect on the failure strain (e_f), which reached values as high as 325%. The tensile ductility was found to correlate strongly with the strain-rate sensitivity (m), and failure occurred by necking to a point. The value of m was controlled by the diffusion-compensated strain rate during testing. Tests performed under widely different temperatures and strain rates resulted in a similar e_f if the diffusion-compensated strain rates were similar. This finding suggests that e_f is controlled by the viscous drag of solute atmospheres by moving dislocations during grain matrix flow. Figure 1 shows these experimental results.

A numerical model of neck growth properly predicts e_f in these binary alloys, indicating that tensile ductility is controlled by the value of m when failure occurs by necking. Because there is little strain hardening in the regime where ductilities are large, the strain-hardening rate does not need to be included in the analysis.

Finally, through comparisons with earlier results for a low purity aluminum–magnesium–manganese alloy, it appears that the addition of manganese decreases the ductility of aluminum–magnesium solid solutions. A maximum e_f of only 125% was achieved in the ternary alloys. This decrease in ductility relative to the binary alloys is due in part to a reduced m value. Other factors, such as cavitation at second-phase particles, may also contribute to the reduced ductility of the ternary alloys.

Publications

E. M. Taleff, G. A. Henshall, D. R. Lesuer, T. G. Nieh, and J. Wadsworth, "Enhanced Tensile Ductility of Coarse-Grain Al–Mg Alloys," in *Proc. TMS Symp. Superplasticity*, A. K. Ghosh, Ed.

E. M. Taleff, G. A. Henshall, D. R. Lesuer, and T. G. Nieh (1994), "Warm Formability of Aluminum–Magnesium Alloys," in *Proc. Fourth Int. Conf. Aluminum Alloys*, T. H. Sanders and E. A. Starke, Jr., Eds., pp. 338–345.

Solute Segregation Behavior in Ni₃Al-Based Ordered Alloys

W. H. Gourdin, N. Kioussis,* A. Gonis, P. E. Johnson, and P. M. Smith

Overview

The role of boron in polycrystalline Ni₃Al has become a paradigm for solute effects in which the appropriate selection of an interstitial dopant can completely suppress brittle behavior. Exactly what boron does to achieve this remarkable effect is not well understood, and interest in boron, as well as embrittling solutes such as hydrogen, remains high. We are seeking a better understanding of the role of boron in Ni₃Al experimentally through a set of tests that allows simultaneous measurements of the chemistry, structure, and plastic behavior of individual grain boundaries and theoretically with a series of first-principles calculations on bulk Ni₃Al with and without boron.

In our experiments, 3-mm-gauge-length, shoulder-grip tensile specimens, with a single grain boundary bisecting the gauge length, are cut from either an extremely large-grained boron-doped polycrystal or a single crystal fabricated by diffusion bonding of carefully polished and oriented single crystals. Tensile testing is performed on a small stepper-motor-driven load frame equipped with a miniature clip-on extensometer. The grain-boundary boron level is controlled by varying the heat treatments, and the crystallography of the natural bicrystals is measured using backscattered Kikuchi patterns (EBSP), which are collected from the specimen surface using a scanning electron microscope.

We believe that boron enhances the electron transfer in Ni₃Al, thereby promoting cohesion, particularly in regions containing lattice defects such as at a grain boundary. To investigate this, we are using both warped muffin-tin and full-potential, linear muffin-tin orbital (LMTO) codes to study the effects of boron and hydrogen on the electron distribution in Ni₃Al. In interpreting the results of our calculations, we make the fundamental as-

---

* California State University at Northridge.

sumption that the changes in electron distribution produced by solutes segregated to the open regions in a grain boundary are qualitatively the same as those produced when the solute occupies an interstitial position in the lattice itself.

Progress

Experimental Results

Last year, we cut, polished, and analyzed for relative orientation seven dog-bone–shaped test specimens bisected by a single boundary. One set of five specimens contained nominally the same boundary (boundary A), whereas a second set was taken from a separate boule (boundary B). This year, these specimens were heat-treated at 1040°C in argon, slow cooled or quenched to vary the boron segregation, and then tested in tension. Testing was conducted in both ambient air and an ultralow-water-vapor environment provided by a glove box.

Figure 1 shows the results of these tests. The quenched A specimen, which should have very little boron segregation, showed the extreme brittleness characteristic of undoped Ni₃Al. In contrast, the slow-cooled specimens, which should have enhanced boundary segregation of the boron, showed substantial ductility, but not as large as might be expected in polycrystals. When tested in a water-free environment, the ductility of the slow-cooled samples increased substantially to values comparable to polycrystals tested in air. The behavior of slow-cooled B samples was comparable to that of specimens of boundary A. Examination of fracture surfaces revealed that only the specimens tested in the low-water-vapor environment show the dimpled failure surfaces associated with ductile failure; slow-cooled air-tested samples, while they show substantial elongation prior to failure, nevertheless fail by cleavage.
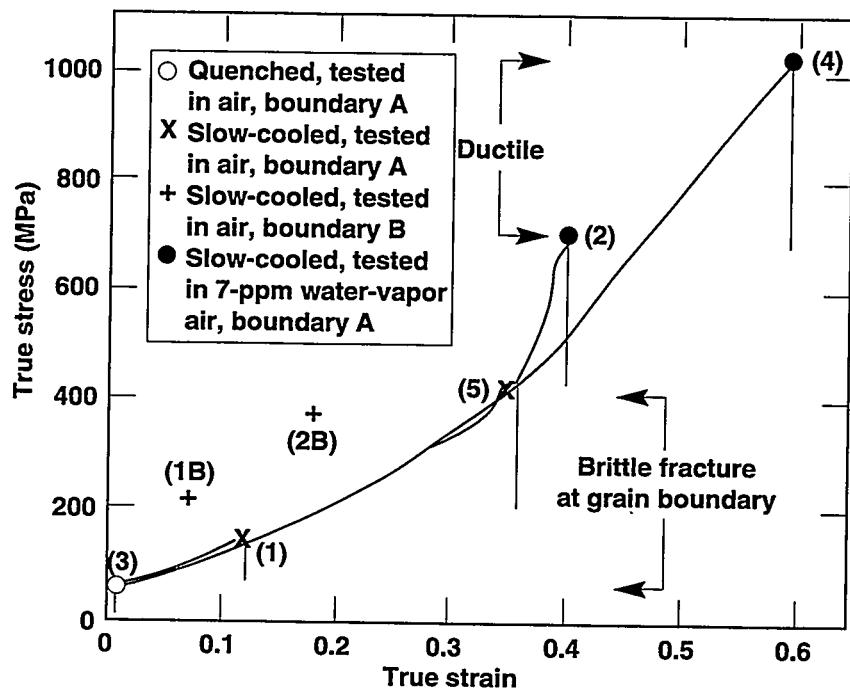
Figure 1. Tensile stress–strain curves for natural bicrystals.

We believe that these limited results on natural bicrystals suggest at least two conclusions. First, individual boundaries clearly can show limited ductility, intermediate between the brittle failure of quenched material and fully ductilized polycrystals. Although we have not yet determined the boron concentration at the boundaries, this observation does suggest that intermediate levels of boron offer limited strengthening of individual boundaries, and the apparently abrupt brittle-to-ductile transition as boron is added to polycrystals is not necessarily a reflection of similarly abrupt underlying modifications to local boundary cohesion. Second, single exposed boundaries may be particularly sensitive to environmental embrittlement, such that fully ductile behavior can be observed only in the absence of water vapor. Although similar environmental effects have been noted in polycrystals, Ni_3Al polycrystals doped with the proper amount of boron are ductile even in moist air.

During the latter part of the year, we completed the fabrication of a diffusion-bonded bicrystal with a $\Sigma5(210)$ simple tilt boundary. From this we prepared a series of miniature tensile specimens that, along with control specimens of boron-doped polycrystalline Ni_3Al, were heat-treated and tested in the

same manner as the natural bicrystals. Diffusion bonding of the bicrystal was clearly not uniform, and several specimens failed during the cutting process or set-up on the tensile tester. However, slow cooling of the specimen, which promotes boron segregation, appeared to be a necessary condition for ductile behavior.

Figure 2 shows a comparison of the true stress–true strain curves for slow-cooled and water-quenched specimens tested in dry argon. The water-quenched material shows very little ductility, and the boundary fails in a brittle manner after only a small strain. In contrast, the slow-cooled sample deforms to a true strain of nearly 35% before failure. The large elongation of slow-cooled material was confirmed with a second specimen, but a third failed prematurely, presumeably because the bicrystal was poorly bonded. For comparison, one slow-cooled specimen and one water-quenched specimen were tested in air. Both of these failed at small strains, irrespective of heat treatment. Because additional samples were not available, this behavior could not be confirmed, and we can draw no conclusion regarding the influence of atmosphere. The polycrystalline specimens show large tensile ductilities (>30% elongation) regardless of heat treatment. As indicated below, however, these specimens contained
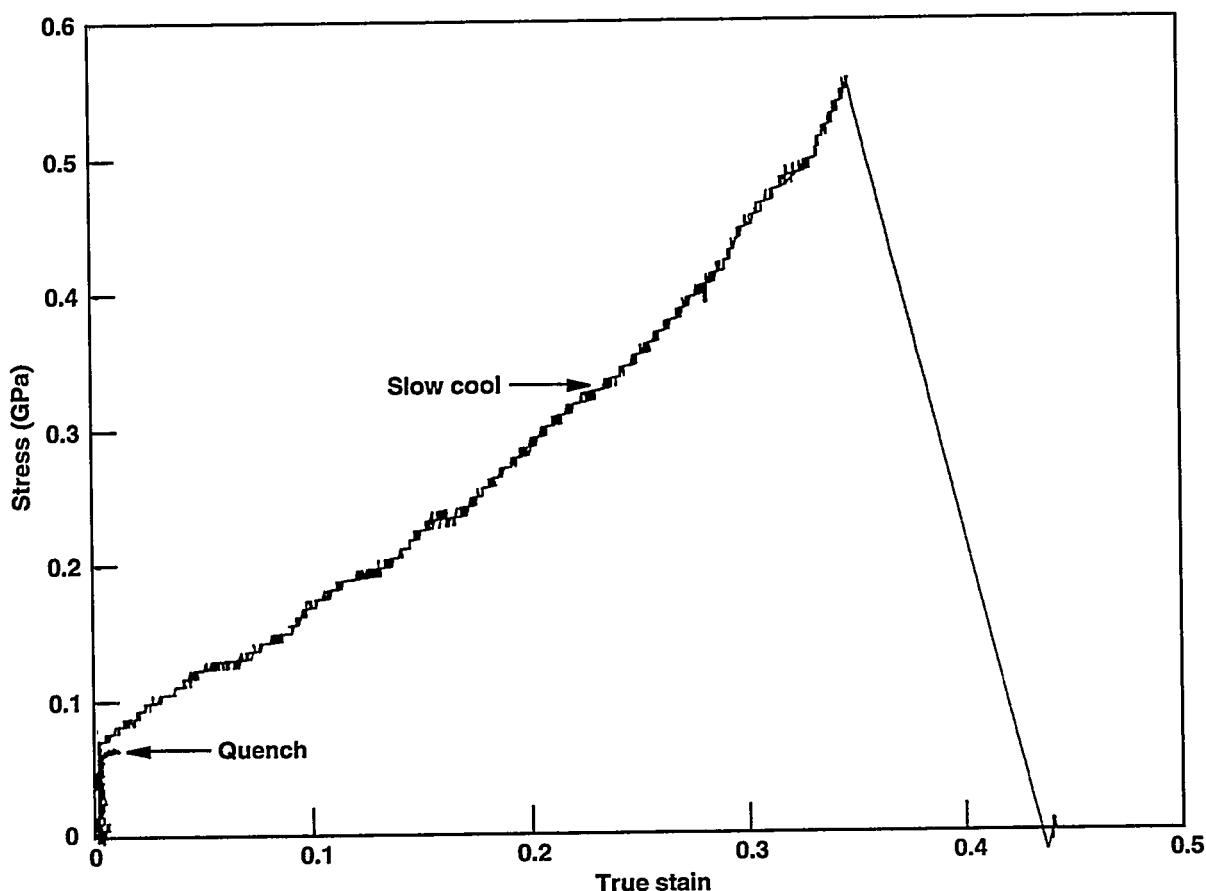
Figure 2. Tensile stress–strain curves for diffusion-bonded bicrystals with Σ5(210) simple tilt boundaries.

eight times more boron than the diffusion-bonded bicrystals, so our heat treatment may not be sufficient to completely deplete their boundaries of segregated solute.

We also completed the secondary ion mass spectrometry (SIMS) analysis of the bulk boron content of the single-crystal material from which the bicrystals were made. Surprisingly, the bicrystal material contains approximately 0.01% boron by weight, only 20% of what the supplier quoted. Given such a low boron content, the ductility of the slow-cooled specimens is somewhat surprising, but it may also account for the efficacy of the heat treatments. The polycrystalline specimens contained approximately 0.08 wt% (800 wt ppm) boron.

Theoretical Results

Theoretical efforts have focused on the implementation of full potential LMTO methods and their use in supercell calculations (which use several FCC unit cells as a basis) to study concentration effects on the electronic structure of boron-doped Ni_3Al. Because of a lack of CRAY computer time, the full-potential supercell calculations must be run on a workstation. To make this practical, improvements to existing codes were implemented that yielded a 10-fold increase in execution speed. Supercell calculations were then performed with boron and hydrogen placed in each of two different octahedral interstices in the lattice.

Consistent with earlier calculations, the present results indicated that boron induces a charge redistribution in the lattice that is associated with enhanced lattice cohesion (the charge density between atomic planes is enhanced), and it prefers to occupy the interstice in which it is entirely coordinated by nickel atoms. In contrast, hydrogen solutes appear to produce a charge redistribution

consistent with weakened bonding in the lattice. Our calculations indicate that the effects of solutes are primarily local in origin. Consistent with this, the presence of hydrogen in an adjacent site has only secondary effects on the charge distribution produced by boron. These results suggest that boron can indeed act as a binding agent both in the lattice and at grain boundaries, particularly in nickel-rich material. Similarly, hydrogen alone acts as a weakening agent but does not necessarily act to negate the effect of boron.

Publications

P. E. Johnson, W. Gourdin, A. Gonis, N. Kioussis, and M. Vaudin (in press), "Boron and Hydrogen in Ni₃Al: Part II. Mechanical Testing of Bicrystals," to appear in *Proc. Materials Research Society Symp.*

N. Kioussis, H. Watanabe, R. G. Hemker, W. Gourdin, A. Gonis, and P. E. Johnson (1994), "Effect of Boron and Hydrogen on the Electronic Structure of Ni₃Al," ("Boron and Hydrogen in Ni₃Al: Part I") in *Proc. Materials Research Society Symp.* (Materials Research Society, Pittsburgh, PA), vol. 319, pp. 363–368.

S. Sun, N. Kioussis, S. P. Lim, A. Gonis, and W. H. Gourdin, "Impurity Effects on Atomic Bonding in Ni₃Al," (to be submitted).

Energetic Materials

R. L. Simpson
Thrust Area Leader

The energetic materials thrust area seeks to develop new materials and processing routes for materials of interest to industry, the Department of Defense (DoD), and the Department of Energy (DOE). Currently, automobile air-bag systems incorporate sodium azide as the gas-generator material. Sodium azide is attractive because of its thermal stability, rate of gas generation upon decomposition, availability, and cost. Unfortunately, it is considered environmentally unsuitable because of possible generation of hydrazoic acid, a severe poison. These environmental concerns have initiated a nationwide search for new materials to replace sodium azide. This synthesis work also has direct relevance to our DOE and DoD national security goals.

We also address a critical need in the demilitarization of conventional and nuclear weapons. Open burn or open detonation (OB/OD) is currently the standard method of destruction of energetic materials, and the United States has many OB/OD-permitted facilities. Public concerns and increasingly stringent environmental regulations have made OB/OD of energetic materials increasingly costly. It will likely be banned throughout the United States and Europe in the near future. The molten salt destruction (MSD) process is an alternative to OB/OD for the destruction of energetic materials and energetic-material-containing wastes. MSD is an attractive technology because of its inherently low gaseous emissions and the ability of the salt bath to scrub both acidic gases and particulates. Understanding the kinetic details of the process is essential for further scale-up of the MSD process. In our MSD work, we seek to provide fundamental scientific information to a significantly larger programmatic effort.

Fundamental Kinetics of Molten Salt Destruction of Energetic Materials

B. E. Watkins, R. L. Kanna, R. S. Upadhye, and C. O. Pruneda

Overview

LLNL is developing methods for the safe and environmentally sound destruction of energetic materials. Open burn/open detonation (OB/OD) is currently the most common method of destruction of energetic materials, and the United States has many OB/OD-permitted facilities for the destruction of these materials. Public concerns and increasingly stringent environmental regulations have made OB/OD of energetic materials increasingly costly. As a result, OB/OD may be banned in the near future.

The Molten Salt Destruction (MSD) process is an alternative to OB/OD for the destruction of energetic materials and energetic material-containing wastes as described by Upadhye et al.[1] MSD is an attractive technology because of its inherently low gaseous emissions and the ability of the salt bath to scrub both acidic gasses and particulates. LLNL is currently operating a nominal 7.5-kg molten salt bath (Fig. 1). This unit is being used to address key technical issues before this process can be commercialized. Work presented here is directed to the understanding of fundamental kinetics and mechanism of destruction of explosives. This understanding will facilitate the scale-up of the process to commerical-sized units.

Progress to Date

We have modified an existing 7.5-kg salt bath (an equal-weight mixture of lithium, potassium, and sodium carbonates with a melting point of about 400°C) to accept a continuous feed. Previously, the unit was only used in batch mode. Energetic materials were obtained as pure powders, molding powders, or pressed parts. The pressed parts were water-machined to a powder, and all materials were passed through a 1.5-mm screen. A slurry consisting of 33% by weight energetic material (25% for LX-16), 1% methyl cellulose, and water was entrained in a stream of air and injected into the salt bath. This unit typically operates at 700 to 750°C.

The levels of both NO and CO are quite low for all energetic materials tested (Table 1). These data are presented as the percent of nitrogen or carbon in the feed that leaves the unit as NO or CO. Presenting data in this manner allows evaluation of the stack gas independant of the driver gas feed rate. At the 700 to 750°C operating temperatures, thermal
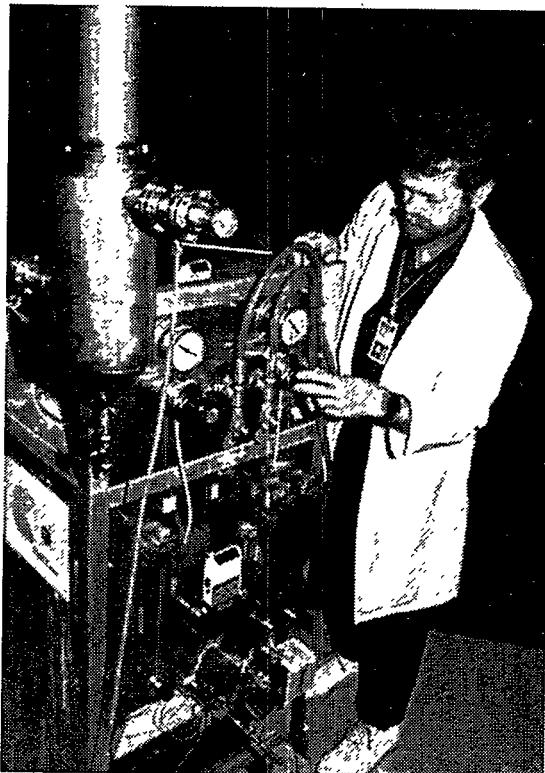

Figure 1. The 7.5-kg molten salt unit.

Table 1. Incomplete oxidation levels of C and N.

Explosive[a]	%C → CO	%N → NO	Throughput (kg/h)	Form
RDX	0.035	0.05	1.8	Neat powder
HMX	0.035	0.11	1.4	Neat powder
TNT	0.006	0.45	0.50	Neat powder
Explosive D	0.028	0.18	0.49	Neat powder
Comp B-3	0.051	0.09	1.0	Powder
LX-10	0.029	0.019	0.99	Machined part
LX-16	0.064	0.14	1.3	Molding powder
LX-17	0.029	0.20	0.69	Machined part
PBX-9404	0.09	0.25	. 0.3	Machined part
LP XM46	0.11	0.58	2.6	Diluted solution

[a] RDX = Hexahydro-1,3,5-trinitro-1,3,5-triazine.

HMX = Octahydro-1,3,5,7-tetranitro- 1,3,5,7-tetrazocine.

TNT = 2,4,6-Trinitrotoluene.

Explosive D = Ammonium picrate.

Comp B-3 = 60% RDX/40% TNT.

LX-10 = HMX/Viton[DuPont].

LX-16 = PETN(2,2-bis[{nitoxy}methyl]-1,3-propanediol dinitrate)/FPC 461 [Firestone].

LX-17 = TATB(2,4,6-trinitro-1,3,5-benzenetriamine)/Kel F [3M].

PBX-9404 = HMX/tris(2-chloroethyl)phosphate/nitrocellulose.

LP XM46 = Hydroxyammonium nitrate, triethanolammonium nitrate, and water.

NO_x is not expected to significantly contribute to the emissions. Grab-gas sampling has shown that NO is the principal NO_x species formed under these operating conditions, and the amount of NO_2 and N_2O were insignificant when compared to NO concentrations. The major combustion products are N_2, CO_2, and H_2O, and the amounts of NO_x and CO produced by the molten salt destruction process were relatively small. The levels are high enough that they may require downstream treatment in a commercial scale plant, but the untreated emissions are low enough to make any downstream treatment unit small in size.

We wished to compare the MSD process to more conventional thermal processes. For this comparison, we pumped LP XM46 (diluted 1:3 with water) at a propellant feed rate of 5.1 kg/h of into a moving packed bed of alumina spheres at 570°C. Under these conditions, 54% of the nitrogen in the liquid propellant was emitted as nitrogen oxides.[2] The principal nitrogen oxide species was NO_2, with NO levels 60% of the NO_2 levels. A trace of

N_2O was also produced. The amount of nitrogen oxides produced by destruction of LP XM46 using MSD is significantly less than for destruction in a packed-bed combustor.

To understand the reason for these lower emissions, we examined the composition of the salt bath after 2.5 L of diluted LP XM46 had been processed. The concentrations of nitrate and nitrite in the bed were 4.50% and 0.42%, respectively. Thus, roughly 50% of the nitrate in the LP XM46 remained in the salt bath after termination of the run. If additional fuel, such as 2-propanol, is injected after the bed has built up an inventory of nitrate, the concentration of nitrate in the bed drops and NO is the principal nitrogen oxide species emitted. Oxidation of the organic materials in the propellant by oxygen is faster than oxidation by nitrate in the feed. Additional fuel reduces the nitrate to NO. We may be able to produce lower emissions by enhancing the rate of oxidation of organic materials by nitrate.

It is well known that a number of transition metal ions can catalyze the oxidation of organic

materials and reduce nitrogen oxide emissions. Various catalytic materials were evaluated for their compatibility with carbonate molten salt baths. We found that V_2O_3, V_2O_5, $KCrO_4$, and $CoCO_3$ formed stable complexes in a mixture of lithium, potassium, and sodium carbonates at 650°C. We also found that $NiCO_3$, Fe_2O_3, and $CuCO_3$ were unstable under the above conditions and form insoluble metal oxide complexes, which are incompatible with the MSD process.

In addition to the carbonate eutectic our molten salt unit was loaded with 5 wt% of V_2O_5, and 400 g of RDX was processed through the unit. We found that the levels of incomplete combustion products and NO_x were identical to operation in the absence of vanadium.

In a separate series of experiments, the 7.5-kg unit was charged with 5 wt% of potassium chromate. Emissions with and without chromate are presented in Table 2. At a feed rate of 3.3 g/min, no uncombusted hydrocarbons are observed in either case. However, the concentration of CO is reduced by 36% and NO is reduced by 33% by the addition of chromate. At higher feed rates, the presence of uncombusted hydrocarbons is observed and the addition of chromate lowers the methane concentration by 37% and the ethylene concentration by 88%. No effect is seen on the NO or CO emissions at higher feed rates. We are investigating the detailed kinetics of decompo-

sition in the presence of chromate and investigating additional transition metals.

We evaluated the 7.5-kg MSD unit and determined that its residence time is too long to be useful in measuring the rapid destruction kinetics of energetic materials. A smaller, 200-g MSD unit was completed and installed in Building 241. We began a detailed kinetics study of the decomposition of RDX and TNT. These fundamental studies leverage the existing MSD program and allow incorporation of basic science that would not have been possible with existing funding. An understanding of kinetics and how transition metal catalysts influence the MSD process on a small scale will speed the implementation of the MSD process.

We continuously measured CO_2, CO/N_2, NO, H_2O and O_2 by mass spectrometry, and investigated the decomposition of TNT, RDX and several halogenated binders in the MSD bath. The eutectic mixture of lithium, sodium, and potassium carbonates used in both the small unit and the larger 1 kg/h unit has a working temperature down to 420°C. At these temperatures we obtained decomposition kinetics of the binders but the explosive decomposition was still too rapid to be measured.

We are investigating kinetics in a molten bath of lithium, sodium and potassium nitrates. These materials form a eutectic melting at

Table 2. Emissions with and without chromate.

	Comp B-3 feed rate		
	3.3 g/min	16.3 g/min	33.3 g/min
Emissions without CrO_4^- (ppm)			
NO	453	302	181
CO	106	124	131
Methane	ND^a	2290	4880
Ethylene	ND^a	5500	1730
Emissions with CrO_4^- (ppm)			
NO	302	241	181
CO	68	130	134
Methane	ND^a	1670	—b
Ethylene	ND^a	640	—b

[a] ND = not detected.
[b] Steady state not reached.

120°C, well below the decomposition temperature of most explosives, and will certainly allow us to make good kinetic measurements. The non-carbonate bath will also allow us to add varying amounts of carbonates and investigate whether carbonates catalyze the decomposition of energetic materials.

Conclusions

MSD produces lower emissions of NO_x than other thermal processes. This is principally due to the chemistry of interaction of the explosives and decomposition products with the reactive carbonates and the liquid phase reaction kinetics. Addition of transition metal salts to the carbonate salt bath, principally chromate, further decreases emissions of NO_x, CO, and hydrocarbons. We were unable to measure the decomposition kinetics of explosives in carbonate salt baths because the rates were too fast to measure in carbonate eutectic mixtures with low melting temperatures. We are currently investigating other salt mixtures with lower melting points to determine the kinetics of destruction in a liquid phase and the catalytic properties of the carbonate salt bath.

References

1. R. S. Upadhye, C. O. Pruneda, and W. A. Brummond, "Destruction of High Explosives and Wastes Containing High Explosives Using the Molten Salt Destruction Process," presented at the I&EC Special Symposium, American Chemical Society, Atlanta, Georgia, September 21–23, 1992.
2. R. J. Cena, C. B. Thorsness, T. T. Coburn, and B. E. Watkins (1993), *LLNL Demonstration of Liquid Gun Propellant Destruction in a 0.1 Gallon Per Minute Scale Reactor*, Lawrence Livermore National Laboratory, Livermore, CA, UCRL-ID-117549.

Publications

Upadhye, R. S., and B. E.Watkins (1994), *Destruction of the Liquid Gun Propellant LP XM46 Using Molten Salt Destruction Process*, Lawrence Livermore National Laboratory, Livermore, CA, UCRL-ID-116389.

Upadhye, R. S., B. E. Watkins, C. O. Pruneda, and W. A. Brummond (1994), *Energetic Material Destruction Using Molten Salt*, Lawrence Livermore National Laboratory, Livermore, CA, UCRL-JC-117252.

Upadhye, R. S., B. E. Watkins, C. O. Pruneda, and W. A. Brummond, "Molten Salt Destruction as an Alternative to Open Burning of Energetic Material Wastes," in *Proc. I&EC Special Symp.* (American Chemical Society, Atlanta, GA, in press).

Watkins, B. E., R. S. Upadhye, C. O. Pruneda, and W. A. Brummond, "Emissions from Energetic Material Waste during the Molten Salt Destruction Process," in *Proc. I&EC Special Symp.* (American Chemical Society, Atlanta, GA, in press).

Energetic Molecules

P. Pagoria, R. Schmidt, and A. Mitchell

Introduction

We are investigating the synthesis of high nitrogen energetic materials as gas generators for the development of new air-bag materials.

Progress to Date

In the consideration of new materials for gas-generator applications the most important criteria is that the gases produced are nontoxic. This puts limitations on the carbon and hydrogen content of the new gas-generator material because the presence of hydrogen or carbon may cause the formation of highly toxic HCN. With these limitations in mind, our research in the development of new air-bag materials has concentrated on two main areas: (1) polymers consisting of carbon and nitrogen (and possibly oxygen) only, and (2) high nitrogen energetic materials with low hydrogen content. The carbon–nitrogen polymers are interesting because these materials should produce only nitrogen and solid carbon upon decomposition. The high nitrogen energetic materials are known to be excellent gas generators, and keeping the hydrogen content low will reduce the possibility of HCN forming upon decomposition.

The carbon-nitrogen polymer research was based on our observation that the reaction of amines with sodium hypochlorite followed by treatment with activated charcoal caused an oxidative coupling of the amines, forming an N=N bond. We envisioned that this chemistry could be extended to compounds such as 3,6-diamino-1,2,4,5-tetrazine, which upon oxidation and coupling would give a polymer consisting only of carbon and nitrogen (Fig. 1). The reaction of 3,6-diaminotetrazine with sodium hypochlorite did not yield the expected N,N,N',N'-tetrachloro-3,6-diaminotetrazine; instead, the chlorine oxidation caused a ring-opening to yield 1,2,5,6-tetrachloro-1,3,4,6-tetraaza-1,3,5-hexatriene. The structure of this material was confirmed by x-ray crystallography.

Our investigation of other methods to effect the oxidative coupling of 3,6-diaminotetrazine (e.g., iodobenzene diacetate) have thus far given either starting material or decomposition products, but work is continuing in this area. Our investigation of the oxidative coupling of 5,5'-diamino-3,3'-bis-1,2,4-oxadiazole to yield a polymer consisting of only carbon, nitrogen, and oxygen using a variety of oxidizing reagents also led to either recovery of starting material or decomposition products.

The use of high nitrogen energetic materials, such as triaminoguanidinium nitrate, as components for gas generators has been known for some time. Recently, 5-aminotetrazole nitrate and 5-nitrotriazol-4-one have been suggested as possible air-bag materials. We have synthesized three thermally stable, high nitrogen energetic materials with good oxygen balance that may find use as air-bag materials: 2,6-diamino-3,5-dinitropyrazine-1-oxide; 3,5,7-triamino-s-triazolo-[4,3-a]-s-triazine dinitrate; and 3-amino-4,6-dinitropyridazine-1-oxide. We have also synthesized two dibenzo-1,3a,4,6a-tetraazapentalene derivatives, a class of compounds with attractive air-bag properties such as good thermal stability, high nitrogen content and heat of formation, and low or zero hydrogen content.
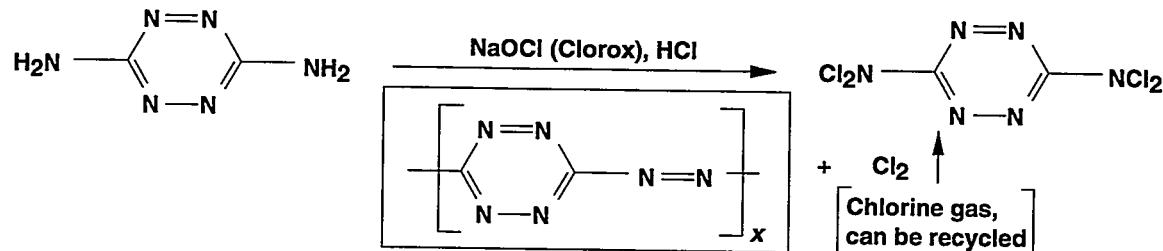

Figure 1. Proposed oxidation of 3,6-diamino-1,2,4,5-tetrazine with chlorine and activated charcoal.

Weapons-Supporting Research

Group Projects

Mechanical and Microstructural Properties of U–6Nb Alloys

G. Gallegos and A. Schwartz

Overview

Understanding the fundamental mechanisms that control the mechanical behavior of U–6Nb is important to weapons stockpile stewardship activities. The need to look at new and efficient methods to form this alloy, preferably at room temperature, requires understanding its behavior at large strains.

Technical Activities

We conducted torsion tests using thin-walled and thick-walled specimens in an effort to capture the "double-knee" effect at low strains and a "diffuse maximum" as reported by Vandermeer et al. on uniaxial tension studies of U–Nb alloys.[1] Because of difficulties associated with buckling in the thin-wall specimens, the inability to find microstructural evidence of deformation, and the need to look at large strain behavior, we conducted a series of tests using solid torsion specimens that have the same external geometry as the hollow specimens. The specimens included three "as-received" samples taken from a plate which was forged, rolled, quenched from the gamma phase to room temperature, and aged at 200°C. A fourth specimen, heat treated in the gamma-phase region at 1000°C for 24 hours, dropped to 800°C, then quenched, but not aged was also studied.

Results from these tests showed the effective strain to failure was about 55% for the as-received plates, whereas the specimen that was not aged had an effective strain to failure of 64%. These strain levels are greater than those achieved using the hollow specimens, which failed by buckling, and tensile data obtained by other investigators where the maximum elongations are on the order of 40% (presumably limited by necking). As expected, the sharpness of features in the early portion of the stress-strain curve is diminished, presumably

due to the strain gradient through the cross section of the solid specimen.

Figure 1 shows a photomicrograph of a cross section of a deformed torsion specimen. The curvature of the contrast lines (areas rich in niobium) suggests that the deformation is highly localized near the fracture surface.

Subsequent tests were performed in which lines were made on the gage section of the specimens to verify the localization phenomena. Figures 2, 3, and 4 show a sequence of photos of the specimens: undeformed, deformed to about 50% effective strain, and immediately prior to failure, respectively. They clearly show that these specimens deform uniformly through most of the test. However, immediately prior to failure, localized deformation occurs as shown by the discontinuity in the vertical gage mark.

Figure 5 is a photograph of failed torsion specimens. Specimen A was the as-received material, and specimen B was quenched (but not aged). The surface texturing on B appeared immediately upon twisting the specimen, along with a series of "bands" at approximately 45 deg from the axis of the specimen. No explanation has been formulated as yet to explain this difference.

We conducted microstructural studies in parallel with the torsion testing. Three-mm disks were extracted by spark machining from each torsion sample, lapped to a thickness of 125 µm, and electropolished to produce transmission electron microscopy (TEM) specimens. Prior to the examination of the deformed material, TEM characterization of the as-received specimens was carried out. To obtain a direct comparison of the effect of homogenizing and quenching vs forging and aging, the specimen that was heat-treated and quenched to room temperature was examined prior to mechanical deformation to compare the as-quenched and as-received microstructures. Figure 6 illustrates this as-quenched microstructure at (1) low magnification, showing
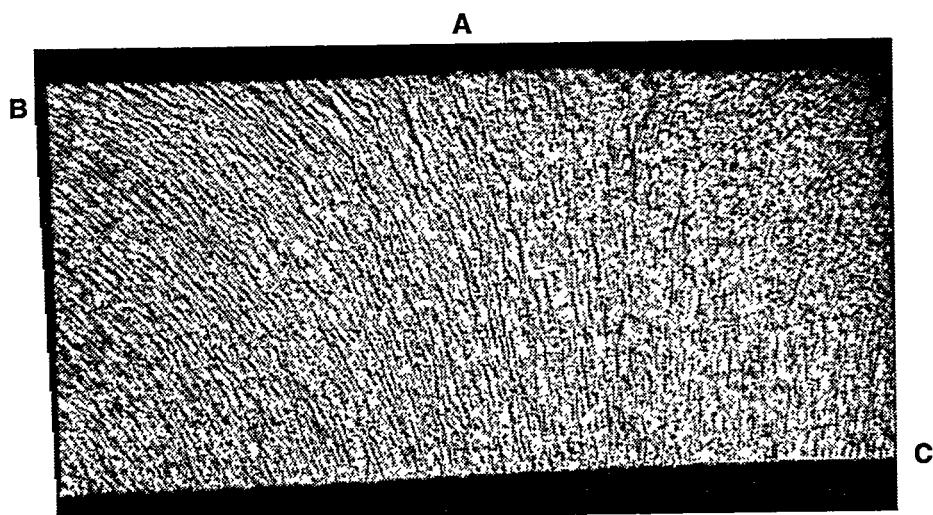
Figure 1. Photomicrograph taken at 10× of a U–6Nb torsion specimen in which the top of the specimen is the fracture surface. The relief "lines" (shown using differential interference contrast) are regions rich in niobium. At the center of the specimen (location A), the lines are vertical, as no straining occurred. The parallel lines are the result of the rolling operation of the plate where samples were taken. Maximum strain occurred at the outer surface (location B) and considerable strain occurred at the fracture surface. At location C, the lines are nearly vertical, suggesting strain localization.
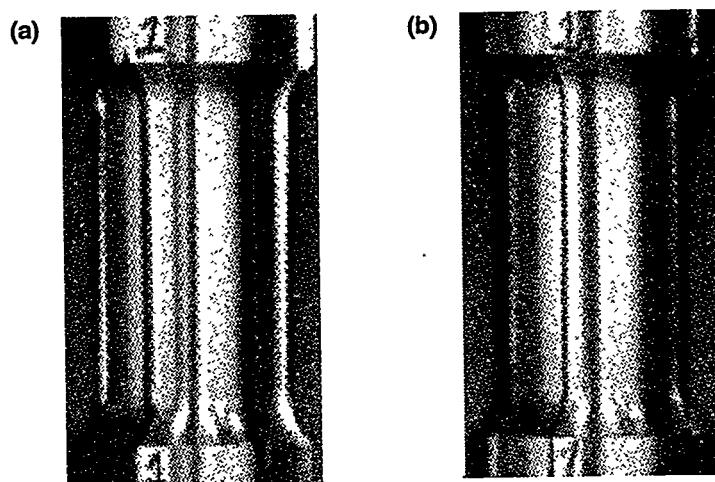
Figure 2. Undeformed specimens before torsion: (a) heat-treated U–6Nb and (b) not-heat-treated U–6Nb.

relatively large twin bands, and (2) higher magnification, revealing twins within the larger twin bands. The twin density and twin spacing are slightly different than those observed in the as-received condition, indicating that the forging and aging do, indeed, affect the microstructure. This observation is in agreement with the torsion testing data, which indicates that

the as-quenched material reached higher strain levels before fracture.

Next, specimens from the solid rod that had been deformed to failure were examined both longitudinally (along the axis of the torsion bar) and transversely (across the diameter). The transverse specimens were extracted by spark coring a 3-mm-diam rod
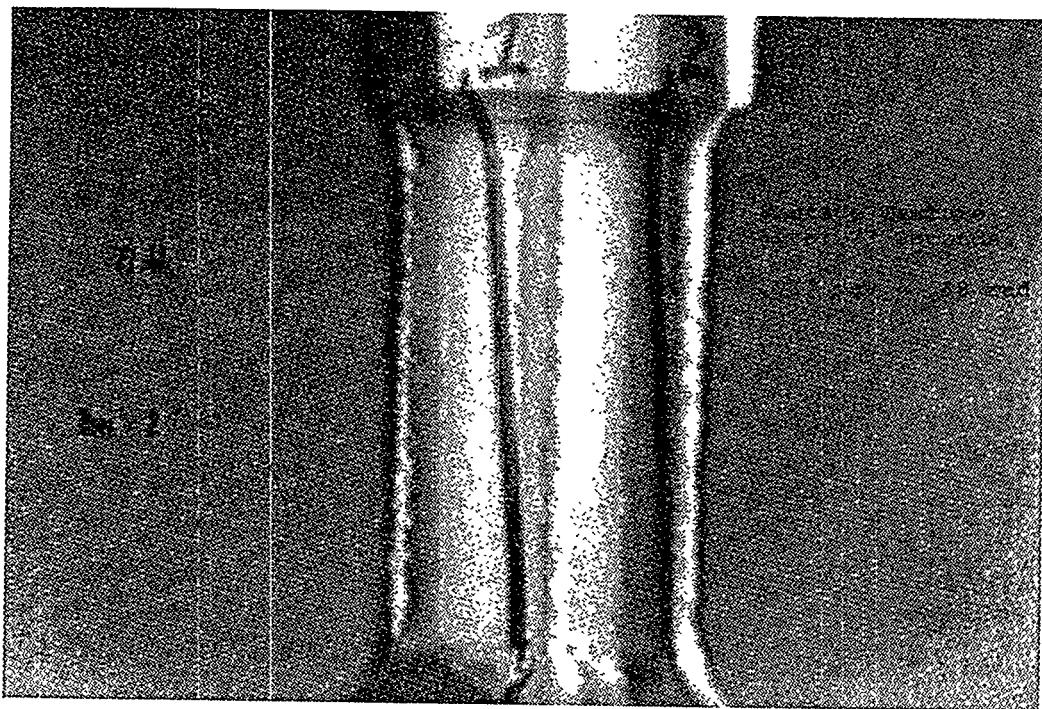
Figure 3. Specimen deformed to about 50% effective strain.
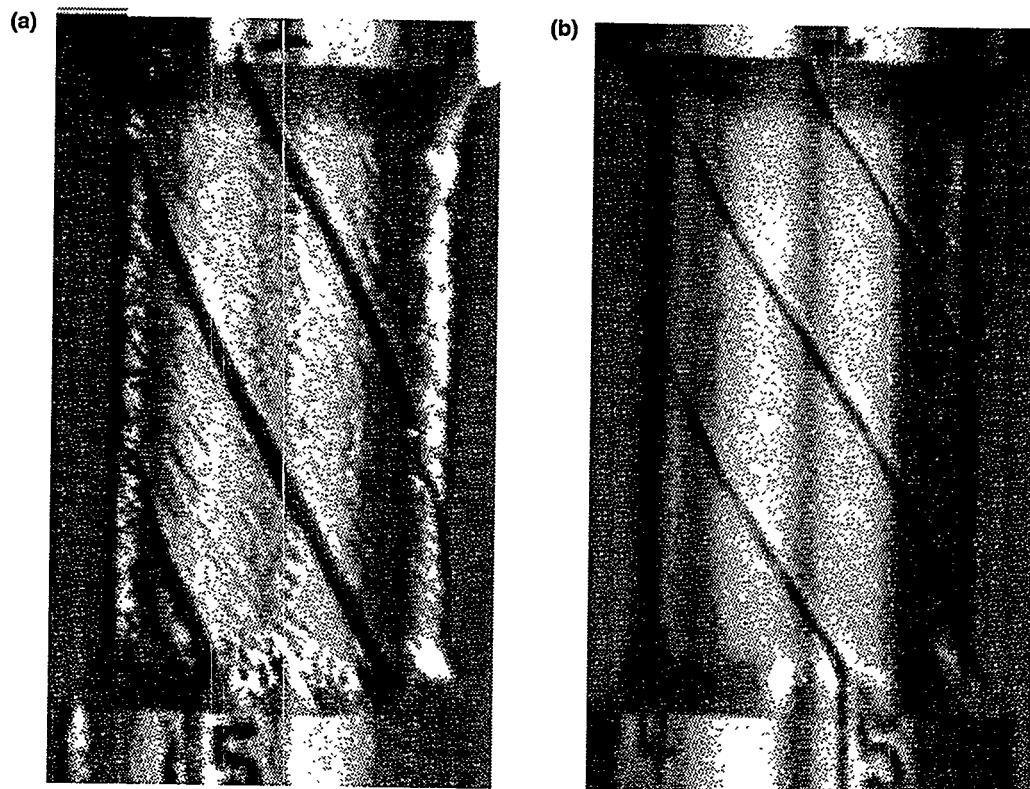
Figure 4. Deformed specimens just prior to fracture: (a) heat-treated U–6Nb and (b) not-heat-treated U–6Nb.

Figure 5. Photograph of the failed torsion specimens: A is as-received and B is as-quenched.

LAWRENCE LIVERMORE
NATIONAL LABORATORY
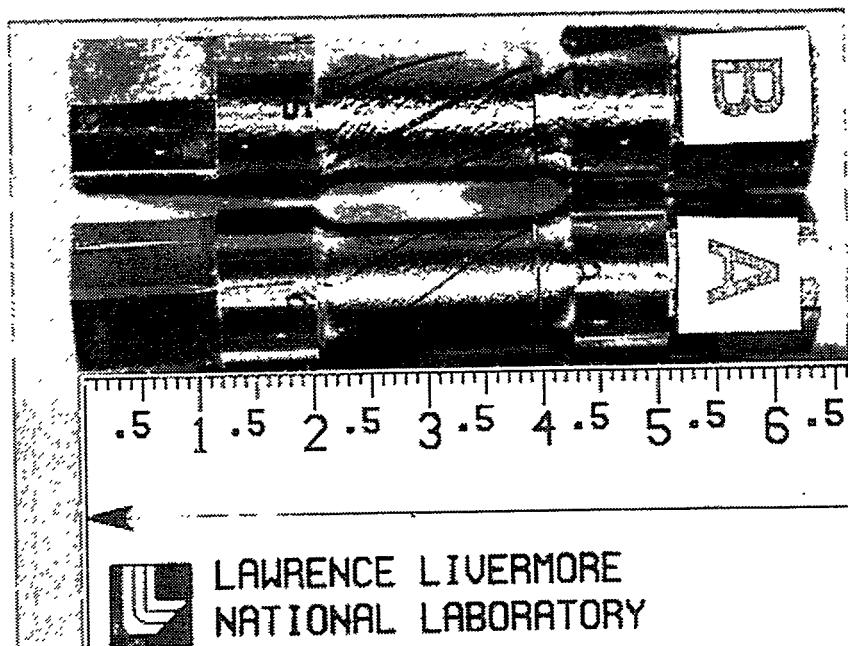
(a)
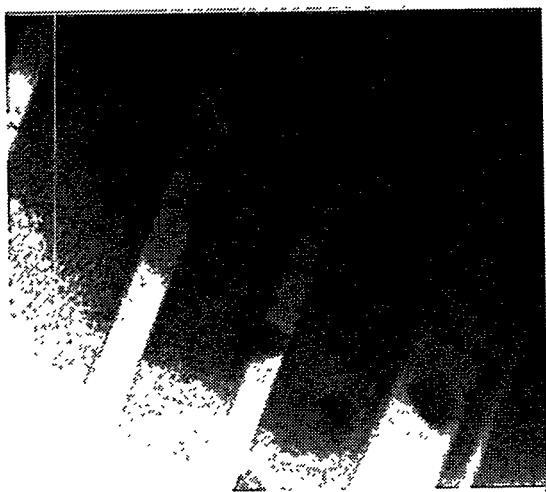
(b)
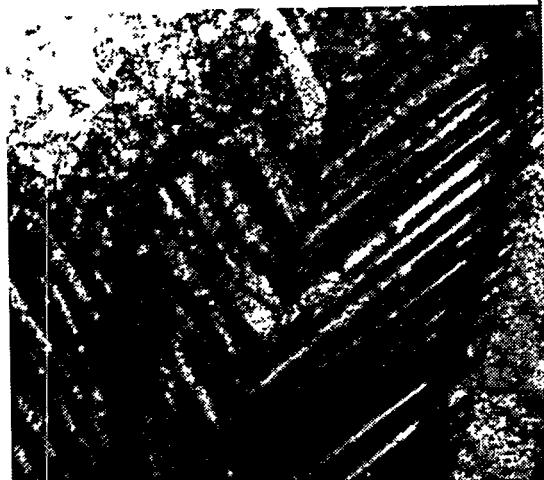
Figure 6. Microstructures of as-quenched U–6Nb: (a) low magnification (10,000×) bright-field TEM image revealing relatively large twin bands, (b) higher magnification (50,000×) bright-field image showing twins within the twins.

across the specimen near the fracture surface. This rod was then sectioned by a low-speed diamond saw to 300-mm thickness, lapped, and electropolished. By sectioning at such a thin level, 16 specimens across the diameter could be examined; this corresponds to the full range of strain levels across the diameter in Fig. 1. Figure 7 shows a bright-field TEM image taken from the center of the torsion bar that exhibits a microstructure similar to that of the unstrained as-received material. This is expected because at the center of the bar, little deformation is occurring.

Figures 8(a) and (b) are a TEM bright-field–dark-field image pair of the specimen taken from the outer radius, and Figs. 8(c) and (d) are two additional bright-field images. These micrographs reveal a highly twinned microstructure similar to as-received and as-quenched microstructures. Examination of other regions of this foil and other specimens near the outer radius have not revealed any dislocations or dislocation clusters. This is rather surprising because the strain levels are well past the second knee of the stress-strain curve where classic work hardening is expected.

Figure 7. Bright-field TEM image at 50,000× from a specimen at the center of the torsion bar (low strain).

Reference

1. R. A. Vandermeer, J. C. Ogle, and W. C. Northcutt, Jr., "A Phenomenological Study of the Shape Memory Effect in Polycrystalline Uranium–Niobium Alloys," *Met. Trans. A* **12A**, 733–741 (1981).
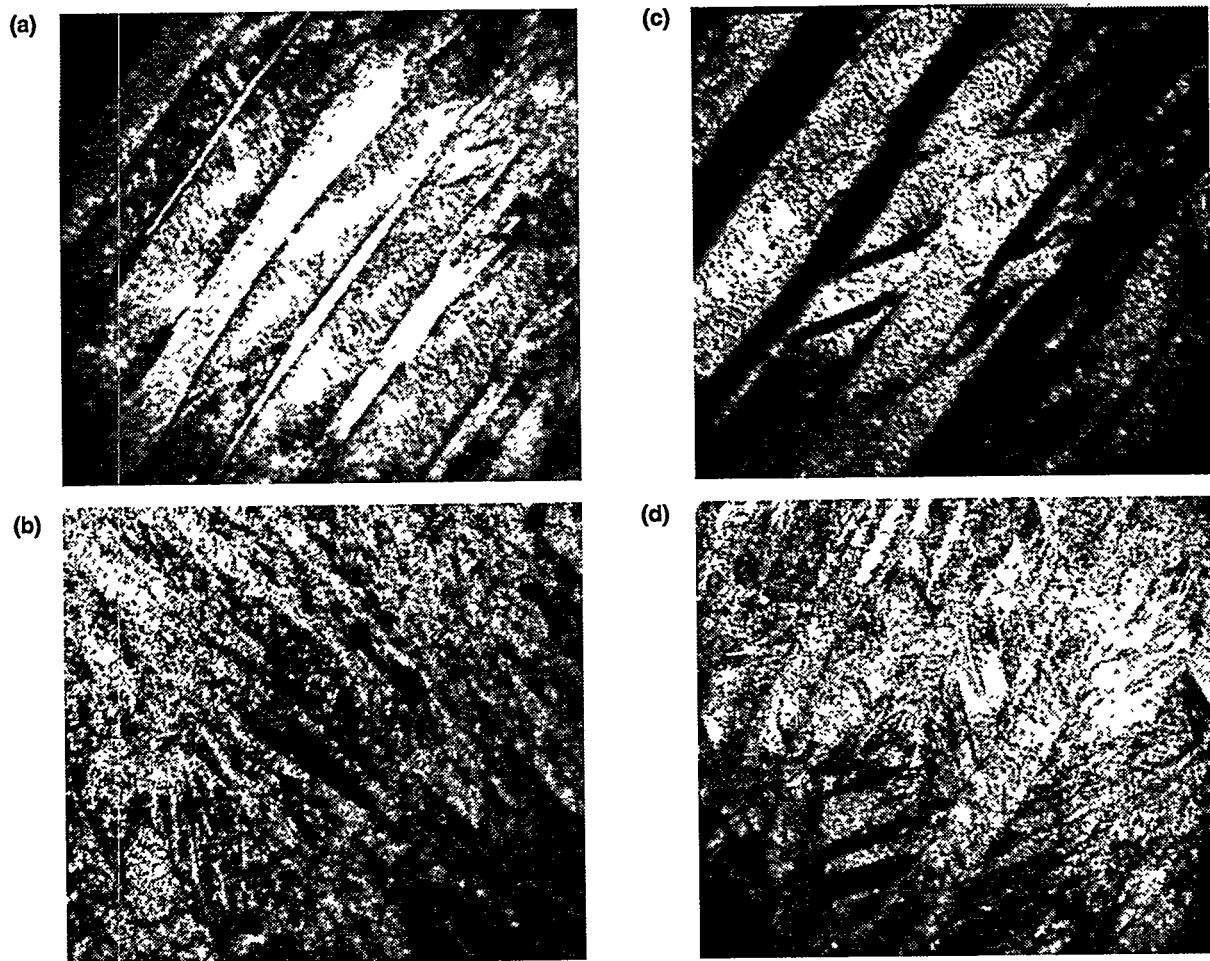
**Figure 8. Microstructures of the solid torsion bar at 50,000×: (a) Bright-field image from the outer radius; (b) dark-field image corresponding to (a); (c) and (d) bright-field images from the outer radius.**

Advanced Synchrotron Radiation Study of Materials

Joe Wong, M. Fröba, P. A. Waide, and J. W. Elmer

Overview

Our objective is to advance and develop state-of-the-art synchrotron radiation (SR) methods to investigate and elucidate the role of atomic and electronic structures in determining the physicochemical properties of materials and their processing. Our activities take advantage of the unique characteristics of SR such as high intensity, high collimation, high polarization, and broadband tunability from vacuum ultraviolet to soft and hard x rays to probe the structure of matter on an element-selective basis in real time (down to second and subsecond time scales) and in real space. We are expanding our existing SR capabilities in material characterization using these powerful photon sources and developing new capabilities to (1) investigate in situ mapping of phase boundaries in fusion welds; (2) develop and implement a novel, quick-scanning extended x-ray absorption fine structure (QEXAFS) capability on our participating research team (PRT) x-ray beamline at the Stanford Synchrotron Radiation Laboratory (SSRL) to study time-dependent phenomena; and (3) develop new soft x-ray capabilities to study low-Z materials containing silicon, aluminum, and magnesium that are of technological importance. The latter activity received a Laboratory Directed Research and Development award at the start of FY94.

The following is a summary of our technical accomplishments for this reporting period:

- Facilitated the use of the newly installed QEXAFS capability on beamline 10–2 to obtain high-quality, multi-edge EXAFS spectra in a series of rare-earth cuprates, $RE_2Cu_2O_5$.

- Identified the chemical states of metal constituents in transition metal–silica aerogel materials.

- Developed a spatially resolved x-ray diffraction (SRXRD) technique using SR and applied it successfully to map the phases present in the heat-affected zone (HAZ) of fusion welds in situ and in real time.

Progress

Multi-Edge EXAFS Scans

The signal statistics in EXAFS measurements of bulk, moderately concentrated samples are not limited by the synchrotron photon flux, but rather by the mechanical instability of the monochromator as it is rotated from one position to another in the conventional point-by-point measurement. If a stable monochromator can be slewed in a quasi-continuous manner and intensity recorded "on the fly," much of the undesirable mechanical noise due to start-and-stop motion in the point-by-point mode may be avoided. This forms the basis of the QEXAFS procedure as conceived and demonstrated by Frahm.[1] The key instrumentation in a QEXAFS setup is the employment of a micro-stepper to provide a large number of motor steps (e.g., 80,000 steps/deg). Given this implementation,

$$t_Q \approx 80,000 \frac{\theta_i - \theta_j}{r} ,$$ (1)

and

$$N = \frac{t_Q}{c} .$$ (2)

where t_Q is the time of a QEXAFS scan; θ_i and θ_j are the initial and final energy Bragg angles (deg), respectively; r is proportional to the scan rate (steps/s); c is the counting time per data point (s/point); and N is the number of data points. The versatile QEXAFS technique can be used in the transmission, fluorescence, e-yield, and glancing angle modes. Samples may be in bulk, dilute, powder, or thin-film form. Such a QEXAFS setup is a one-time installation and may be turned on and off by software. Applications of the QEXAFS technique include survey scans for optimization, recording of "normal" EXAFS spectra, and time-resolved studies in the seconds time regime.

In a June 1993 run at SSRL, we installed a permanent QEXAFS setup on beamline 10-2

and tested successfully all of its functions and capabilities. In February 1994, we took advantage of the *beam time efficient* aspect of the technique to investigate the site-specific chemistry of a series of rare-earth cuprates, $RE_2Cu_2O_5$, where RE = terbium, dysprosium, holmium, erbium, thulium, ytterbium, and lutetium. We also recorded systematically a set of multi-edge EXAFS spectra of all metal constituents in each material. Figure 1 shows a raw experimental EXAFS scan for $Tm_2Cu_2O_5$ over an energy range of 2000 eV. This contains both the $L_{3,2,1}$-edge spectra of thulium and the K-edge spectrum of copper. The spectrum was scanned with a step size of 0.5 eV and 0.1 s integration per point and took just under 7 min to record. The conventional point-by-point method would have required 2 h.

The QEXAFS method, therefore, enables a more efficient use of beam time by eliminating the dead time loss between data points in the conventional method. A comprehensive QEXAFS users manual has been completed and is now available for distribution. In July 1994, an on-line tutorial session was scheduled to demonstrate this new spectroscopic capability to a number of interested University of California–national laboratory PRT members.

Chemical States of Metal in Transition Metal–Silica Aerogels

Metal oxide-based aerogels are potentially useful as catalytic materials. In the as-prepared state these materials are usually amorphous, making phase identification and structure elucidation by conventional diffraction rather uninformative. X-ray absorption spectroscopy is a tool of choice because the XANES spectrum near the absorption edge of a given constituent element is characteristic of the chemical bonding and coordination geometry of that element. The EXAFS spectrum at higher energy yields bond distance and coordination number and type of nearest neighbors surrounding a given atom in the structure. In this reporting period, we measured the EXAFS spectra of a series of transition metal-silica aerogels containing titanium, vanadium, cobalt, nickel, copper, zirconium, and tantalum. Figure 2 shows the vanadium K-edge XANES of a vanadium–silica containing 5 wt% of metal. A prominent and well-defined pre-edge peak is observed in this aerogel material. This pre-edge absorption feature is characteristic of pentavalent vanadium in a square pyramid coordination with oxygen as in crystalline V_2O_5.[2] Figure 2 also shows for comparison the normalized vanadium K-edge XANES of V_2O_5. In Figure 3, the tantalum L_3 XANES spectrum of a pure tantala aerogel is plotted with the corresponding spectra for tantalum metal and crystalline Ta_2O_5. A strong white line dominates the XANES spectrum because of a transition from initial p to final d states, which are relatively empty in this early $5d$ metal. Of particular interest is the observed edge shift of the
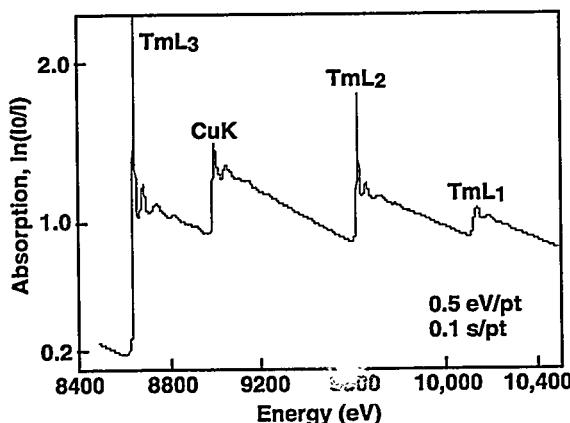

Figure 1. An experimental QEXAFS scan of thulium $L_{3,2,1}$-edge and copper K-edge of $Tm_2Cu_2O_5$ over a 2000-eV range.
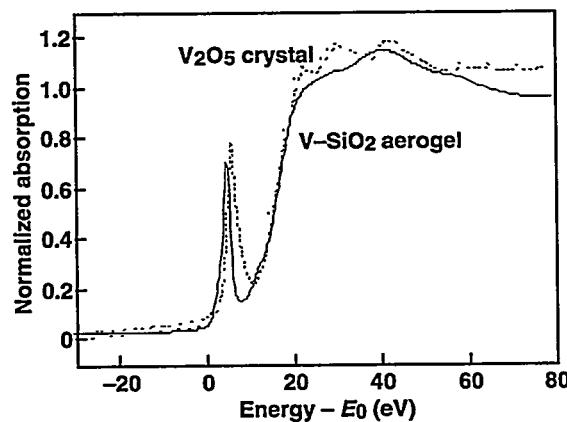

Figure 2. Normalized vanadium K-edge XANES of a V–SiO$_2$ aerogel containing 5 wt% of vanadium and V_2O_5 model compound. E_0 is the K-edge absorption energy of vanadium metal at 5465 eV.

tantalum site in the aerogel material with respect to that of the tantalum metal. This shift is identical to that of Ta_2O_5 indicative of a pentavalency of the tantalum site in the aerogel material. Analysis is now underway to elucidate other transition metal sites in the series of metal silica aerogels measured.

Direct Observation of Phase Transformation in Fusion Welds

We developed a SRXRD technique using SR and applied it successfully to map the phases present in the HAZ of fusion welds in situ and in real time. For the case of a 1.9-kW arc weld in commercially pure titanium, which exhibits an allotropic transformation from a hexagonal close-packed (hcp) α-phase to a body-centered cubic (bcc) β-phase at about 922°C, the following results were obtained:

- The width of the HAZ adjacent to the liquid weld pool was found to be 3.33 ± 0.33 mm as determined by the existence of the high-temperature bcc phase in this zone. This experimental width corroborated well with that calculated from a scaled-up heat-flow model.
- Concentration profiles derived from the SRXRD data revealed coexistence of both α- and β-phases in the HAZ.

These results represent the first direct observation of solid-state transformation and mapping of phase boundaries in fusion welds. These results also provide the needed experimental inputs for modeling of kinetics of phase
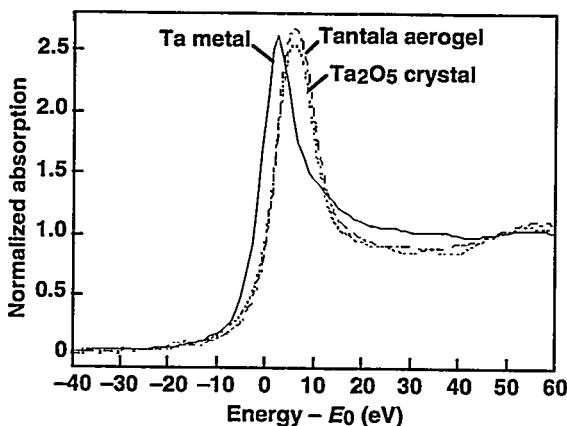
transformation and microstructural evolution in allotropic and other more complex systems under steep thermal gradients and nonisothermal heating conditions.

Figure 4 shows the SRXRD setup and welding apparatus. The synchrotron beam emerging from the wiggler was focused by a toroidal mirror, passed through a 1-mm entrance slit, and monochromatized with a double Si(111) crystal. The monochromatic beam was then collimated with a Huber slit to render a submillimeter beam on the sample at an incident angle of about 25 deg. An energy of 8.5 keV ($\lambda = 1.45860$ Å) for the incident beam was chosen as an optimum energy to (1) maximize the penetration depth in titanium (~26 μm), which was sufficient to reduce the signal contribution from any thin oxide layer (~100 Å) that might form during the welding process; (2) minimize the background contribution due to titanium K-fluorescence from the sample (titanium K-edge at 4966 eV); (3) stay within the specified detection efficiency range (<10 keV) of the silicon photodiodes; and (4) maximize the range of 2θ to collect an adequate number of diffraction peaks for both hcp and bcc phases of titanium for phase identification. The diffracted beams were collected using a thermoelectrically (Peltier) cooled 2048 element position-sensitive silicon photodiode array detector to cover a 2θ range of about 30 deg. The detector and its associated ST1000 data collection software were supplied by Princeton Instruments.

Figure 5 shows the results of a point-by-point phase mapping along the y-direction from the base titanium material into the HAZ. Figure 5(a) illustrates the path taken by the submillimeter beam "scanning" sequentially in steps of 0.33 mm from a point 5 mm behind the center of the weld (+ in the liquid pool) and 11 mm from the centerline of the weld. A diffraction pattern was recorded at each location with a 10-s integration time. A selected set of x-ray diffraction patterns was plotted to show the critical phase changes along the path. Thus, beginning at $y = 11$ mm, the diffraction pattern was that of the hcp titanium at some temperature below the α→β transition temperature. This pattern yielded the expected five low-angle reflections of hcp titanium calculated for the powder pattern. The high peak intensity of the observed (002) reflection indicates that the surface of the titanium cylinder is highly textured with the basal planes oriented nearly parallel to the surface.


Figure 3. Normalized tantalum L-edge XANES spectra of a pure tantala aerogel, Ta_2O_5, and tantalum metal. E_0 is the L-edge absorption energy of tantalum metal at 9881 eV. Scan time = 6.7 min.
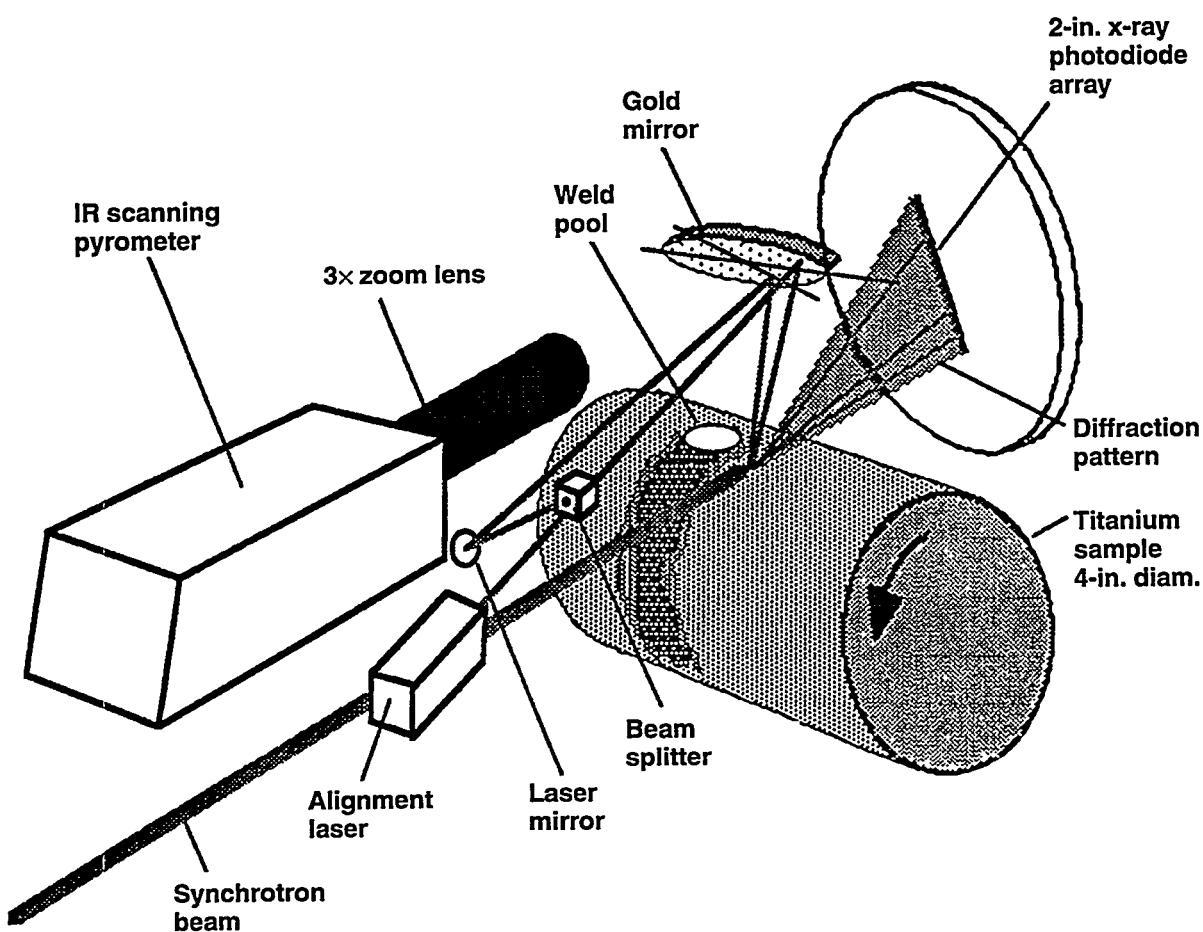
Figure 4. Schematic diagram of the SRXRD setup used for in situ phase transformation and mapping in fusion welds.

Between $y = 11$ mm to $y = 9.33$ mm, only the sharp hcp pattern was observed. As the beam was "scanned" deeper into the HAZ toward the liquid pool, two notable changes in the SRXRD pattern took place concurrently. At $y = 9$ mm, a shoulder on the low-angle side of this hcp (002) reflection emerged simultaneously with the appearance of the bcc (110) reflection. Figure 5(b) clearly shows these two features. The bcc (110) reflection increased in intensity from $y = 9$ mm to $y = 7$ mm, then decreased from $y = 6.66$ mm, and persisted at $y = 5.66$ mm. Also, from $y = 9$ mm inward, the shoulder feature on the low-angle side of the sharp hcp (002) reflection increased in intensity and evolved at $y = 7.33$ mm into a well-defined peak, displacing the narrow reflection completely at $y = 7$ mm. This is indicative of expansion of the hcp lattice along the positive temperature gradient toward the liquid pool. Also at $y = 7.33$ mm, low-angle shoulder features are evident from both (101) and (102) reflections

of the hcp phase. This is expected because both of these (*hkl*) reflections have a non-zero *l* value.

The relative fractions of the α- and β-phases in the HAZ may be estimated from the normalized peak intensities of the (002) reflection of the hcp phase and the (110) reflection of the bcc phase, respectively. For each phase, normalization was performed with respect to the corresponding strongest peak in the series of SRXRD patterns recorded along the path indicated in Fig. 5(a). These intensity profiles are plotted in Fig. 6. By defining the region containing the bcc phase as a measure of the width of the HAZ, which is clearly seen from the intensity profile of the (110) reflection of the bcc phase, a value of 3.33 ± 0.33 mm may be deduced. This value was reproducible experimentally in a series of five SRXRD runs conducted in the same region with respect to the center of the weld pool using the same welding parameters. Moreover, the experimental value agrees well with a value of about 3 mm
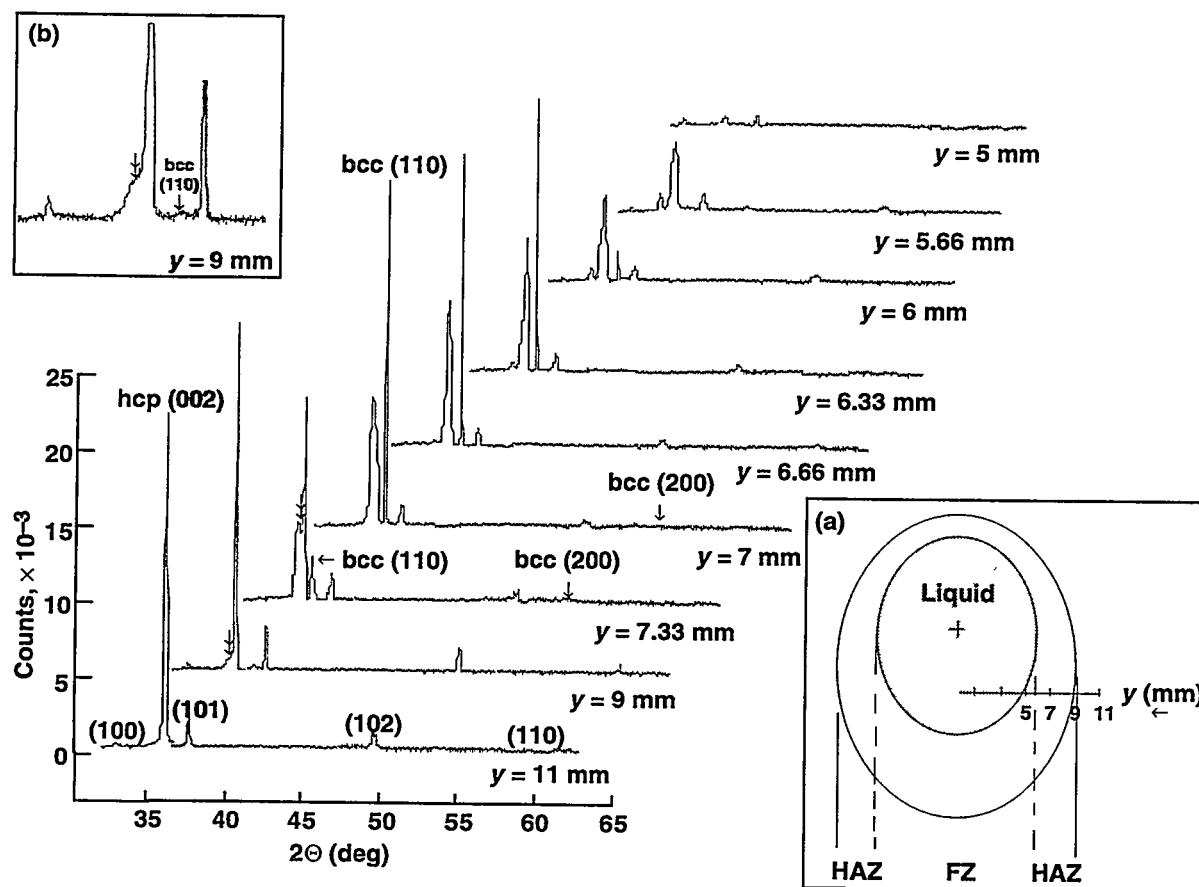
Figure 5. Selected SRXRD diffraction patterns as a function of position in the HAZ of a titanium fusion weld. (a) Schematically the path taken by the x ray, 0.5 mm × 0.25 mm in size, from the base material to the HAZ toward the liquid pool. The starting position at y = 11 mm is about 5 mm behind the center of the weld pool, which is denoted by the cross mark. (b) Expanded SRXRD pattern at location y = 9 mm, showing a discernible appearance of the bcc (110) reflection between the hcp (002) and hcp (101) reflections.

calculated from a scaled-up heat-flow model under the same thermal input power.

Although the spatial range of occurrence for the bcc phase correlates well with the calculated locations of the HAZ, the existence of a minute amount of hcp phase and total absence of the bcc phase near the melt at y = 5 mm (see also Fig. 5) appear an anomaly; however, it was reproducible from run to run. This may be caused by local fluctuations in the position of the weld pool with respect to the x-ray probe arising from lateral instabilities in the dynamic weld pool. Also, scattering in the intensity profile of the α-phase, particularly outside the HAZ in the range y = 11 to 8 mm, is largely caused by texturing of the titanium base material discussed above. Thus, under the present experimental conditions, concentrations of phases from such intensity profiles are at best semiquantitative.

A significant result of the present in situ SRXRD measurements is the coexistence of the α- and β-phase in the HAZ about the titanium fusion weld. This fact, not readily obtainable with either conventional structural techniques (because of their ex situ and postmortem nature) or simple heat flow calculations, must be taken into account in the kinetic modeling of phase transformation and microstructural evolution in allotropic systems under highly nonisothermal conditions. The present results are very encouraging and demonstrate experimental feasibility of our SRXRD technique to determine the phases and their boundaries in situ and in real time during the welding process. With the aid of further experimental refinements using a combination of more stabilized welds and smaller size probes from third-generation bright synchrotron sources such as those at ESRF (Grenoble) and
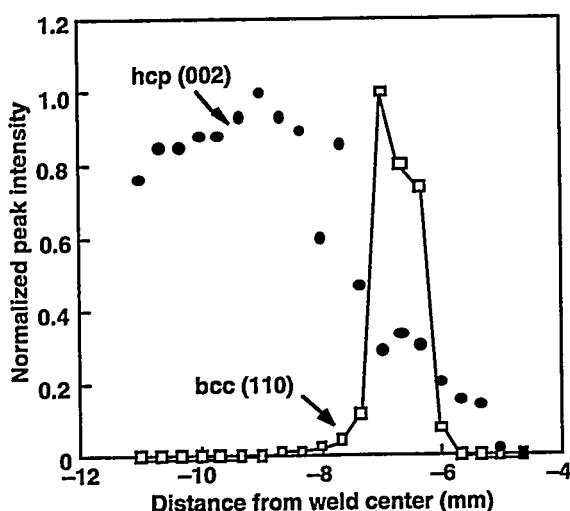
Figure 6. Normalized peak intensity profiles for the (002) reflection of hcp α-titanium and the (110) reflection of bcc β-titanium showing the relative fraction of each phase as a function of distance from the weld center. Normalization was performed with respect to the corresponding strongest peak in the series of SRXRD patterns recorded along the path depicted in Fig. 5(a).

APS (Argonne), we plan to obtain more complete and finer spatially resolved phase mappings of fusion welds with large imaging plates.[3] These data will then be used to develop a generalized model of phase-transformation behavior in welds to predict microstructural evolution in both the HAZ and fusion zone and to verify the model for both allotropic phase transformations occurring in titanium and those occurring in two-phase stainless steel alloys that are of prime importance in a variety of modern core technologies.

References

1. R. Frahm, *Nucl. Instrum. Methods* **A270**, 578 (1988).
2. J. Wong, et al., *Phys. Rev. B* **30**, 5596 (1984).
3. T. Hamaoka, *Cell Technol.* **9**, 456 (1990).

Publications

A. Chaiken, L. J. Terminello, J. Wong, G. L. Doll, and C. A. Taylor, II (1993), "Electronic and Atomic Structure of Metastable Phase in BN Using Core Level Photoabsorption," *Appl. Phys. Lett.* **63**, 2112.

J. Wong, G. N. George, I. I. Pickering, Z. Rek, M. Rowen, T. Tanaka, and B. DeVries (1994), "New XAFS Spectroscopic Investigations in the 1–2 keV Region," *Solid State Comm.* **92**, 559.

J. W. Elmer, Joe Wong, M. Fröba, P. A. Waide, and E. M. Larson, "Analysis of Heat Affected Zone Phase Transformations Using In Situ Spatially Resolved X-Ray Diffraction with Synchrotron Radiation," *Met. Trans.* (submitted).

Joe Wong, J. W. Elmer, M. Fröba, P. A. Waide, and E. M. Larson, "Direct Observation of Phase Transformation in Fusion Welds," *Science* (submitted).

Invited Talks

MAX-Lab Annual Users Meeting, Lund, Sweden, "Performance of a YB$_{66}$ Double Crystal Monochromator in the 1–2 keV Region" (September 1993).

20th Annual SSRL User Meeting, Stanford, "New XAFS Spectroscopic Investigations in the 1–2 keV Region: The YB$_{66}$ Story" (October 1993).

Seminar, Department of Geological and Environmental Science, Stanford University, "QEXAFS and New Soft X-Ray Experimental Capabilities for Materials Study" (November 1993).

The 43rd Annual Denver Conference on Applications of X-Ray Analysis, Steamboat Springs, CO, "Dynamic Characterizations of Reactions," (August 1994).

ACS Symposia on Synchrotron Radiation Applications to Industrial Problems, Washington DC, "New Synchrotron Studies of Si-, Al- and Mg-Bearing Materials" (August 1994).

Materials Physics Seminar, Hamburger Synchrotron Lab, (HASYLAB), Hamburg, Germany, "New Opportunities in XAFS Spectroscopy in the 1–2 keV Region" (September 1994).

Dow Chemical Research Laboratory, Midland MI, "New Structural Probe for Si-, Al- and Mg- Materials with XAFS Spectroscopy" (December 1994).

Materials Physics Seminar, Illinois Institute of Technology, Chicago, IL, "Recent Advances in XAFS Spectroscopy for Materials Research" (December 1994).

Full-Potential Multiple Scattering Theory—The Poisson Equation

J. M. MacLaren,[*] J. van Ek, and A. Gonis

Overview

Electronic structure theory provides a framework for accurately predicting many properties of condensed matter systems, including ground-state crystal structures, elastic constants, and formation energies. To predict many of these properties in geometries in which the atoms are not close-packed, it is necessary to employ methods that treat the exact form of the potential throughout the unit cell, rather than its spherical average.

The methods used in our treatment of the electronic structure of solids are based on the framework of multiple scattering theory (MST). Electronic structure techniques based on MST have a number of attractive features: the ability to treat defects such as interfaces, surface and point defects, and the ability to treat disorder through the use of the coherent potential approximation. Unfortunately, these methods have been implemented almost exclusively within the muffin-tin approximation, which is only suitable for a close-packed atomic arrangement. There is a clear need to extend these techniques to a full-potential treatment. In a self-consistent electronic structure calculation, one needs to solve both the Schrödinger and Poisson equations. These equations are similar and will be solved using similar methods. Here, we discuss the solution of the Poisson equation.

Progress

The Poisson equation has been solved using three different cellular approaches: (1) the conventional multipole structure constant summation resulting from MST; (2) a Green's function cellular method; and (3) a variational cellular method (VCM).[1] The latter technique appears to have the best numerical convergence and has been implemented in the full potential electronic structure code. The solution to the Poisson equation can be written in terms of Green's functions by

$$V(\mathbf{r}) = \int d\mathbf{r}' \, G(\mathbf{r},\mathbf{r}') \, \rho(\mathbf{r}') \ , \tag{1}$$

where

$$G(\mathbf{r},\mathbf{r}') = \frac{1}{|\mathbf{r}-\mathbf{r}'|} \ , \text{ and} \tag{2}$$

$$\nabla^2 G(\mathbf{r},\mathbf{r}') = 4\pi\delta(\mathbf{r}-\mathbf{r}') \ . \tag{3}$$

In the cellular treatment, we divide space up into a collection of cells, where a local solution $v_n(\mathbf{r})$ to the Poisson equation is found by direct integration. This solution is only required to satisfy the Poisson equation within its cell. The global solution can be found, and it is

$$V_n(\mathbf{r}) = v_n(\mathbf{r}) - \frac{1}{4\pi}\sum_{n'}\int d\mathbf{r}'_{n'}$$

$$\left[G(\mathbf{r}_n,\mathbf{r}'_{n'})\nabla'^2 \, V_{n'}(\mathbf{r}'_{n'}) - V_{n'}(\mathbf{r}'_{n'})\nabla'^2 \, G(\mathbf{r}_n,\mathbf{r}'_{n'}) \right] \ . \tag{4}$$

By expanding the Green's function we arrive at the solution

$$V_n(\mathbf{r}) = v_n(\mathbf{r}) - \sum_L \frac{J_L(\mathbf{r}_n)}{(2l+1)} \sum_{n'}\left[H_L^n, V_{n'} \right]_{n'} \ , \tag{5}$$

where J_L and H_L are regular and irregular solutions to Laplace's equation and $[H_L,V_n]_n$ denotes a surface Wronskian taken over the cell surface. As expected, the local solution is corrected by an appropriate sum of regular solutions to Laplace's equation. We found that using an extended charge density (i.e., one that is not truncated to zero outside its cell) gives the best numerical stability. By replacing the surface integration by a volume integral

[*]Department of Physics, Tulane University, New Orleans, LA.

(Green's theorem), the usual structure constant multipole expansion can be recovered.

These methods have been tested on several trial densities for which exact solutions are known. Figure 1 shows one VCM approach.

References

1. X.-G. Zhang, W. H. Butler, J. M. MacLaren, and J. van Ek, *Phys. Rev. B* **49**, 13383 (1994).
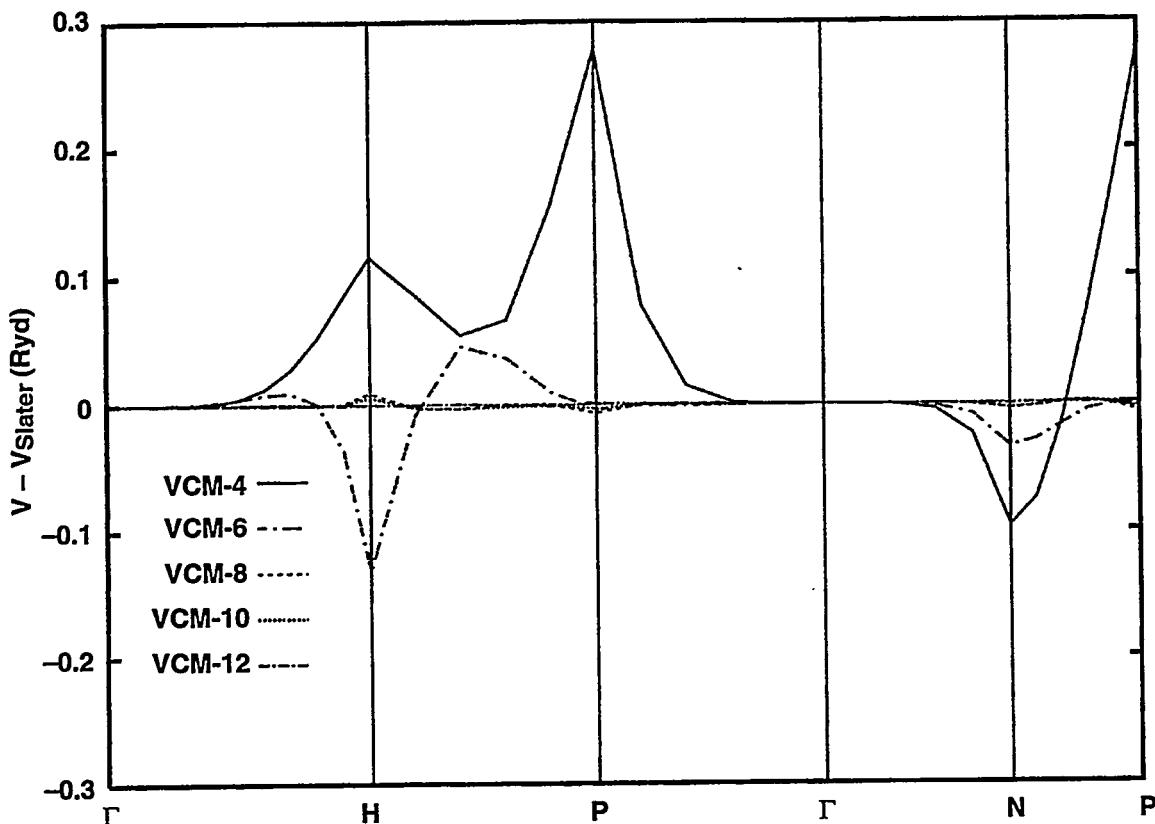
Figure 1. The errors and convergence for the Slater potential at various points along the surface of the face-centered cubic Wigner–Seitz cell. Although all the methods converge, VCM has the fastest rate of convergence.

Electronic Structure of Metallic Alloys

P. P. Singh and A. Gonis

Overview

We developed the theoretical and computational frameworks for studying, from first-principles, the ground-state properties and the phase stability of ordered and disordered alloys. We also incorporated in our codes the effects of charge transfer in disordered alloys, and we are now working on including the strain effects due to the size mismatch. To make reliable predictions about the phase stability of alloys, we formally extended the generalized perturbation method to include the total energy of a disordered alloy.

Progress

Our approach allows us to calculate the electronic structure of ordered and disordered alloys within the same framework. This approach is based on the screening transformation of the linear muffin-tin orbitals (LMTO) and the Korringa-Kohn-Rostocker–coherent potential approximation method. The advantages of our formulation include (1) an efficient calculation of electronic structure of ordered and disordered alloys with the same set of approximations for the Hamiltonians in each case, (2) minimization of charge-transfer effects by employing charge-neutral spheres, and (3) a probable improvement over the muffin-tin formulation for those alloys in which the potential in the interstitial region is not constant.

Based on our approach, we calculated the total energies and the effective cluster interactions of several metallic alloys. In particular, we studied the energetics of ordered and disordered nickel–platinum alloys over the whole concentration range. For example, in Fig. 1, we show the formation energies and the ordering energies of nickel-platinum alloys calculated nonrelativistically and scalar relativistically. We found that the relativistic effects also play an important role in changing the most stable structure from hexagonal close-packed to

rhombohedral as one goes from zinc to mercury.

For studying more complex systems than is feasible with the conventional electronic structure methods, we carried out preliminary studies on the transferability of the LMTO tight-binding parameters using the nickel–aluminum system.

In the future, we plan to study the combined effects of chemical order and local atomic displacements on both the electronic structure and the phase stability of alloys.

Publications

P. P. Singh and A. Gonis, "The Origins of Phase Stability in Ordered and Disordered Ni-Pt Alloys," submitted to *Phys. Rev. B*.

P. P. Singh (1994), "From Hexagonal Close-Packed to Rhombohedral Structure: Relativistic Effects in Zn, Cd, and Hg," *Phys. Rev. Lett.* **72**, 2446–2449.

M. H. F. Sluiter and P. P. Singh (1994), "Transferable Tight-Binding Parameters: An Application to Ni and Ni–Al Alloys," *Phys. Rev. B* **49**, 10918–10925.

P. P. Singh (1994), "Relativistic Effects in Mercury: Atom, Clusters, and Bulk," *Phys. Rev. B* **49**, 4954–4958.

P. P. Singh and A. Gonis (1994), "Electronic Structure of Metallic Alloys Using Charge-Neutral Atomic-Spheres," *Phys. Rev. B* **49**, 1642–1646.

Presentations

P. P. Singh and A. Gonis (1994), "Electronic Structure of Metallic Alloys Using Charge-Neutral Atomic-Spheres," *Bull. Am. Phys. Soc.* **39**, 802.

A. Gonis, P. P. Singh, E. C. Sowa, and P. E. A. Turchi (1994), "Generalized Perturbation Method Expansion of the Total Energy of Substitutional Alloys," *Bull. Am. Phys. Soc.* **39**, 747.

P. P. Singh and A. Gonis, "Electronic Structure of Ordered and Disordered Alloys in the Atomic-Sphere Approximation," *TMS Fall Meeting on Alloy Modeling* (Pittsburgh, PA, 1993).

A. Gonis and P. P. Singh, "Generalized Perturbation Method Expansion of the Total Energy of Substitutional Alloys," *TMS Fall Meeting on Alloy Modeling* (Pittsburgh, PA, 1993).
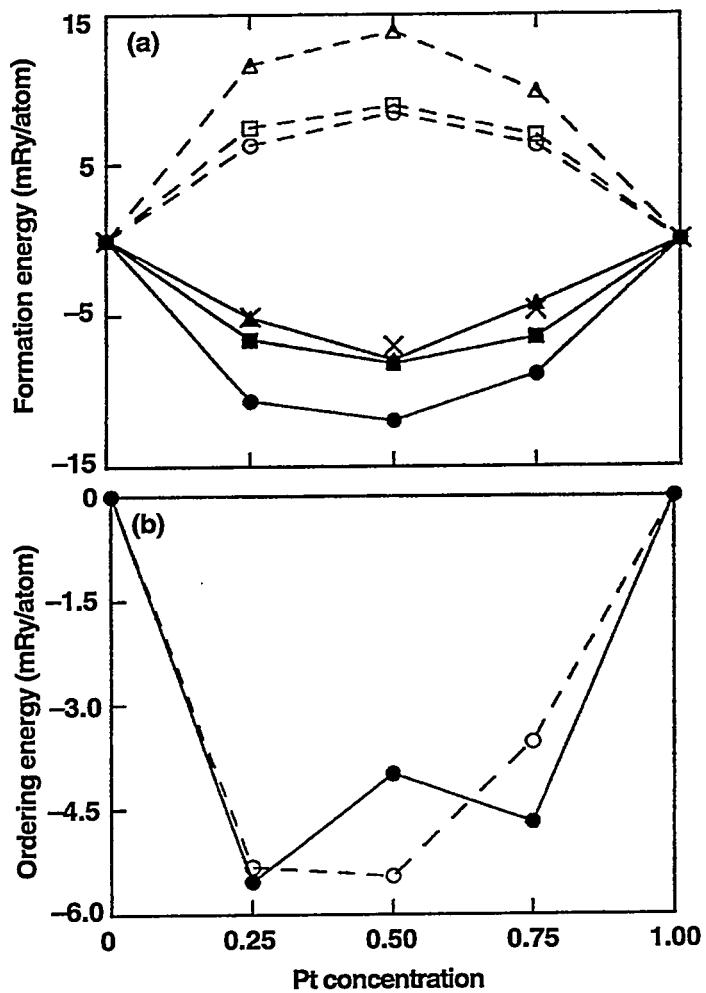
Figure 1. (a) The scalar-relativistic (filled symbols) and nonrelativistic (open symbols) formation energies of nickel–platinum alloys obtained with charge-neutral calculations. The circles, squares, and triangles represent the results of ordered calculations, ordered with combined correction calculations, and disordered calculations, respectively. The crosses show the experimental heats of formation. **(b)** The scalar-relativistic (filled circles) and nonrelativistic (open circles) ordering energies of nickel–platinum alloys obtained with charge-neutral calculations for both ordered and disordered alloys.

Plutonium on Metal Surfaces

J. van Ek, P. A. Sterne, and A. Gonis

Overview

As part of our basic research effort supporting fire-safe pit technology, we are exploring the electronic structure of a plutonium atom incorporated into a refractory metal surface. The chemistry of plutonium on various refractory metal surfaces should be reflected in the energetics of plutonium on these metals. To understand the interactions between plutonium and refractory metal surfaces, the niobium–plutonium system was modeled as a niobium(110) substrate with (1) a coherently stacked plutonium overlayer one atom thick and (2) a sublayer of plutonium one atom thick covered by a layer of niobium one atom thick.

The dimensions of the system as a whole are assumed to be given by the bulk-niobium lattice constant. The self-consistent electronic structure was calculated with the linear muffin-tin orbitals (LMTO) code using a 16-atom unit cell containing (1) a slab of nine atom layers of niobium covered with one atom layer of plutonium on each side and (2) a slab of seven atom layers of niobium covered on each side with a plutonium layer one atom thick and an outer niobium layer one atom thick. The slabs are separated by five layers of coherently stacked empty spheres. This unit of 16 layers is then repeated periodically to give a translationally invariant system, suitable for treatment with the LMTO code.

The electron count in the empty spheres decays exponentially to less than 0.15×10^{-4} electrons in the central empty sphere. Central niobium layers are close to charge neutrality ($<0.4 \times 10^{-2}$ electrons). The effects of relativity on the electronic structure are fully accounted for at any stage in the calculation.

Progress

The total energy-per-unit cell of the sublayer system is about 1.7 eV lower in energy than the overlayered compound. In view of the available experimental data, this makes sense because plutonium does embrittle niobium—so there must be a tendency for the plutonium to attack the niobium substrate. Figure 1 shows the density of states (DOS) for both systems. The inequivalent niobium atoms are numbered 1 to 5, niobium-1 being an atom in the central (bulk-like) layer. Because of a higher coordination number for the sublayer plutonium atoms, the hybridization between 5s and 4d states on niobium and 7s, 6d, and 5f states on plutonium is much more effective than in the overlayer system. Because of s–d hybridization, the 7s and 6d states on plutonium in the sublayer system shift downward in energy relative to the overlayer system, while the 5s and 4d DOS on the niobium atoms close to the plutonium sublayer are shifted upward.

When the plutonium atoms are buried under a niobium layer they gain about 0.4 electrons relative to the overlayer situation. The acquired charge mainly ends up in the 6d channel as a result of the lowering in energy of the plutonium 6d states. The intensified s–d hybridization in the sublayer system accounts for the increase of the total DOS around –2.4 eV. The plutonium 5f electron count does not change very much, while the 5f atomic DOS broadens, resulting in a higher DOS at lower energies (i.e., increase in the total DOS around –1 eV).

We did not detect a tendency toward the formation of a ferromagnetic moment in the plutonium layer for either of the two systems. A relatively small interatomic separation between the atoms in the plutonium layer causes the 5f electrons to delocalize, thereby destroying the magnetic moment of 5f electrons in atom-like states. Equivalent behavior was found in a previous study on α- and δ-plutonium.

Similar calculations will be repeated for the vanadium–plutonium system, for which it is known experimentally that vanadium is much more resistant to embrittlement by (liquid) plutonium than niobium. Further, it will be interesting to see how the total energy of an ordered surface alloy compares to the two

systems presently investigated. Such an alloy would provide an intermediate between the overlayered system and the somewhat artificial plutonium-sublayer compound.

Publications

J. van Ek, P. A. Sterne, and A. Gonis (1993), "Phase Stability of Plutonium," *Phys. Rev. B* 48, 16280.
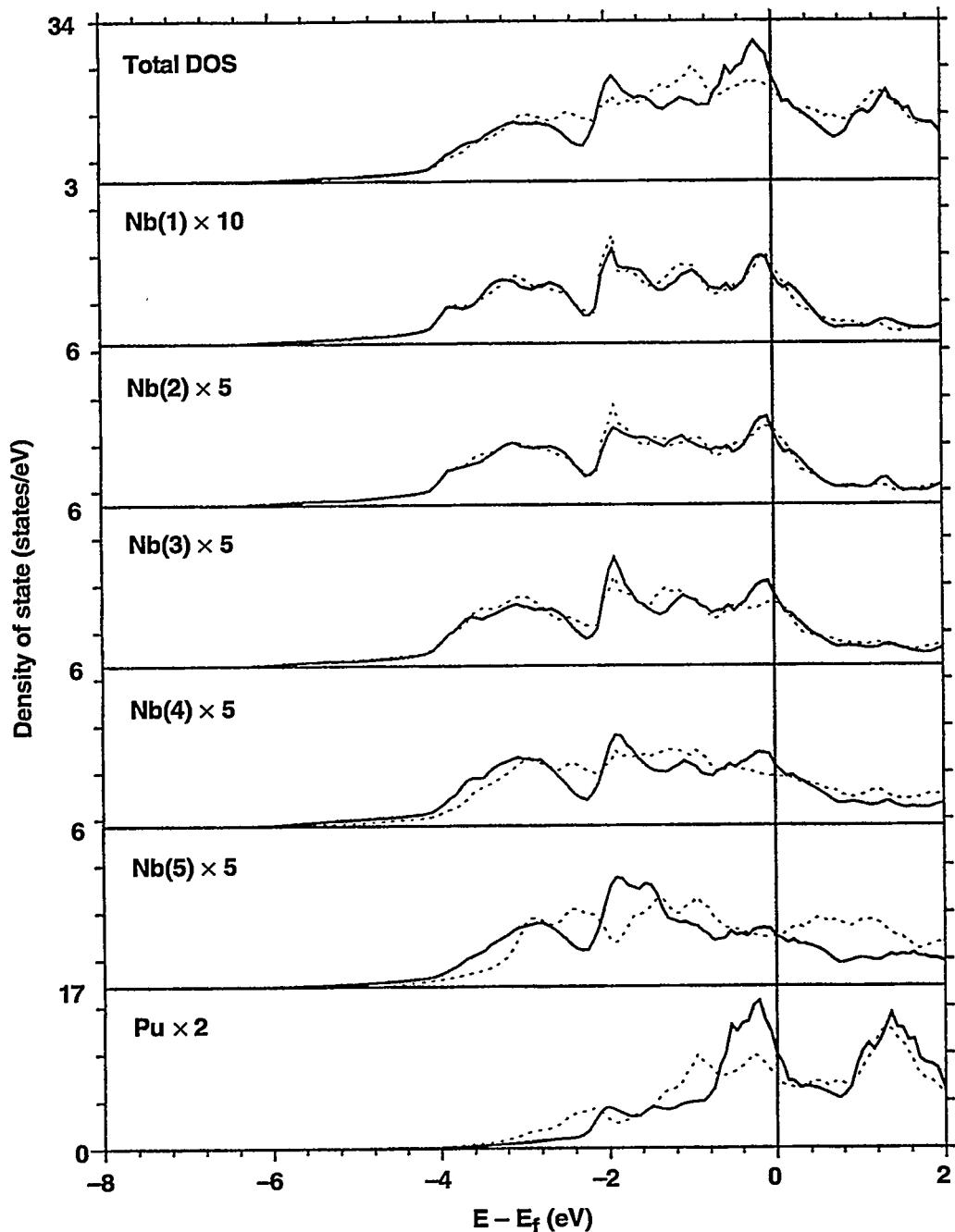

Figure 1. Total and atom decomposed DOS for a single-atom overlayer of plutonium on a niobium(110) substrate (solid line) and a plutonium sublayer covered by one layer of niobium (dashed line). Nb(1) is an atom in the central layer of the 11-layer slab.

Theory of New Thermoelectric Materials with Exceptional Figures of Merit

P. E. A. Turchi

Overview

A better understanding of the electronic properties and crystalline structure relationships is required to support and guide the experimental effort in designing and processing new advanced thermoelectric materials. This study is based on electronic structure calculations in the framework of first-principles and semi-phenomenological models. The role played by alloying, pressure, and anisotropic distortions on these relationships will be examined for transition-metal silicides M–Si (where M is iron, ruthenium, or osmium) either in the bulk form or in multilayer configurations. From experimental studies of the kinetic characteristics of metals and alloys, it is known that the conductivity and thermopower have singularities associated with so-called "electronic topological transitions" (ETT) that are relevant for this proposal. This work will predict whether or not a gap exists in the density of states of these materials and will evaluate the electrical conductivity. The development of new theoretical tools that combine, on one hand, the accurate knowledge of microscopic material parameters and, on the other hand, experimental determination of transport coefficients should provide a more accurate evaluation of the figure of merit ZT, which characterizes the efficiency of thermoelectric materials.

Work in Progress

First-principles electronic-structure studies were performed for a series of silicon-based transition-metal compounds. The calculations are based on the scalar relativistic linear muffin-tin orbital method in the atomic sphere approximation (LMTO-ASA) within the local density approximation of the density functional theory. The only input parameters are the atomic numbers of the various species and the crystalline structure. The Layer Korringa, Kohn, and Rostoker (LKKR) method, which is combined with the coherent potential approximation (CPA) to treat chemical disorder effect, is also being used to study multilayers of transition metals and silicon. To treat the more complex structures, such as the Nowotny "chimney-ladder" structures (and even the amorphous state) exhibited by thermoelectric materials and, at the same time, to examine the role played by alloying on the electronic properties of these compounds, a more versatile method based on the tight-binding (TB) approximation and the recursion method will be used. The alloying effect itself will be treated within the single-site CPA. The electronic parameters that enter this semi-phenomenological model are obtained from the so-called TB-LMTO scheme, which reduces the basis set to a tight-binding one—so that an accurate description of the electronic properties can still be achieved. The transferability of the electronic parameters that enter the TB model is now being checked to calculate the electronic structure properties of more complex structures.

From the band structure information of B2- (of CsCl type) and C1- (of CaF_2 type) based MSi and MSi$_2$ ordered compounds, respectively, where M is iron, ruthenium, or osmium it is apparent that, although these compounds have an overall metallic character, their Fermi surface is only confined around a few special k-points of the Brillouin zone. We found that application of a hydrostatic pressure does not change the overall characteristics of the band structure. One immediate question is: What is the role played by local atomic distortions or alloying (doping) in a possible metal to semiconductor transition (or ETT) in these materials? For this study, calculations are currently performed on an approximation of the complex oC48 structure, at the composition MSi$_2$, which is known to display a semiconducting character. The number of atoms in the unit cell has

been reduced from 48 for oC48 to 6 for the approximation (or 64 to 8 if empty spheres are included). However, electronic structure and transport calculations based on the LKKR-CPA approach are currently performed for multilayers of iron–silicon as a function of the stacking orientation and the repeat period to test the validity of the Hicks and D resselhaus prediction on the quantum well effect on the thermoelectric figure of merit.

Work Plan

With LMTO-ASA–, LKKR (LKKR-CPA)–, or TB (TB-CPA)–based calculations, we will study the electronic band structure, Fermi surface (if any), total and partial densities of states, and equilibrium properties of a class of materials that includes MX, MX_2, and M_2X_3, where M is a transition metal belonging to the VIA–VIIIA series (i.e., chromium, molybde-

num, tungsten, manganese, iron, ruthenium, osmium, cobalt, rhodium, or iridium) with special emphasis on iron-, ruthenium- and osmium-based materials, and X is silicon or germanium. Note that these three metal-based silicides show strong similarities in their crystalline structures and properties, at least at high silicon composition (above 50 at. % silicon).

In this study, the following issues will be addressed:
- Semiconducting vs metallic character.
- Influence of (1) crystalline structure, (2) M or X substitution, and (3) pressure on stability and electronic structure properties.
- The influence of bulk vs multilayer configuration on the above properties.

Within multiple scattering theory (LKKR-CPA), electrical conductivity will be calculated, and formalism will be developed to calculate the Seebeck coefficient.

Fabrication of a Σ5(210)/[001] Symmetric-Tilt Grain Boundary in Boron-Doped Ni₃Al for a Multipronged Experimental Approach to the Effect of Boron on Ductility

W. E. King, G. H. Campbell, and W. Wien

Introduction

We report on the fabrication of a boron-doped Ni_3Al bicrystal. The interface was a $\Sigma5(210)/[001]$ symmetric-tilt grain boundary and was selected based on its potential for atomic structure determination via high-resolution electron microscopy for relation to subsequent property measurements. Figure 1 shows the coincidence site lattice model for the $\Sigma5(210)$ tilt grain boundary in the Ni_3Al structure. This boundary is equivalent to a 180-deg twist boundary on the (210) plane.

Experimental Procedure

Ni_3Al single-crystal boules were obtained from the Materials Processing Center at Ames National Laboratory. The nominal composition is $Ni_{0.76}-Al_{0.24}$ containing 500 ppm boron by weight. After growth, the crystals were homogenized at 1200°C for seven days. The single-crystal boules were oriented to within 1 deg of [210] using Laue back-reflection x-ray diffraction patterns. The oriented boules were cut into 6-mm-thick slabs using electrodischarge machining followed by polishing to remove surface damage. The direction of the surface normal of the slab was measured using Laue back-reflection then repolished such that the surface normal was then parallel to [210]. Extensive spot splitting was observed for these crystals compared with previous work on niobium and molybdenum. This splitting indicates the presence of low-angle grain boundaries whose misorientation is several degrees. Several of these subgrains were found within a 0.7-mm x-ray beam giving an indication of the size of the subgrains. The direction of the surface normal was checked using Laue patterns and the tilt/polish procedure was repeated. Within the limitation of these subgrains, the

crystals were oriented as precisely as possible. Figure 2 shows the [210] Laue patterns. The samples were then removed from the goniometer, inverted, and mounted on a parallel polisher. The exposed surface was ground and polished such that the surface normal was parallel to [210]. The flatness of the sample was measured by observing the interference fringes between an optical flat and the sample surface. The variation in the surface profile is ±75 nm over the entire sample.

The samples were demounted and cleaned. At this point it was necessary to establish and indicate the relative orientation of the two crystals about [210] such that the [001] directions of the crystals were antiparallel. We accomplished this by attaching each crystal to a single-rotation goniometer with the surface normal of the sample parallel to the rotation axis. In this way, only the twist orientation of the crystals about their surface normals was adjustable. The goniometers were then mounted opposing one another on the x-ray track with the x-ray beam perpendicular to [210], and the Laue back-reflection method was used to set the twist orientation of each sample independently by
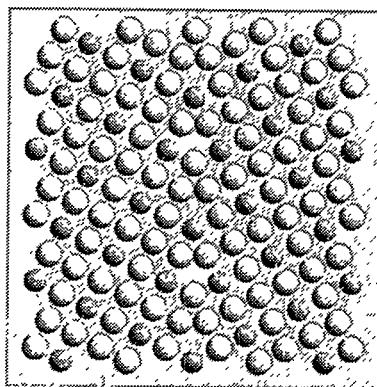

Figure 1. The coincidence site lattice model for the Σ5(210) tilt grain boundary in the Ni₃Al structure.

successively driving each crystal into the x-ray beam. One sample was set with [001] parallel to the x-ray beam and the other with [001] anti-parallel to the x-ray beam. Figure 3 shows the Laue patterns. After the desired orientation was established, the crystals were driven together and fastened with a solvent-soluble epoxy. Upon removal of the bicrystal, an optical flat was polished along the outer edge, the normal of which was perpendicular to the twist axis of the bicrystal. This optical flat was used for alignment of the samples in the ultrahigh-vacuum (UHV) diffusion-bonding machine. The epoxy was then dissolved from the crystals, and the crystals were cleaned before introduction into the UHV diffusion-bonding machine.

Ni₃Al crystals were introduced to the bonding machine and transported to the surface analysis chamber for prebonding study. Figure 4 shows the integral Auger electron spectrum (AES) from the as-introduced sample. This spectrum showed the existence of boron, carbon, oxygen, nickel, and aluminum on the as-introduced surface. The surface was sputtered for 10 min using 1 keV Xe+ ions. After sputtering, a second AES spectrum was recorded and showed peaks characteristic of nickel and aluminum.

To investigate the effect of heat treatment on the surface chemistry of the crystals, AES spectra were recorded as a function of temperature during heating and cooling from room temperature to about 500°C. These results are shown in Fig. 5 where we plot the derivative of the AES spectrum with respect to energy. On a sputter-

cleaned surface at 275°C, carbon and oxygen peaks began to grow, indicating segregation of carbon and oxygen to the surface of the crystal. Both peaks continued to grow with increasing temperature to 490°C where the carbon peak was observed to vanish. This was likely due to increased solubility for carbon in Ni₃Al at this temperature. Reduction of the temperature to 385°C showed the reoccurrence of the carbon signal.

In an attempt to locally purify the near-surface region of the crystal, the crystal was sputter-cleaned while holding the temperature to 415°C where carbon and oxygen were observed to rapidly come to the surface. The combined annealing and sputtering process was carried out for 15 min at which time sputtering was stopped and an AES spectrum was recorded (Fig. 6). The segregation of carbon to the surface was then monitored for 15 min while holding the sample at 410°C. After this time, only a small carbon peak was observed (compare the scales of Figs. 5 and 6). This indicates that the near-surface region was effectively purified of both oxygen and carbon.

After cleaning, samples were transported to the bonding chamber where the relative orientation of the crystals was set using the precision crystal orientation device coupled with a laser beam. Two alumina blanks and the Ni₃Al samples were stacked on an alumina ram, which is part of the diffusion-bonding press. The fingers of the precision crystal orientation device are rotatable, which enables setting of the twist orientation of the samples. We accomplished this
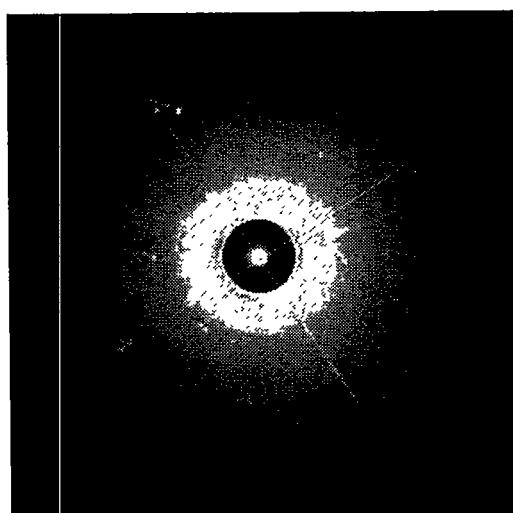
Figure 2. Laue backscatter x-ray diffraction patterns of [210] surface normals for the two single crystals. Note the extensive spot splitting.
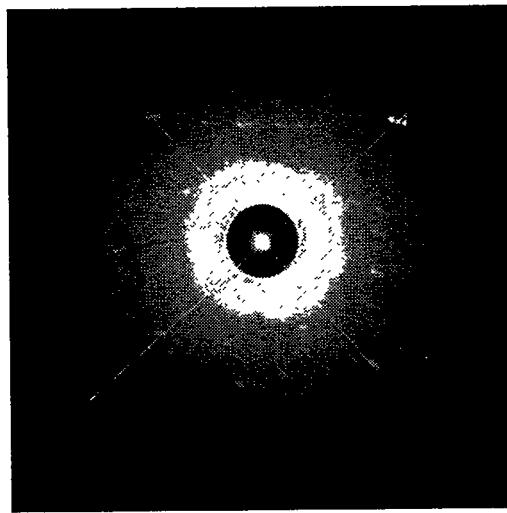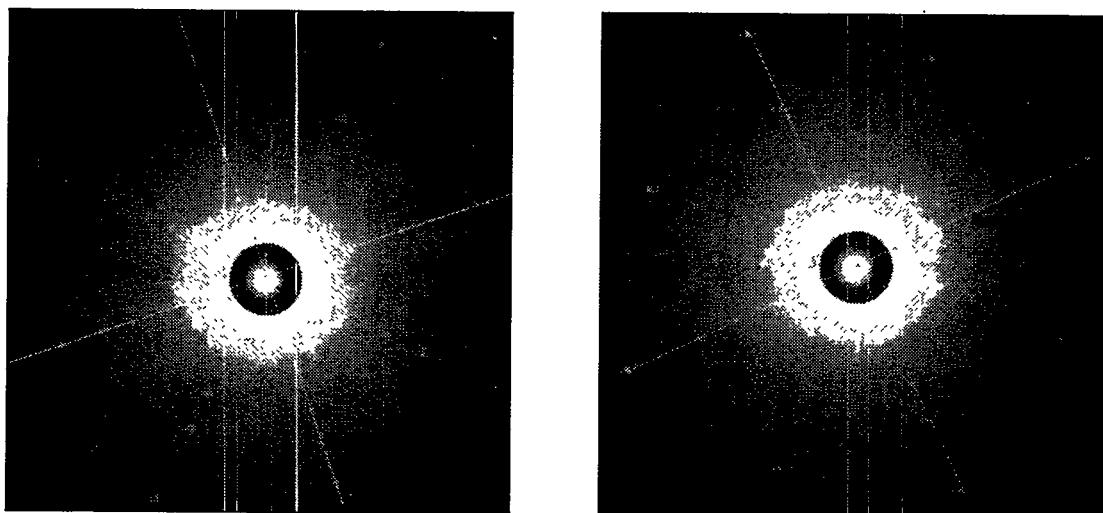
Figure 3. Laue backscatter x-ray diffraction patterns used to align the [001] tilt axis of the bicrystal.
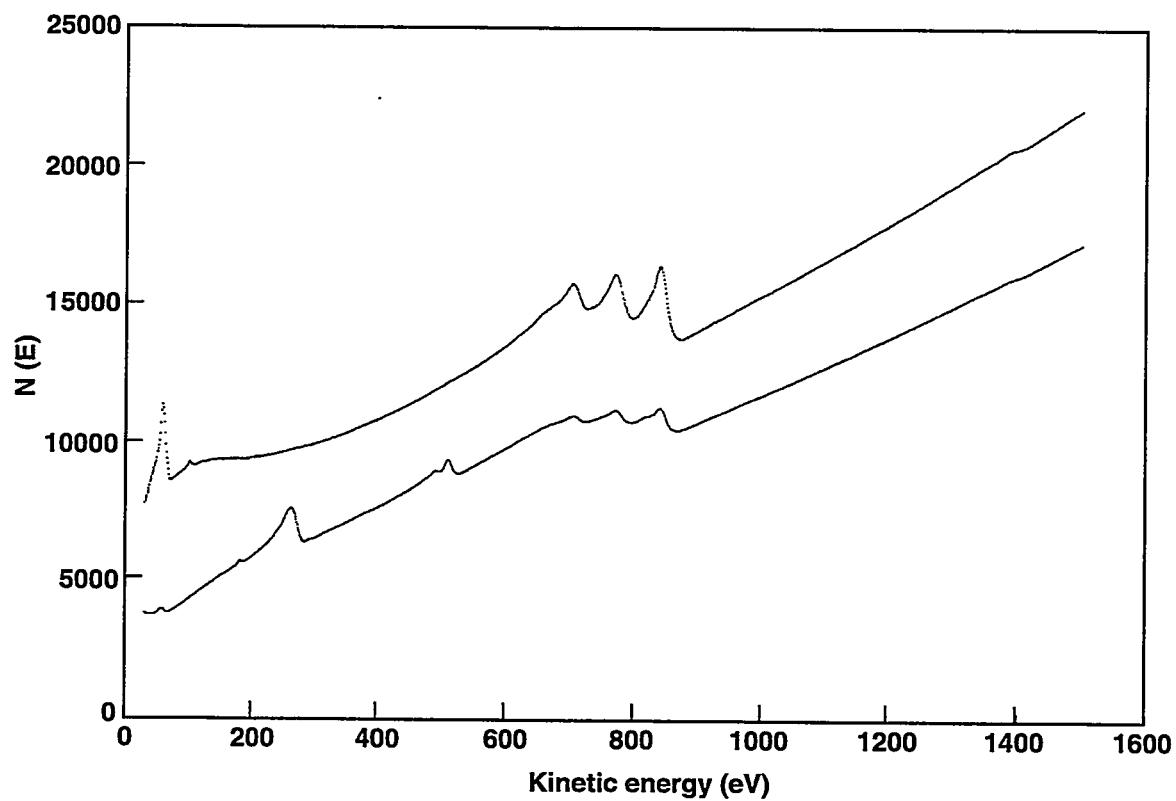
Figure 4. Auger electron spectra from as-introduced and sputter-cleaned Ni₃Al crystal.
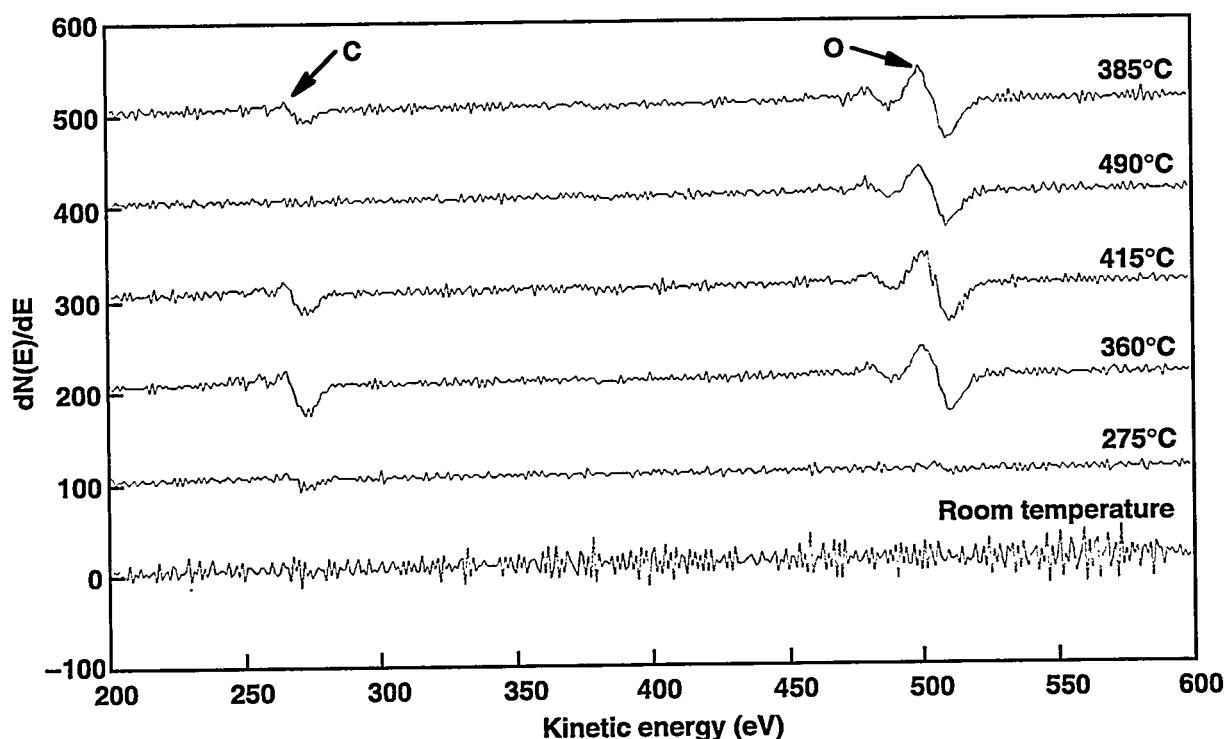
Figure 5. Differential Auger electron spectra from Ni_3Al crystal acquired as a function of annealing temperature.
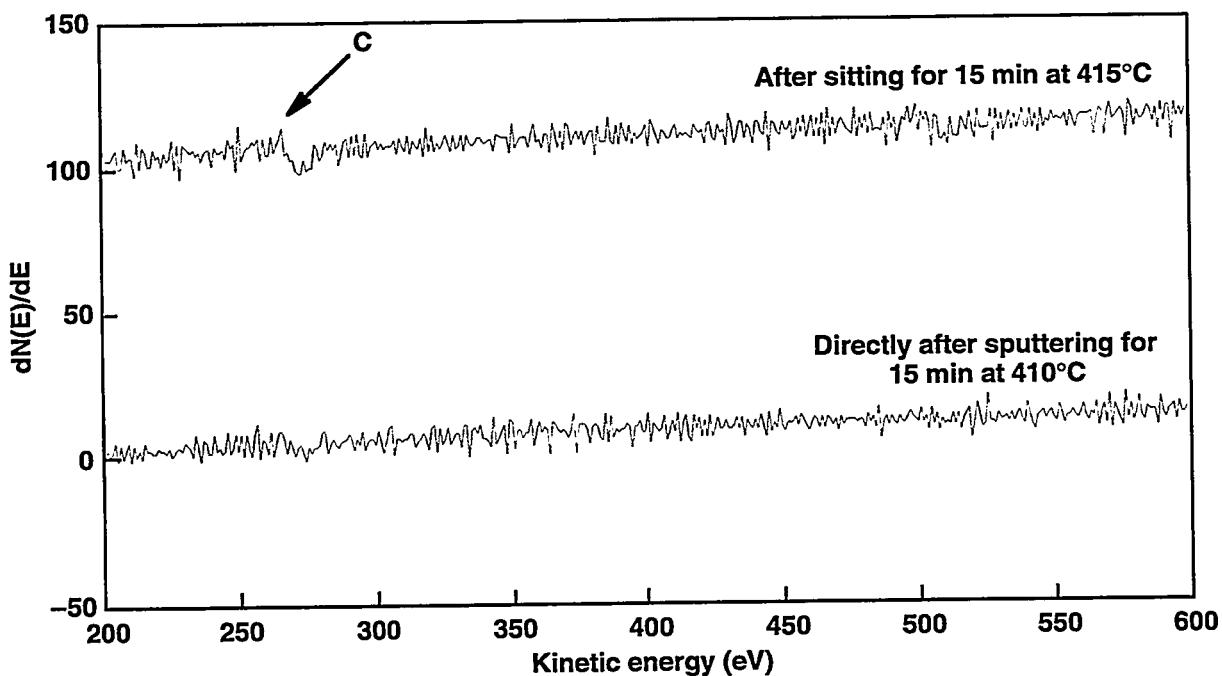
Figure 6. Differential Auger electron spectra showing the effect of locally purifying the surface by sputtering at temperature.

using laser-beam reflection from the optical flats that were polished onto the sides of the samples in the final stages of preparation. At this point, a second alumina ram was brought to rest on top of the stack and the fingers were withdrawn. Using this procedure, the crystals were oriented to 0.1 deg of the orientation that was marked by optical flats. The entire sample stack was then raised into a radio-frequency heating coil with a molybdenum susceptor. A load of 236 N was applied, and the sample was heated to the bonding temperature, 1150°C. Figure 7 shows the temperature vs time history. The vacuum in the diffusion-bonding chamber was tracked during the same time and is plotted in Fig. 8. At no time did the vacuum exceed 2×10^{-8} Torr.

Optical Observations of Bonded Samples

Figure 9 shows a view of the as-bonded sample. The sample is composed of two polycrystalline alumina blocks on either end

that interpose two Ni_3Al single crystals. The crystals remained undeformed and well-aligned after bonding, indicating that insignificant creep deformation occurred under the bonding conditions.

Future Experiments

Samples are currently being cut from the bicrystal for several experiments. Mechanical test experiments will be carried out at LLNL. High-resolution scanning transmission electron microscopy coupled with electron energy-loss spectroscopy to investigate the interface density of states will be carried out at Cornell University. Atom probe field ion microscopy will be carried out at Northwestern University to assess the boron content of the boundary. The high-resolution electron microscopy will be carried out at Sandia National Laboratory, California, and LLNL to study the interface atomic structure.
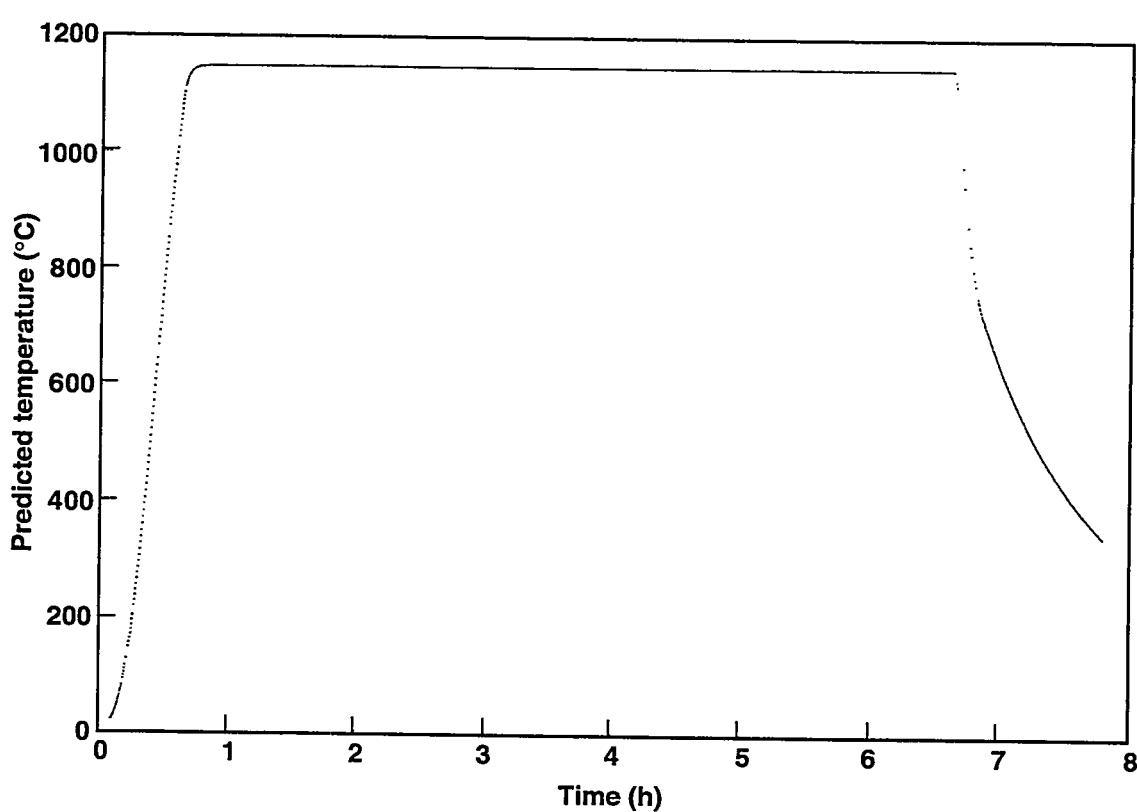
Figure 7. Sample temperature history predicted from optical pyrometry measurements of RF furnance susceptor temperature.
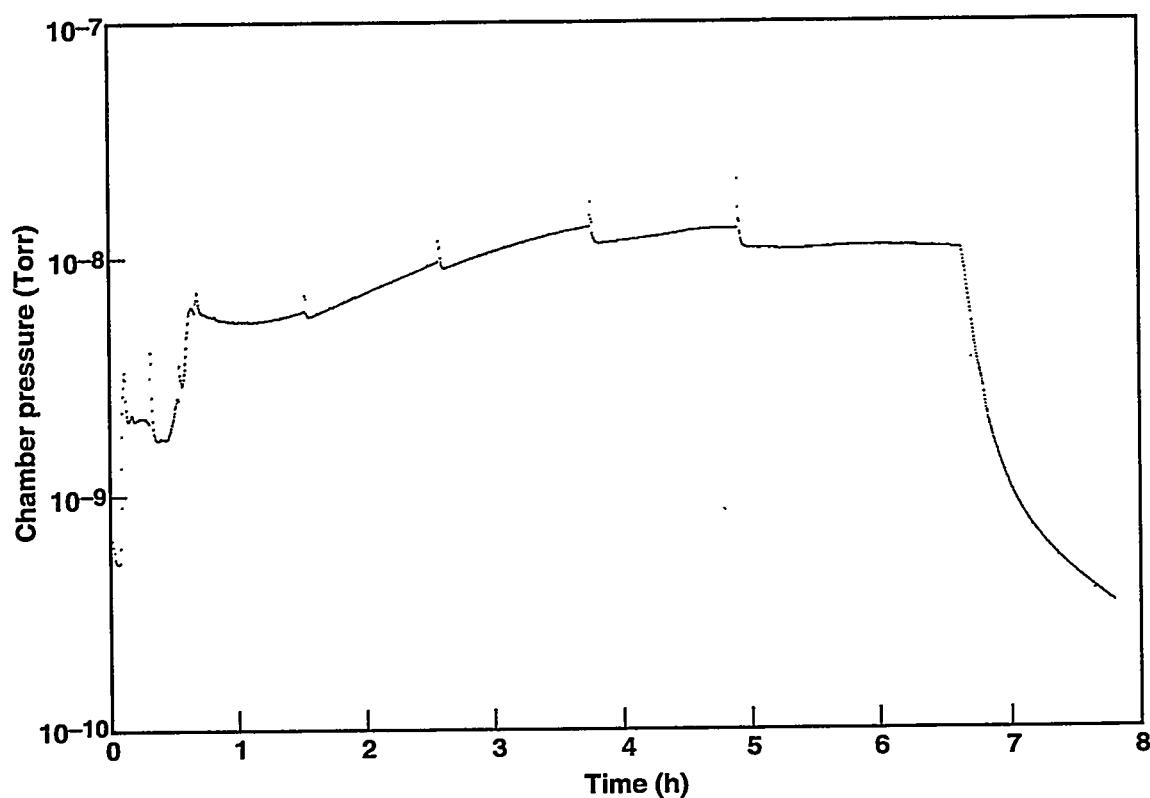
Figure 8. Vacuum in diffusion-bonding chamber as a function of time. Spikes in vacuum correspond to firing of titanium sublimation pump.
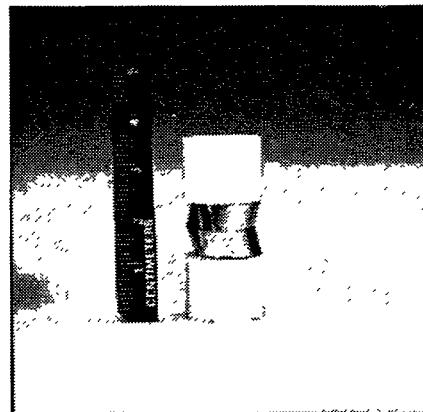
Figure 9. Photograph of as-fabricated bicrystal. Optical flats used for orientation are visible at left. A 180-deg twist on [210] plane is clearly visible from the geometry.

.

Laboratory Directed Research and Development

Director's Initiatives

Molecular-Level Studies of Energetic Materials

P. C. Souers

Explosive Alloys

The goal of this project is to determine how the sensitivity of energetic materials is controlled by their intramolecular and intermolecular structures. Whereas the role of intramolecular effects in stabilizing the structure against shock and impact initiation has been well researched, the role of intermolecular bonding (e.g., hydrogen bonds) has not. The three thrust areas for FY94 are

- General intermolecular structural effects—does the molecular packing in the crystal ("herringbone" vs "bedspring") itself relate to sensitivity?
- Hydrogen bonding and the structural effect of impurities on sensitivity.
- Structure disorder from thermal transitions.

The goal of the first thrust area is to produce a predictive method for the design of new energetic materials. Because the hypothesis is that intermolecular bonding is the key to understanding the sensitivity puzzle, we are concentrating on how intermolecular effects can be used in addition to the standard intramolecular design criteria.

One focus is on the relationship between molecular crystal packing and sensitivity. To find correlations between molecular packing and sensitivity, crystal structure and sensitivity data for about 500 compounds ranging from non-high explosives to powerful explosives have been collected. We are studying the correlation of oxygen balance (explosive power), heat of formation (intramolecular stability), and density (molecular packing efficiency). A three-dimensional plot of data for over 300 compounds shows an island of dense, energetic materials that will be targeted for structural and sensitivity analysis. To correct for heat of formation anomalies due to high molecular nitrogen content or large molecular size, heats of formation will be replaced by heats of reaction calculated by the thermochemical code Cheetah.

The goal of the second thrust area is to determine how intermolecular bonding can be changed to design less-sensitive materials, preferably from relatively sensitive starting materials. We are investigating whether the inclusion of impurities in energetic materials affects sensitivity through structural change or merely morphology modification. The impact sensitivity of 2,4-dinitroimidazole (2,4-DNI) has been shown to decrease dramatically with only a few percent of 4-nitromidazole (4-NI) impurity, a by-product of synthesis. One hypothesis suggests that complexation of the 4-NI impurity with 2,4-DNI changes the directionality of hydrogen bonding in the solid. This modified structure may be more insensitive because of the impact of directionality on slip planes rather than a quantitative increase in intermolecular bonding.

Batches of 2,4-DNI were contaminated with known amounts (determined by nuclear magnetic resonance analysis) of 4-NI to study quantitatively how the impurity level, molecular structure, and sensitivity interrelate. Scanning electron micrographs revealed a relatively poor morphology (numerous defects) in the purest material. However, the quality improved with increasing 4-NI. Although a reversible endothermic conversion seen in differential calorimeter records did relate to 4-NI impurity level (not present in pure 2,4-DNI), the two ingredients were seen to react individually. These data so far suggest that 4-NI does not form a complex with 2,4-DNI, but may at least act as a morphology modifier.

To study how intermolecular bonding affects sensitivity, we are producing more hydrogen-bonded high-explosive complexes with the more heavily nitrated biimidazole analog of dinitrobistriazole (DNBT), one component in the known insensitive high-explosive complex DNBT–2ANTA (ANTA is 3-amino-5-nitro-1,2,4-triazole). The complex (Fig. 1) forms a strongly hydrogen-bonded network much like that of TATB.

The Los Alamos National Laboratory's compound 4,4′,5,5′-tetranitro-2,2′-biimidazole (TNBI) (Fig. 2) is being studied now and is more sensitive than DNBT. Compounds mixed to date with TNBI include 3-amino-1,2,4-triazole (3-AT) and 5,5′-diamino-3,3′-bi(1,2,4-triazole) (DABT), both forming as yet unidentified very insoluble colored crystals whose infrared spectra are distinct from each starting material. Compounds such as 4,5-dinitroimidazole, which might be expected to complex based on molecular symmetry, and ANTA, a good complexing agent, did not complex. Work is in progress to complex TNBI with other compounds with more energy in the rings (e.g., oxadiazoles) to compensate for the replacement of energetic NO_2 groups with hydrogen-bonding amino groups that exist in 3-AT and DABT.

In our third thrust area, we are performing fast-heating thermal analysis of TATB samples to study whether high-temperature phase transition(s) in TATB could yield a more disordered, poorly hydrogen-bonded structure that would account for the increased sensitivity of hot TATB formulations. Fast ramp rate (50–125°C/min) DSC data shows multiple unidentified endothermic responses in ultrafine (submicron), normal, crystallized, dry-aminated, micronized, and crash-precipitated TATB. The appearance of endotherm(s) in samples prepared by vastly different techniques suggests that impurities are not the source, but morphology and surface energy may play an important kinetic role. Because fast-ramp (50°C/min) differential thermal analysis/thermal gravimetric analysis measurements suggest that weight loss is minimal

DNTB · H₂O
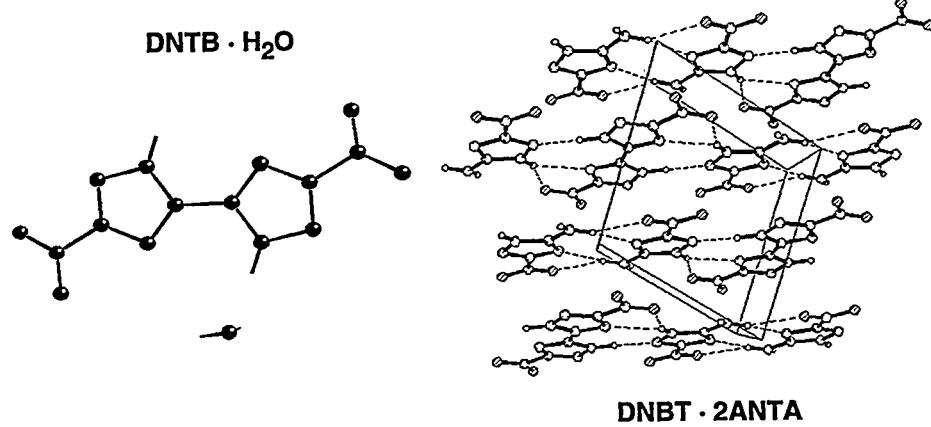
DNBT · 2ANTA

Figure 1. The insensitive high-explosive complex DNBT–2ANTA.

TNBI · H₂O
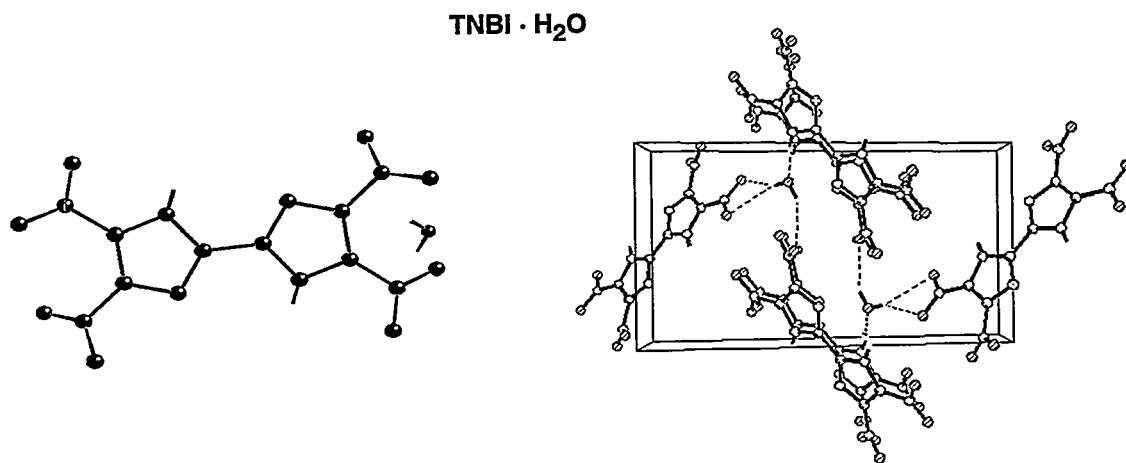
Figure 2. The Los Alamos compound TNBI.

for the highest temperature endothermic response just prior to the exotherm, sublimation is probably not the responsible behavior. Work is proceeding to determine whether the transition is due to melting or a solid–solid conversion, either of which would be important in understanding thermal sensitization.

Gateway Modes

Earlier results indicate that phonon-to-vibron energy transfer rates are important in determining explosive sensitivity. Sensitive explosives efficiently transfer energy from lattice vibrational modes (phonons) to internal molecular vibrational modes (vibrons), while insensitive explosives have much slower transfer rates. This observation was originally built on a theoretical evaluation of seven widely varying explosives. We need to ascertain whether this trend holds over a wide variety of organic explosives or not.

To determine this, we have worked in collaboration with S. Trevino of the National Institute of Standards and Technology to evaluate the energy transfer rates for HMX, PETN, TATB and five other insensitive compounds. The phonon density of states is the crucial experimental information needed to calculate energy transfer rates. The best indicator of the density of states is given by incoherent neutron scattering experiments. Trevino has performed these experiments for the eight sample compounds. We then performed the theoretical calculations based on his results (Fig. 3). The results confirm our earlier observation that in the range of 400 to 600 cm^{-1} the known sensitivities, as measured by drophammer and the energy transfer rates, show a high degree of correlation.

To advance our predictive structural capability, we are presently undertaking molecular dynamics simulations of TATB and HMX. The ab initio electronic structure procedure followed last year for HMX did not yield a stable crystal structure. Therefore, a more refined electronic structure calculation is underway, using a larger basis set, and with partial charges on atoms determined by a rigorous fitting of the electrostatic potential. The present potential is producing a stable crystal structure in its first tests.

Detonation Physics

Work on detonation physics has recently been incorporated in this project. Previous work, funded by Physics, analyzed the light from four two-stage gas gun shots on the liquid explosive, nitromethane, with the flyer velocities set to span the detonation point. The blackbody spectrum from three points above the detonation point was measured and the plateau caused by the piston-action of the heavy sabot was observed. From the plateau, an in situ detonation temperature of 3900 K was obtained.

Examples of the most recent data on nitromethane are shown in Fig. 4. The step labeled "detonation" is normally expected. It then decays to the constant-pressure plateau created by the piston driving the explosive in front of it, which yields the detonation temperature. The reshock is caused by the reflection of the shock wave from the sapphire observation window and interferes with the temperature measurement. Most interesting is the early bulge called "superdetonation," which was not seen in the preliminary run. It may represent the extra energy imparted when the detonation wave reaches the original shock wave in the liquid.
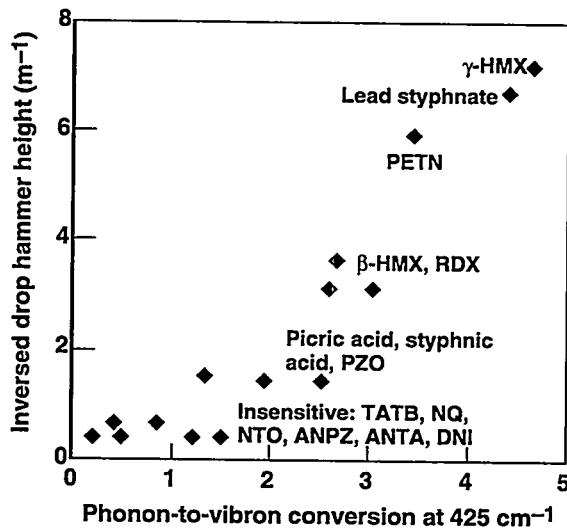

Figure 3. Correlation between calculated energy transfer rates in explosives and the inverse of the measured drophammer height. The correlation is excellent, with the most insensitive explosives at the bottom and the most sensitive at the top.
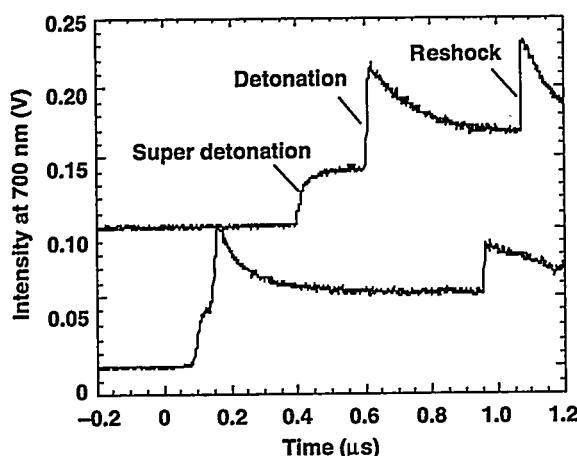
Figure 4. Light emission form nitromethane detonated with a gas-gun sabot at the velocities shown.

Molecular Hydrodynamics

There remain many unresolved questions regarding the initiation of detonation in high-explosive materials. These materials are primarily molecular solids, and in addition to strong intramolecular forces, the molecules interact with one another through weak van der Waals, long-ranged electrostatic, and hydrogen-bonded forces. Hydrogen-bonding is thought to drive the relative stability of TATB.

In our molecular hydrodynamics approach, we use an atomistic description for the forces between atoms within the molecule (intramolecular) and between atoms on neighboring molecules (intermolecular). The forces used in modeling HMX were developed from electronic structure calculations. We began by examining the stability of the experimental crystal structure for HMX at zero pressure and room temperature. The tetragonal structure was found to be stable with respect to small distortions of the molecular dynamics simulation cell, though the volume of the cell expanded to a few percent larger than the experimental volume. The HMX molecules remained in the chair conformation.

To study the nonequilibrium response of individual molecules in HMX and the transport of energy from translational motion into internal vibrational motion, we have simulated the propagation of shock waves with strengths up to 200 GPa. The stronger shocks are prob-

ably unrealistic in that the molecules in our current model are not allowed to dissociate. Potential parameters are being developed for carbon, hydrogen, nitrogen, and oxygen within the bond-order approximation, and we expect to begin studying reaction dynamics this year. The molecules at the shock front are in a highly nonequilibrium state, thus, thermodynamic concepts such as temperature are not well-defined. However, mechanical concepts such as kinetic energy are well-defined, and we can consider a kinetic temperature based on the equipartition of energy. We have proposed that for a molecule like HMX with many internal degrees of freedom, the kinetic temperature associated with center of mass motion at the shock front should significantly overshoot the final equilibrium temperature far behind the shock front. Figure 5 shows our calculated results for an 80-GPa shock in HMX.

The large spike is the kinetic temperature for the center of mass motion (both translation and rotation). This spike identifies the position of the shock front. The lower curve is the remaining kinetic energy that is due to internal vibrations. Equilibrium between center of mass motion and internal vibrational motion occurs several nanometers behind the shock front. This does not mean that equilibrium between all internal vibrations has occurred on this fast time scale. The observed overshoot is about 11,000 K. This is about half the value expected from Dremin's theory. The discrepancy is probably due to internal vibrational motions being directly excited at the shock front. Knowledge of the exact nature of these internal
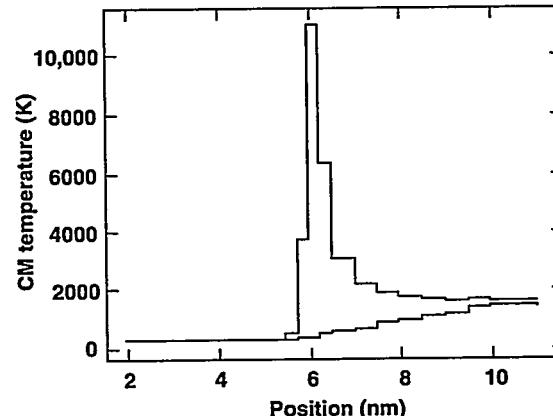
Figure 5. Kinetic temperature calculated for an 80-GPa shock in HMX.

vibrations may lead to new insights into the doorways for energy transport in energetic materials. A detailed analysis is currently in progress.

For determining sensitivity, the nature and evolution of the material microstructure is probably more significant than the response of individual molecules at a shock front. For example, nothing is known about the conformation of molecules at the core of a dislocation in energetic molecular crystals, nor the work required to move the dislocation (Peierls stress) and the frictional heat generated. This frictional heat and other forms of localized energy (hot spots) play a central role in most theories of sensitivity. To begin testing these ideas, we have introduced small voids into our simulation by removing small clusters of molecules and have repeated the shock wave simulations. Figure 6 shows the resulting peak kinetic temperature at the shock front at the center of the small void for a 50-GPa shock. This energy rises quickly with void size but dissipates within a few nanometers behind the shock. This is consistent with practical experience, which indicates that only really large voids
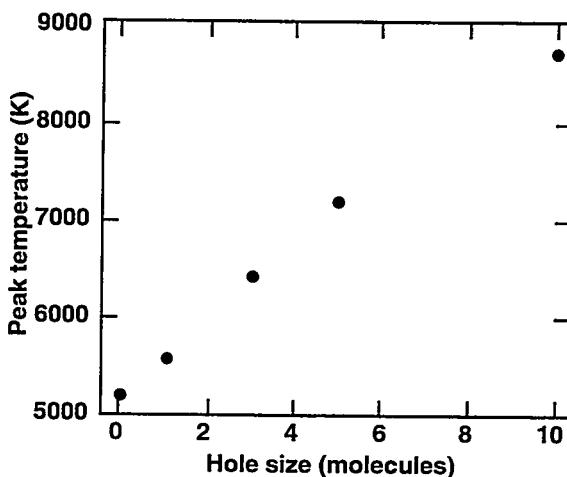
Figure 6. Variation of calculated temperature with void size for a 50-GPa shock.

(>0.1 μm) are significant. The molecules near the surface of the void move far away from their original lattice positions, and the local structure appears disordered or possibly to have melted though the time scale is too short to measure diffusive motion.

Aerogel-Based Electronic Devices

R. W. Pekala, S. T. Mayer, J. L. Kaschmitter, and T. D. Tran

Overview

The principal objective of this project is to develop a fundamental understanding of the chemistry, engineering, and physics issues involved with tailoring the structure and properties of carbon aerogels for applications in supercapacitors (i.e., electric double-layer capacitors). This project builds upon LLNL expertise in organic aerogels to develop energy-storage devices with high energy (~4 Whr/kg) and power densities (~7 kW/kg) accompanied by low internal resistance (<100 mohms). Such devices will impact all types of power conversion, including power converters in electric vehicles and industrial motor controllers.

## Technical Progress

A large fraction of our technical activity in the past year has focused on the scientific issues associated with producing a prototype aerocapacitor. As part of this, we demonstrated the production of thin film, porous carbon electrodes (<125 μm) with areas greater than 50 cm^2, delineated the effects of pyrolysis temperature on capacitance, and measured the frequency dependence of supercapacitor performance using impedance spectroscopy. In addition, we demonstrated a 5-V bipolar stack supercapacitor with large-diameter, thin-film carbon electrodes and improved contacts; examined its cycle lifetime; and identified packaging materials required for supercapacitors using acidic, basic, or organic electrolytes. As an additional component of prototype development, we developed a systems model for supercapacitors that predicts energy and power densities as a function of packaging, electrode, electrolyte, and separator materials.

In addition to the issues described above, we also explored alternative means of cost-effectively producing the aerogel electrodes. Porous carbons, such as carbon black powders and activated carbon fiber clothes, have been investigated as electrode materials in double-layer capacitors over the past 25 years. Carbon aerogels represent a significant breakthrough as an electrode material because of their controllable pore size, large volumetric surface area (~500 m^2/cm^3), high electrical conductivity, and low inorganic ash content. Previously, the capacitance of thin monolithic aerogels were studied, giving capacitance values as high as 35 F/cm^3. Because monolithic aerogels must be supercritically dried to preserve their high surface area and ultrafine pore size, we decided to explore alternative methods for producing carbon aerogel electrodes in a more cost-effective manner.

We prepared a carbon aerogel composite in which our starting resorcinol-formaldehyde solution was infiltrated into a thin sheet of carbon paper (125 μm thick and greater than 90% porosity). After curing the resorcinol–formaldehyde mixture, the pore fluid was exchanged with acetone and the composite was air-dried. Essentially, a resorcinol–formaldehyde aerogel was deposited on the carbon fibers in the paper. This material was then pyrolyzed at 1050°C in an inert atmosphere to form the thin-film carbon aerogel composite. Capacitance measurements give a value of 15 to 18 F/cm^3 for the composite material. Although this value is substantially lower than the highest values achieved for monolithic carbon aerogels, it is still 3 to 4 times higher than other commercially available electrode materials. Furthermore, this process allows for the production of carbon aerogel composites with large cross-sectional areas and eliminates the need for supercritical drying.

During cycling of supercapacitors, it is apparent that the surface groups attached to the carbon aerogel must be characterized and controlled if individual cells are to be operated near the breakdown voltage of water (i.e., 1.2 V). Preliminary data show that these surface groups can be electrochemically oxidized to form gases. As a result of the large volumetric

surface areas in carbon aerogels, these gases can cause ballooning and eventual failure of a sealed device. In an alternative procedure, individual cells can be derated to a lower voltage (e.g., 0.8 V), but this procedure leads lower energy densities because $E = 0.5\, CV^2$.

Publications

J. Wang, L. Angnes, H. Tobias, R. A. Roesner, K. C. Hong, R. S. Glass, F. M. Kong, and R. W. Pekala, "Carbon Aerogel Composite Electrodes," *Anal. Chem.* **65**, 2300 (1993).

R. W. Pekala and D. W. Schaefer, "Structure of Organic Aerogels: Morphology and Scaling," *Macromolecules* **26**(20), 5487 (1993).

F. M. Kong, J. D. LeMay, S. S. Hulsey, C. T. Alviso, and R. W. Pekala, "Gas Permeability of Carbon Aerogels," *J. Mater. Res.* **8**(12), 3100 (1993).

M. S. Gebert and R. W. Pekala, "Fluorescence and Light Scattering Studies of Organic Sol-Gel Reactions," *Chem. Mater.* **6**(2), 220 (1994).

S. T. Mayer, J. L. Kaschmitter, and R. W. Pekala, "Effects of Aqueous Solution Compositions on Aerocapacitor Energy Density", in *ECS Symp. Proc., New Sealed Rechargeable Batteries and Supercapacitors*, B. M. Barnett, E. Dowgiallo, G. Halpert, Y. Matsuda, and Z. I. Takehera, Eds. (ECS, 1993) vol. 93, no. 23, p. 38.

G. A. M. Reynolds, Z. H. Wang, M. S. Dresselhaus, A. W. P. Fung, and R. W. Pekala, "Photoconductivity: A Probe of Defect States in Carbon Aerogels," *Phys. Rev. B* **49**(21), 15027 (1994).

A. W. P. Fung, Z. H. Wang, M. S. Dresselhaus, G. Dresselhaus, R. W. Pekala, and M. Endo, "Coulom-Gap Magnetotransport in Granular and Porous Carbon Structures," *Phys. Rev. B* **49**(24), 17 325 (1994).

R. W. Pekala, S. T. Mayer, J. L. Kaschmitter, and F. M. Kong, "Carbon Aerogels: An Update on Structure, Properties, and Applications," in *Proc. Int. Symp. Advances in Sol-Gel Processing and Applications* (Chicago, IL, in press).

R. W. Pekala, S. T. Mayer, J. F. Poco, and J. L. Kaschmitter, "Structure and Performance of Carbon Aerogel Electrodes," in *Proc. MRS Symp. Novel Forms of Carbon II*, C. L. Renschler, D. M. Cox, J. J. Pouch, and Y. Achiba, Eds. (Materials Research Society, Pittsburgh, PA, 1994), vol. 349.

Presentations

R. W. Pekala, "Structure–Property Relationships in Carbon Aerogels," Third Pacific Polymer Conference, Gold Coast, Australia, December 13–17, 1993.

R. W. Pekala, "Structure and Performance of Carbon Aerogel Electrodes," Symposium on Novel Forms of Carbon II, Materials Research Society, San Francisco, CA, April 4–8, 1994.

"New Organic Aerogels Based upon a Phenolic–Furfural Reaction," 4th International Symposium on Aerogels, Berkeley, CA, September 19–21, 1994.

"Double Layer Capacitors Based on Carbon Aerogel Electrodes," 4th International Symposium on Aerogels, Berkeley, CA, September 19–21, 1994.

Laboratory Directed Research and Development

Individual Projects

Solid-State Amorphization at a Crystalline Interface

A. F. Jankowski

Overview

The transformation from one crystalline phase to another in the solid state is generally driven by system ordering, hence energy minimization. Solid-state amorphization (SSA), the crystalline-to-amorphous phase transformation, is unusual because the amorphous state is conventionally more disordered than its crystalline counterparts. Our objective is to conceptually understand and experimentally regulate the nucleation of an amorphous phase from a completely crystalline structure. The key to this objective is to control the onset of disordering as the energetically favorable reaction.

Logic dictates that nucleation of a disordered phase can occur at those locations in a crystalline system that are most disordered, e.g., internal interfaces. We will attempt to regulate the driving force behind the SSA nucleation mechanism through a systematic variation of the interface spacing. Lattice strains produced at the interfaces should alter the onset of SSA as a consequence of interfacial elastic energy minimization, i.e., an amorphous interface is energetically more favorable than a strained, highly disordered, crystalline interface.

Technical Activities and Results

The nickel–titanium system is ideal for studying SSA because there is a large atomic size difference between the elements (which favors interfacial strain and preferential interdiffusion) and a deep eutectic is found in the binary alloy phase diagram (facilitating interdiffusion). We prepared more than 50 multilayer thin films of varying layer-pair spacings and nickel:titanium thickness using planar magnetron sputter deposition. We characterized the onset of SSA using differential thermal analysis (DTA) and developed a numerical fitting procedure for the DTA curves of "ΔT vs T" to analytically identify the SSA transformation temperature, which is dependent on the layer-pair spacing. In addition, the transformation temperature appears to depend on the nickel:titanium thickness for any given layer-pair spacing.

We completed structural characterization using both high-resolution microscopy of cross-sectioned multilayers, to identify the as-deposited growth morphology and atomic crystalline arrangements, and x-ray diffraction, to assess the layer pair spacings, composition profile, and interfacial disorder via lattice distortions. The structural characterization shows stabilization of a face-centered-cubic (fcc) phase of titanium as it grows epitaxially upon nickel and a square-wave composition profile consisting of strained layers of nickel (in tension) and titanium (in compression). The magnitude of strain increases with decreasing layer-pair spacing. A thermodynamic formalism of the system energetics of disordering at a crystalline interface that includes transformation to an amorphous state is in progress

Publications

Jankowski, A. F., and M. A. Wall (1994), "Formation of Face-Centered-Cubic Titanium on a Ni Single Crystal and in Ni/Ti Multilayers," *J. Mater. Res.* **9**, 31.

Jankowski, A. F., J. P. Hayes, and P. B. Ramsey (1994), "Interface Controlled Amorphization of Ni/Ti Multilayers," in *Defect-Interface Interactions, Materials Research Society Symp. Proc.*, E. P. Evam, A. H. King, M. J. Mills, T. D. Sands, and V. Vitek, Eds., vol. 319, pp. 381–386.

Chaudhuri, J., S. M. Alyan, and A. F. Jankowski (1993), "X-Ray Analysis of Ni/Ti Multilayers," in *Thin Films—Stress and Mechanical Properties IV, Materials Research Society Symp. Proc.*, P. H. Townsend, J. Sanchez, C. Y. Li, and T. P. Weihs, Eds., vol. 308, pp. 707–712.

Chaudhuri, J., S. M. Alyan, and A. F. Jankowski (1994), "Analysis of Ni/Ti Multilayers by X-Ray Diffraction," *Thin Solid Films* **239**, 79.

Nanoscale Lithography Using Scanned Probe Microscopy

M. Balooch and W. J. Siekhaus

During the first half of the year, the newly purchased scanning tunneling microscope/ atomic force microscope (STM/AFM) was housed in an ultrahigh-vacuum system. This allowed us to study insulators and conductors with near-atomic resolution.

The AFM operates in the conventional and the noncontact mode.[1] It uses a piezoresistive cantilever that consists of a single silicon structure with a diffused conductive channel and an integrated ultrasharp asymptotic silicon tip. Deflection of the cantilever alters the resistance of the conductive channel (the piezoresistive effect). Figure 1 shows a diagram of the piezoresistive detection scheme for AFM.

We found that the resolution of the piezoresistive detection scheme is comparable to conventional optical lever AFM detection schemes and is more attractive because of its simplicity and reliability. The absence of external deflection sensing elements simplifies the design, and the low voltage dc response allows simple circuitry.

The unique feature of the instrument is its noncontact AFM capability using piezoresistive cantilevers based on frequency modulation (FM) detection, which was pioneered by Albrecht et al.[2] In FM detection, the cantilever is driven at a fixed amplitude of vibration, and changes in its vibration frequency are detected as the tip feels the surface. The FM detector measures much weaker force gradients than can be sensed using a conventional amplitude modulation detector over a given bandwidth. The instrument has been thoroughly tested.

In addition, we have been modifying our standard AFM instrument to extend its capability for measuring tribological properties of patterned silicon carbide grown on silicon using a C_{60} precursor. The properties of interest include the hardness of the film as a function of different growth conditions, the friction coefficient of the patterned film, and the elastic modulus of the film.

References

1. F. J. Giessibl and B. M. Trafas, *Rev. Sci. Instrum.* **33**, 3726 (in press).
2. T. R. Albrecht, P. Gruetter, D. Horne, and D. Rugar, *J. Appl. Phys.* **69**, 668 (1991).

Presentations

Balooch, M., "Ordered Molecular and Nanoscale Electronics," Engineering Foundation Conference, Keauhou-Kona, HI, June 5–10, 1994.

Balooch, M., "Nanoscale Lithography by Scanned Probe Microscopy," University of California, San Diego, CA, May 10, 1994.
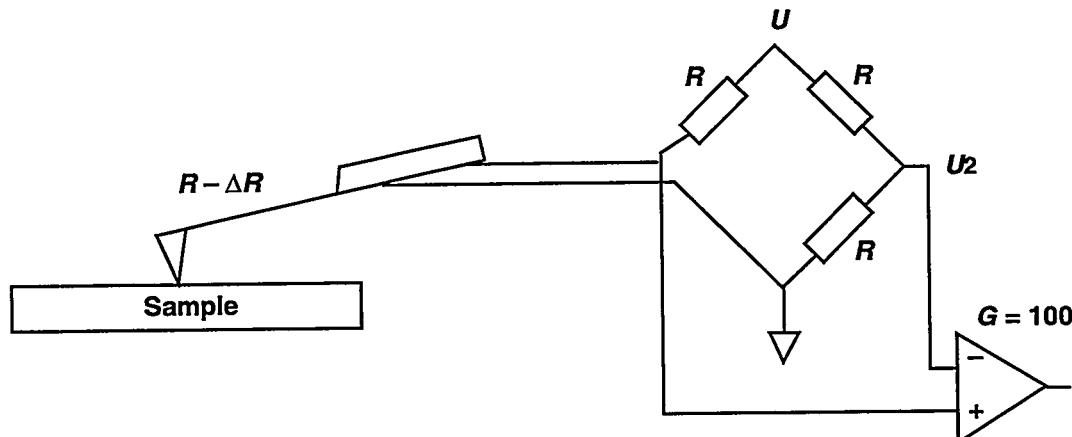

Figure 1. Diagram of the piezolever detection scheme for vacuum AFM.

Osteoporosis Research

J. H. Kinney

Introduction

Intermittent parathyroid hormone (PTH 1-34) therapy has been shown to increase bone mass and improve biomechanical strength in osteopenic animal models.[1,2] Also, intermittent PTH 1-34 therapy both alone and in combination with estrogen therapy has been reported to preserve trabecular bone connectivity.[3] Trabecular bone connectivity reports generally are derived from estimates of two-dimensional histologic data. The purpose of our study was to determine if intermittent PTH (1-34) therapy increased trabecular bone mass and connectivity in a rat model of established osteopenia using three-dimensional in vivo morphometry by x-ray tomographic microscopy (XTM).

Methods

Six-month-old, retired, Sprague–Dawley breeder rats were randomized into six groups. Six rats underwent sham operations, and all others were ovariectomized (ovx). At eight weeks post-ovx, all sham rats and one group of ovx rats were sacrificed. The remaining rats were injected for four weeks with 5 doses/ week of PTH 1-34 at 4 (low), 40 (medium), and 400 (high) μg/kg/day. At sacrifice, the right and left proximal tibias were harvested for histomorphometry and XTM scans, respectively.

For each XTM scan, the left tibia was mounted on a rotating stage and scanned with 25-keV monochromatic synchrotron radiation from the growth plate distally. A region of trabecular bone in the secondary spongiosa from 0.9 to 1.9 mm below the growth plate was extracted from each image. The data from these scans were reconstructed into 17.6-mm isotropic volume elements (voxels) using the Fourier filtered back-projection method. Connectivity density, b_1, was determined from a three-dimensional analysis of the topology of the trabecular network according to the relation-

ship $b_1 = b_0 - x$, where b_0 is the number of nonconnected trabeculae and x is the Euler–Poincaré characteristic. Connectivity per unit of bone tissue was analyzed by dividing the number of trabecular connections by the amount of bone mass in the volume scanned. Analysis of variance was applied to analyze differences between groups, and Tukey's post-hoc test was applied to identify groups that were significantly different ($P < 0.05$).

Results

The administration of PTH (1-34) at medium and high doses increased bone volume and trabecular thickness in osteopenic female rats. Trabecular connectivity only increased slightly when the doses were administered after 50% of the trabecular connectivity was lost. When the number of trabecular connections was normalized to volume of trabecular bone mass, the number of connections decreased for unit of bone in the PTH medium- and high-dose groups.

Discussion

These results demonstrate that trabecular bone volume and connectivity significantly decrease after eight and twelve weeks post-ovx. PTH (1-34) therapy increased bone volume and trabecular thickness to baseline levels or higher but did not appear to reestablish trabecular connectivity. In this study, PTH appears to increase bone mass by thickening existing trabeculae and not forming new trabeculae.

From these data, we hypothesize that to reestablish trabecular connectivity, a therapeutic intervention would have to given before significant distance between trabeculae has developed or treatment with a bone-forming agent (e.g., PTH) would have to be prolonged. Further studies are needed to refute or confirm our hypothesis.

References

1. Shen et al., *J. Clin. Invest.* **91**, 2479, 1993.
2. L. Mosekilde, *Endocrin* **134**, 2126, 1994.
3. J. H. Kinney et al., *Transactions ORS* **19**, 56, 1994.

Publications

Lane, N. E., J. M. Thompson, D. Haupt, and J. Kinney, "Intermittent Therapy with Parathyroid Hormone (1-34) Increases Trabecular Bone Mass but Not Connectivity in Osteopenic Rats," submitted to *Transactions of Orthopaedic Research Society*.

Kinney, J. H., N. E. Lane, and D. L. Haupt, "3D In Vivo Morphometry of Trabecular Bone," *J. Bone Miner. Res.* (in press).

Table 1. The effect of PTH therapy on the bone mass and connectivity of rats. Data are presented as the mean ± standard deviation.

Groups	Bone volume (%)	Trabecular thickness (μm)	Connectivity/ m^3 β_1	Connectivity/ bone mass
Sham	25.0 ± 3.9	86.3 ± 11	57.8 ± 18	229.7 ± 56
Ovx	16.9 ± 2.2[a]	71.6 ± 14	29.4 ± 11[a]	175.6 ± 68
Ovx + 0	15.2 ± 5.5[a]	72.9 ± 8	24.5 ± 14[a]	154.4 ± 33[a]
PTH (low dose)	17.4 ± 5.4	77.9 ± 12	24.9 ± 6[a]	147.8 ± 28[a]
PTH (medium dose)	25.1 ± 6.7[b]	110 ± 15[a,b]	34.6 ± 14[a]	136.0 ± 27[a]
PTH (high dose)	27.8 ± 6.7[b]	100 ± 22[a,b]	31.7 ± 11[a]	112.6 ± 20[a]

[a] $P < 0.05$ from sham.

[b] $P < 0.05$ from ovx + 0.

Bonding and Structure of Nanocrystalline Thin Films

L. J. Terminello

Overview

Our goal was to develop core-level, soft x-ray photoabsorption into an analytic tool for determining the bonding and structure of incommensurate, or amorphous, thin films of technological interest—in particular, boron nitride and carbon thin films. These films are of great interest to the coatings and microelectronics industries for their tribological and passivation properties.

Frequently, amorphous films have desirable mechanical, electronic, or chemical properties, but understanding the relationship between properties and structure requires detailed atomic structural information. Unfortunately, conventional structure determining tools that are used to characterize most materials are inaccurate when applied to films or clusters that have long-range order, or domain sizes, less than the coherence length of atomic-structure-probing x rays (<10 nm) or the wavelength of bond-sensitive probes (infrared and Raman <100 nm). Only a local atomic structural probe like core-level photoabsorption can measure the actual bonding and structure in these incommensurate-phase materials. Our plan was to measure core-level photoabsorption from boron nitride standards and thin films to establish the efficacy and viability of the core-level photoabsorption technique as a nanostructural tool at LLNL. We have succeeded in this phase of the project.

Core-level photoabsorption probes the empty, or unfilled, electronic states of a material. Experimentally, a monochromatic soft x-ray beam from a synchrotron radiation source is impingant on a sample in a high or ultrahigh (10^{-8} to 10^{-11} Torr) vacuum chamber. As the scanned photon energy passes through the core-electron binding energies of the atoms present in the material (100 eV and above), resonances are observed in the absorption cross section and are measured by monitoring the total or partial electron yield produced in the excitation process. This experimental procedure gives a depth sensitivity of 5 nm, thereby sampling the bulk of the thin film and remaining insensitive to surface contaminants. These resonances found near the core-electron binding energies constitute the NEXAFS spectra. Element selectivity is achieved by choosing specific core levels of the constituent atoms in a material. Dipole selection rules dictate which transitions are allowed and reveal the orbital angular momentum of the empty states (final states) when a well-defined core level (initial state) and linearly polarized x rays are used. Measuring the final-state angular momentum is instrumental in determining the bond order of the atom being probed and its local electronic structure. Thus, the bonding structure can be extracted from the NEXAFS measurement.

Technical Activities

We characterized the bonding of the hexagonal, cubic, rhombohedral, and wurtzite phases of boron nitride using core-level photoabsorption. In our measurements we can identify unique spectral features in the photoabsorption cross section and associate these resonances with each phase. Also, because core-level photoabsorption obeys dipole optical selection rules, we can concurrently identify the type of bonding present in the structurally characterized material, in particular, the presence of conjugated p bands indicative of sp^2-like bonding in an incoherent boron nitride–silicon(100) film.

Hexagonal, cubic, rhombohedral, and wurtzite boron nitride (hBN, cBN, rBN, and wBN, respectively) powders were pressed into a tantalum foil for introduction into the ultrahigh vacuum apparatus that was used in the core-level photoabsorption measurements. The metastable wBN, rBN, and cBN powders that would serve as our spectroscopic standards were measured using x-ray diffraction to determine the phase purity. The cubic material

was found to be pure cBN with trace metallic impurities, and the rBN and wBN were found to be 94 and 93% pure, respectively, with the remainder being the hexagonal phase source material used in synthesizing these two powders.

An incoherent boron nitride–silicon film was prepared at General Motors using ion-assisted, pulsed-laser deposition according to procedures described previously. According to x-ray diffraction results, the 70-nm-thick film showed no long-range structural ordering, indicating that this film had an amorphous, or incoherent, structure (i.e., the grain or domain size was smaller than the coherence length of the x-ray probe). Other spectroscopic studies of this fine-grained film using infrared absorption indicate the domain size of the boron nitride films are smaller than the phonon wavelength (about 200 nm) and confirm the amorphous character of this film. Thin-film samples prepared by other methods have produced fine-grained or amorphous films as well.

The boron and nitrogen $1s$ photoabsorption from each of these samples were measured using monochromatized synchrotron radiation and are shown in Fig. 1 for the boron $1s$ edge and Fig. 2 for the nitrogen $1s$ edge. Using the NEXAFS measurements from these four phases of boron nitride, we can assess the bonding of the boron nitride–silicon thin film. It is evident from the boron $1s$ photoabsorption in Fig. 1 that the boron nitride–silicon sample has the strong $1s–\pi^*$ resonance at 192 eV indicative of sp^2 bonding as is observed in the hexagonal phase of boron nitride. The same is true for the nitrogen $1s$ photoabsorption edge shown in Fig. 2.

One difference is noticeable between the boron nitride–silicon and hBN boron $1s$ spectra: the resonance at 200 eV is more pronounced in the boron nitride–silicon film than in the hBN sample. In the nitrogen spectrum, the resonance at 407 eV is higher than the edge peak for the boron nitride–silicon sample, but the opposite is true for the hBN sample. One

explanation for this could be contribution of cubic-phase, or sp^3-related resonances to the NEXAFS measurements. This is supported by infrared absorption measurements on this boron nitride–silicon film that indicate the presence of about 15% cBN. While there is no unique evidence of cBN in this qualitative assessment of the near-edge structure of boron nitride–silicon film, the NEXAFS measurements are useful for determining the sp^2 bonding present in the thin film.

We were also able to determine that the film was mainly sp^2-bonded material but was not entirely amorphous. Using a polarization-dependent NEXAFS measurement, we determined that the boron nitride film was preferentially ordered with the hBN planes lying nearly perpendicular to the surface normal (within 20 deg). This counterintuitive film structure was supported by recently published transmission electron microscope results that show laser-ablated boron nitride films can have such an oriented hBN-like component. In fact, electron diffraction measurements of our film confirm this perpendicular stacking of hexagonal boron nitride sheets.

Publications

A. Chaiken, L. J. Terminello, J. Wong, G. L. Doll, and C. A. Taylor, II (1993), "Electronic and Atomic Structure of Metastable Phases of Boron Nitride Using Core-Level Photoabsorption," *Appl. Phys. Lett.* **63**, 2112.

A. Chaiken, L. J. Terminello, D. A. Lapiano-Smith, E. Hudson, G. L. Doll, and C. A. Taylor, II (in press), "X-Ray Absorption Study of Pulse Laser Deposited Boron Nitride Films," in *Proc. Materials Research Society Symp.*

L. J. Terminello, A. Chaiken, D. A. Lapiano-Smith, G. L. Doll, T. Sato (in press), "Morphology and Bonding Measured from Boron Nitride Powders and Films Using Near Edge X-Ray Absorption Fine Structure," *J. Vac. Sci. Technol. A.*
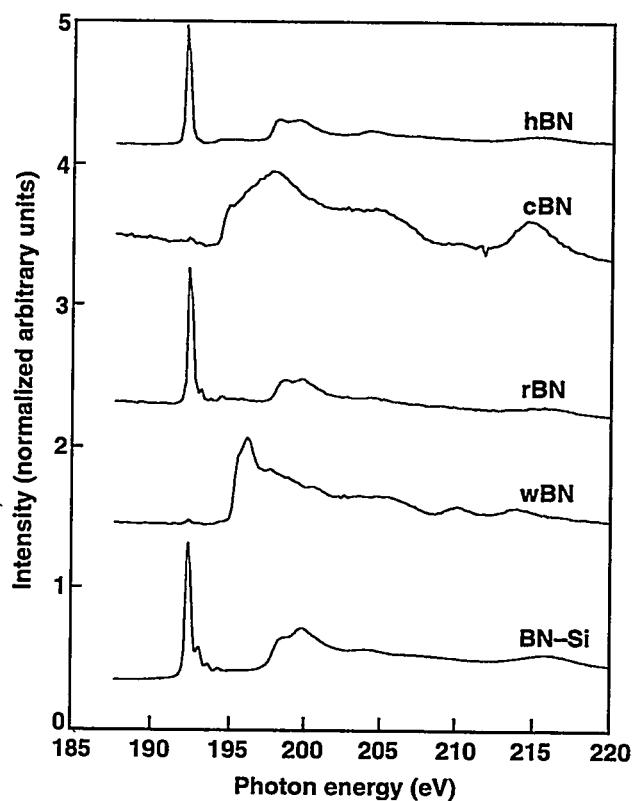
Figure 1. Boron 1*s* core-level photo-absorption for hBN, cBN, rBN, and wBN phases of boron nitride and a boron nitride thin film grown by ion-assisted, pulsed-laser deposition. Each spectrum was photon flux normalized and scaled. Note that the π^* feature at 192.0 eV that is identified with hBN is also present in the rBN and boron nitride–silicon samples.

Figure 2. Nitrogen 1*s* photoabsorption for the hBN, cBN, rBN, wBN, and boron nitride–silicon samples presented in Fig. 1. Here the resonances are not as prominent as those at the boron 1*s* edge; however, the relative energy positions and intensities are valuable for understanding the atomic distribution for the electronic density of states when compared to the corresponding boron 1*s* features.
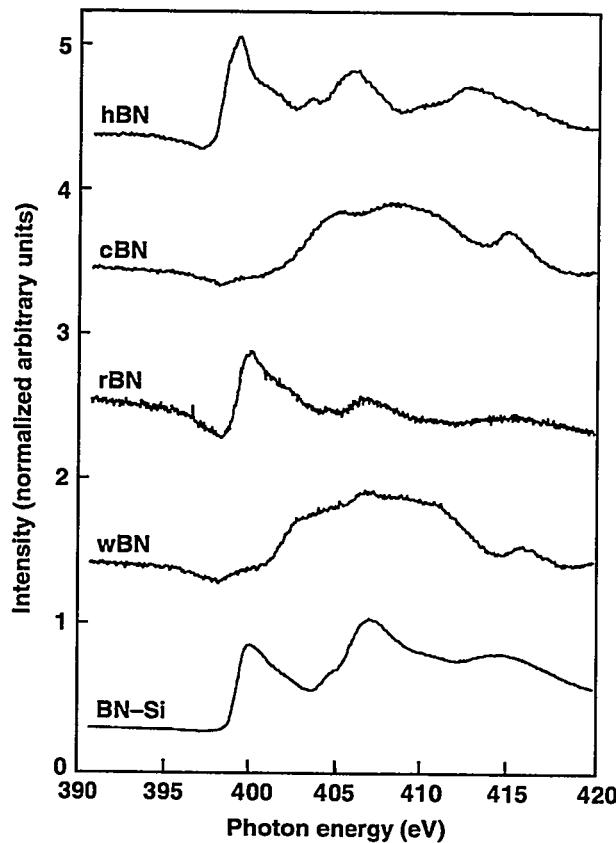
Multilayer Thermoelectric Thin Films

J. C. Farmer, T. W. Barbee, Jr., G. C. Chapline, Jr., R. J. Foreman, L. J. Summers, A. V. Wagner, M. D. Dresselhaus,[*] L. D. Hicks,[*] and M. J. Matthews[*]

Introduction

An enhanced dimension-less figure of merit (ZT) may be possible through the formation of two-dimensional quantum wells. Electrical conductivity is enhanced in two-dimensional quantum wells by restricting the motion of the charge carriers to the plane of the quantum well. This approach to improved electrical conductivity is preferred because additional doping would be detrimental to the Seebeck coefficient. We are synthesizing and evaluating a variety of single-layer, bilayer, and multilayer thermoelectric films with sufficiently thin layers to serve as quantum wells. We determined Seebeck coefficients and electrical conductivities over a broad temperature range.

Progress

Initially, we attempted to prepare multilayers from Bi_2Te_3, a well-known, low-temperature thermoelectric material. We made a number of unsuccessful attempts with dual-magnetron sputtering to deposit thin layers of Bi_2Te_3, separated by a variety of barrier materials. Eventually, some degree of success was achieved by using B_4C as a barrier layer. These films were characterized using x-ray diffraction (XRD) and transmission electron microscopy (TEM) with selected-area electron diffraction. The structure of the film was disappointing. The B_4C layer was virtually amorphous, while the Bi_2Te_3 was polycrystalline. Data indicated the presence of two crystalline phases, rhombohedral and face-centered cubic (fcc) NaCl-type structures, respectively. Interfaces were unusually rough.

As expected from the structural characterization, measurements of the Seebeck coefficient and electrical conductivity were disappointing. For example, a film with a total thickness of 690 nm and 23.5-nm layer pairs had an electrical resistivity of 38 $m\Omega \cdot cm$ and a Seebeck coefficient of -480 $\mu V/K$ near ambient temperature. These measured properties are poor in comparison to those published for single crystals of Bi_2Te_3 at 300 K, which are 2 $m\Omega \cdot cm$ and $+220$ $\mu V/K$, respectively.[1] Carrier transport in the imperfect Bi_2Te_3/B_4C multilayer is probably limited by scattering and interfacial trapping. The n-type behavior of this film is surprising and may be due to the presence of the fcc NaCl-type phase.

It is now believed that $Si_{80}Ge_{20}/Si$ heterostructures synthesized with molecular-beam epitaxy (MBE) have exceptional thermoelectric performance (ZT $\geq$ 1). This heterostructure system is of interest because $Si_{80}Ge_{20}$ is the preferred thermoelectric material for high-temperature applications. These factors prompted us to use dual-magnetron sputtering to synthesize $Si_{80}Ge_{20}/Si$ bilayer and multilayer films by alternating heavily doped n-type $Si_{80}Ge_{20}$ and lightly doped silicon. The carrier density in the $Si_{80}Ge_{20}$ sputtering target was determined to be approximately 10^{19} cm^{-3} by making Hall effect measurements.

Films were deposited on device-quality Si(100) substrates having a resistivity of 10 $\Omega \cdot cm$, high-purity float-zone Si(100) substrates having a resistivity of 1000 $\Omega \cdot cm$, and single-crystal sapphire substrates. We attempted to manipulate the film structure and electronic properties by controlling the substrate temperature during deposition. Amorphous-to-polycrystalline films were deposited on the 1000 $\Omega \cdot cm$ Si(100) at substrate temperatures ranging from approximately 25 to 410°C (35% of the melting point of the film). Beautiful bilayer and multilayer films with excellent

[*] Massachusetts Institute of Technology, Department of Physics.

interfaces were produced. Each $Si_{80}Ge_{20}/Si$ layer pair had a combined thickness of 13.3 nm. The thickness of a typical multilayer film was 850 nm. All films deposited on 1000 $\Omega \cdot$ cm Si(100) were electronically conductive. However, films deposited on heated substrates (410°C) were much more conductive than those deposited on low temperature substrates (25°C). Substrate heating enhanced electronic conductivity by a factor of 5.

In contrast, films deposited on low-temperature silicon, as well as on sapphire, were amorphous and proved to be very poor electronic conductors. Our differential hot stage instrument was used to measure the Seebeck coefficient and electrical resistivity between ambient temperature and 200°C. Dramatic drops in both properties were observed as samples were heated above a threshold temperature. These drops are attributed to a thermal activation of charge carriers. For example, a $Si_{80}Ge_{20}/Si$ multilayer deposited on heated 1000 $\Omega \cdot$ cm Si(100) had a Seebeck coefficient of –650 µV/K and a resistivity of 1.5 $\Omega \cdot$ cm at ambient temperature. These values dropped to less than –350 µV/K and 0.4 $\Omega \cdot$ cm, respectively, as the temperature was increased through 90°C to a maximum of 200°C. Further increases in temperature should continue to enhance the electrical conductivity. The change in transport properties was completely reversible. As the film cooled, the Seebeck coefficient and electrical resistivity returned to their original values of –650 µV/K and 1.5 $\Omega \cdot$ cm.

While performing a similar experiment with a $Si_{80}Ge_{20}/Si$ multilayer deposited on cooled 1000 $\Omega \cdot$ cm Si(100), significant irreversibility due to annealing was observed. Measured properties failed to return to original values after cooling. As the sample was heated, the resistivity dropped to a minimum of 0.1 $\Omega \cdot$ cm. Comparable values for bulk n-type $Si_{80}Ge_{20}$ have been recently published and are –90 µV/K and 0.75 m$\Omega \cdot$ cm, respectively.[2] The sputtered single-layer, bilayer, and multilayer $Si_{80}Ge_{20}/Si$ films are scientifically interesting in that they may provide insight into (1) interfacial trapping of charge carriers in materials with unusually high interfacial areas and (2) the trapping of charge carriers by broken bonds in disordered silicon and silicon-germanium alloys. Because these materials

have very high Seebeck coefficients and reasonable electronic conductivity, they may be useful in various types of thermal sensors. However, they do not appear to be promising thermoelectric materials for application in Peltier coolers and power generators. Future attempts to enhance the thermoelectric properties of this class of films should focus on higher substrate temperatures, slower deposition rates, and synthesis by MBE. Sputtered films of other high-temperature thermoelectric materials, such as doped $FeSi_2$, should also be investigated.

We are making good progress towards synthesizing $Bi_{0.9}Sb_{0.1}/PbTe_{0.8}Se_{0.2}$ films on glass as well as single-crystal silicon and single-crystal sapphire substrates. The Hicks–Dresselhaus model for two-dimensional quantum wells predicts that an exceptional ZT should be achievable with 10-nm layers of $Bi_{0.9}Sb_{0.1}$ separated by $PbTe_{0.8}Se_{0.2}$ barriers. We have now demonstrated that we can make excellent single-layer films of both $Bi_{0.9}Sb_{0.1}$ and $PbTe_{0.8}Se_{0.2}$. We also made beautiful bilayer and multilayer $Bi_{0.9}Sb_{0.1}/Pb_{0.8}Te_{0.2}$ films with very sharp interfaces. The abrupt compositional change at the $Bi_{0.9}Sb_{0.1}/PbTe_{0.8}Se_{0.2}$ interface has been verified with Auger electron spectroscopy depth profiling. TEM with selected-area electron diffraction also revealed distinct interfaces between layers and crystalline structure with preferred orientation within individual layers. Thermoelectric properties of these films have been determined over a temperature range extending from approximately 25 to 160°C. For example, a bilayer film on glass that consisted of 120 nm of $Bi_{0.9}Sb_{0.1}$ covered by 30 nm of $PbTe_{0.8}Se_{0.2}$ had an electrical resistivity less than 2 m$\Omega \cdot$ cm and a Seebeck coefficient of about –220 µV/K. These thermoelectric properties are respectable.

We are completing construction of a vacuum system with a differential temperature stage and four-point probe that will allow measurements of electrical conductivity and Seebeck coefficient between the boiling point of liquid nitrogen and ambient temperature. Vacuum is established and maintained by a turbomolecular pump backed by a mechanical roughing pump. This system will also allow measurements at high temperature and under a good vacuum.

Discussion

If we are able to synthesize promising thermoelectric thin films, we anticipate the following applications:

- Miniaturized thermal sensors and analytical instruments, including a miniature differential scanning calorimeter. A thermoelectric device can be used for both heating and cooling, depending upon the direction of current flow. The energy input to the device can be regulated precisely.
- Device for thermal-cycling solutions of DNA during replication (polymerase chain reaction technique).
- Thin-film coolers and power generators than can be incorporated directly into microelectronics. This will become more important as microprocessors become more powerful and generate more heat.
- Solar-heated thermoelectric power generators based upon thin films.

References

1. D.-B. Hyun, H.-P. Ha, and J.-D. Shim, "Electrical and Thermoelectric Properties of Bi_2Te_3–Bi_2Se_3 Single Crystals," in *Proc. XIth Int. Conf. Thermoelectrics*, K. R. Rao, Ed. (University of Texas, Arlington, TX, 1992).

2. L. W. Fu, D. M. Rowe, and G. Min, "The Effect of Heat Treatment on the Electrical Power Factor of High-Temperature Annealed N-Sige Gap Thermoelectric Alloys," *J. Phys. D* 26, 1796–1798 (1993).

Publications and Presentations

Farmer, J. C., T. W. Barbee, R. J. Foreman, and L. J. Summers (1994), "Deposition and Evaluation of Multilayer Thermoelectric Films," in *Proc. Symp. Microstructures and Microfabricated Systems, 185th Electrochemical Society Meeting* (Electrochemical Society, Pennington, NJ), vol. 94-1, p. 231.

Farmer, J. C., T. W. Barbee, R. J. Foreman, and L. J. Summers (1994), "Deposition and Evaluation of Multilayer Thermoelectric Films," in *Proc. Symp. Microstructures and Microfabricated Systems, 185th Electrochemical Society Meeting,* (Electrochemical Society, Pennington, NJ), ext. abstract, vol. 94-1, p. 1661.

Farmer, J. C., S. Ghamaty, and B. Elsner (1994), "Synthesis and Evaluation of Novel Thermoelectric Thin Films," in *Symp. Materials Synthesis and Characterization, Division of Industrial and Engineering Chemistry, 207th Meeting American Chemical Society* (American Chemical Society), Paper No. 74.

Magnetoresistive Materials with Novel Spacer Layers

A. Chaiken and R. P. Michel

Overview

Our goal is to enhance understanding of the giant magnetoresistance phenomenon that has been observed in ferromagnetic-metal–paramagnetic-metal multilayers by extending the research to ferromagnetic-metal–semiconductor systems. In addition, we will study the behavior of the antiferromagnetic interlayer coupling that has often been associated with observations of giant magnetoresistance. To perform these experiments, we designed and built a computer-controlled ion-beam sputtering system and prepared our first multilayers. We characterized the magnetic properties of these multilayers using a newly assembled vibrating-sample magnetometer and began observing the magnetoresistance using a newly constructed magnetotransport measurement system. We have already observed antiferromagnetic coupling in the Fe/Si multilayer system and have performed preliminary magnetotransport measurements.

During the first six months of our project, we constructed the necessary film deposition and characterization equipment for the project.

We completed an ion-beam sputtering system and prepared the first multilayers. The system incorporates a computer-controlled "electronic shutter" system for good control and reproducibility in layer thicknesses. In addition, we designed and built a liquid-nitrogen-substrate cooling system so we could deposit in a layered geometry materials that would otherwise immediately form an alloy. The success of this cooling is illustrated in the low-angle x-ray diffraction pattern shown in Fig. 1 for a $(Fe30\text{Å}/Si20\text{Å}) \times 50$ multilayer. The pattern shows an interplanar spacing of 42 Å, indicating that the two materials have reacted slightly in forming a multilayer structure.

We also observed antiferromagnetic interlayer coupling in Fe/Si multilayers, as shown in Fig. 2. Similar coupling has been observed in $Fe/FeSi_2$ and $Fe/FeSi_2/Si/FeSi_2$ multilayers, which we studied to determine the effect of interface diffusion. The large magnetic field required to saturate the Fe/Si multilayer's magnetization and the low remanent magnetization are classic signs of a spacer-layer-mediated interlayer coupling. Observation of this coupling is of fundamental interest in
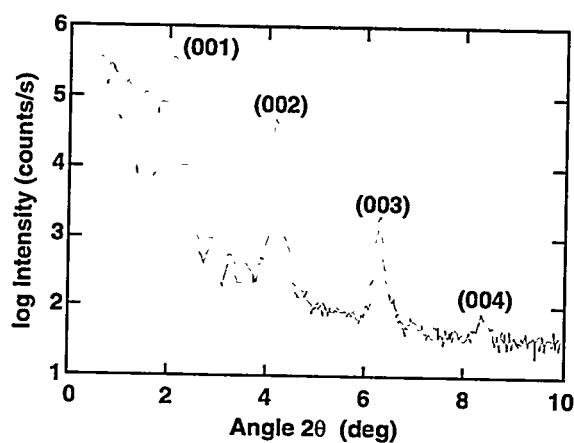
Figure 1. Low-angle x-ray diffraction pattern of Fe/Si multilayer; L = 41.82 Å.
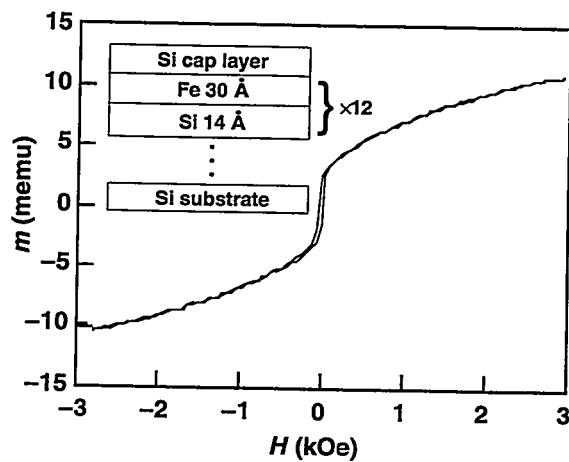
Figure 2. Magnetization curve of an Fe/Si multilayer.

nonmetallic systems, where its origin is not clear. However, we believe that the coupling in these Fe/Si multilayers is mediated by roughness at the multilayer interfaces, where projecting terraces of iron act like tiny bar magnets that want to align antiparallel. Detailed x-ray diffraction studies of these multilayers are underway that will allow quantitative comparison of observed roughness with recent theories. Soon-to-be-completed transmission electron microscopy studies and polarized neutron reflectometry studies on these samples should shed more light on these issues.

Recently workers at the Massachusetts Institute of Technology and Tohoku University reported large magnetoresistance at low fields in $Fe/Al_2O_3/Fe$ sandwiches, similar in conception to the perpendicular-transport iron/insulator/iron devices envisioned in this proposal. We hope to achieve results of similar importance soon.

Fundamental Studies of Particle–Solid Interactions

T. Diaz de la Rubia and M. W. Guinan

Introduction

The aim of our research is to improve our understanding of nonequilibrium processing of materials with energetic beams. Our goal is to develop models of defect production and transport in materials to help industry develop improved macroscopic modeling tools for the manufacturing of next-generation electronic components and other advanced materials.

As the dimensions of integrated circuits decrease, and the cost and complexity of manufacturing increases, empirical approaches to industrial process design cease to be practical. Hence, process modeling of device manufacturing becomes critical. However, process modeling currently is not predictive, with the main limitation being a lack of complete understanding of the physical processes involved. For example, understanding defect production during ion implantation as well as dopant diffusion and activation is vital to supporting shallow junction technologies. Addressing these limitations is one of the critical factors that will determine the future success of the semiconductor industry.

Through this project, we are developing a unique capability in the area of atomistic simulation of energetic particle interactions with solids. Our molecular dynamics codes use massively parallel computers to provide the physical insight that will allow us to describe the defect production and diffusion processes common to beam-assisted processing of materials. Our atomistic simulation codes—together with modern three-dimensional visualization tools and continuum transport simulation programs—will lead the way toward a comprehensive total computer aided design (TCAD) tool. This TCAD tool will provide a predictive process-modeling package for manufacturing the next generation of semiconductor integrated circuit components.

Semiconductor Device Processing with Ion Beams

We are presently carrying out molecular dynamics studies of ion implantation and defect properties in silicon at recoil energies up to 10 keV. The simulations employ crystallites with up to 356,000 atoms at temperatures from 80 to 600 K. The atoms interact through semi-empirical three-body interatomic potentials. The simulation cells have periodic boundaries in X and Y and a free surface in the (001) direction. To date, all simulations have been performed with the Stillinger–Weber potential for silicon.

The structure of the material in a cascade region changes dramatically during the period of the simulation. Analysis of the radial distribution function (rdf) at various times for a representative region of a displacement cascade shows that the structure at 1.0 ps is similar to that of liquid silicon, except for the presence of some crystalline peaks as a result of the surrounding crystalline matrix. The final structure at 7.0 ps is similar to that obtained for amorphous silicon, except for the presence of a sharp peak at 3.4 Å, corresponding to the shoulder that is usually observed for amorphous silicon. The average coordination number in this region, as determined by the integral of $g(r)$ out to the first minimum, was found to increase to a value of about 6.5 at 0.5 ps and decrease to about 4.3 after equilibration with the surrounding lattice. To compare directly with bulk silicon, we simulated two quenches from the liquid: one in 500 ps and the other in 5 ps. Both were performed at constant volume to duplicate as closely as possible the conditions of the cascade. The more rapid quench exhibits a peak at 3.4 Å, similar to that of the cascade region, suggesting that the amorphous material in this region has a structure that is determined by the fast conduction of heat to the surrounding crystal.

The results of these molecular dynamics simulations provide insight into the defect production process in silicon. One of the most striking results of this work is that very few isolated Frenkel pairs are produced directly by the displacement cascades. This can be understood by considering that isolated point defects are produced in cascades by replacement collision sequences (RCSs) along low-index crystallographic directions. As we have recently shown, such RCSs in silicon are extremely short (2 to 3 atomic replacements long at most). Therefore, the probability of such an RCS producing a stable (i.e., separated beyond its own spontaneous recombination volume) vacancy-interstitial pair during the 5-keV cascades is small. Our simulations resulted in an average of 3 to 5 isolated Frenkel pairs per 5-keV cascade, a number only about 4.5% that predicted by binary collision models such as the modified Kinchin–Pease expression of Sigmund and Norgett et al.[1] However, large pockets of highly unrelaxed amorphous material are produced by the displacement cascades. Because of the energetic collisions and large atomic rearrangements induced by the incoming particle, these amorphous regions contain density fluctuations. Also, it is expected from experimental evidence that these amorphous pockets will not be stable at temperatures above about 350°C. Upon annealing at an elevated temperature, these density fluctuations will then result in the appearance of vacancies and self-interstitial atoms in the recrystallized material. These defects can then participate in the transient-enhanced diffusion of dopant atoms that is commonly observed in low-energy, ion-implanted silicon.

In conclusion, we have simulated the collisions of 5-keV silicon ions with a silicon substrate. We found that amorphous material is left after the cascades cool to the ambient temperature. The number of atoms in the amorphous regions is in agreement with the 10-eV/atom amorphization energy observed in ion-implantation experiments on a number of different systems. The structure of the amorphous regions is similar to that of bulk silicon quenched from the melting point to 0 K in 5 ps. This is consistent with the fact that the cascade regions have a structure similar to liquid silicon during the 2-ps period and that the kinetic energy in the region is close to that of liquid silicon. Tensile stress results from the collisions,

and the density of the silicon substrate is increased. These effects are the opposite of those observed in metallic systems but are caused by the fact that liquid silicon has a higher density than that of the crystal. Atomic mixing in the cascade occurs.

For low-energy recoils, we have seen that the threshold energy for defect production in silicon is highly anisotropic. For recoils along [111], the threshold may be as low as 18 eV. However, along [110], values as high as 45 eV were found. As noted above, the open nature of the diamond lattice results in very short replacement collision sequences (two to three atomic replacements at most). The defects produced by these low-energy recoils were found to be a vacancy and [110] dumbbell self-interstitial. When a tetrahedral interstitial was produced, as was the case for low-energy recoils along [111], it readily converted to the more stable [110] dumbbell form. The energy difference between these two configurations was found to be 1.2 eV. The split dumbbell interstitial is in good agreement with the predictions of ab initio calculations.

To explore the motion of amorphous-crystalline (a-c) interfaces in silicon, a process of critical importance in the development of ultrashallow junctions, we first studied the threshold energy for producing defects in amorphous silicon. The a-silicon was produced by quenching of a high temperature melt, and a structure with a coordination number of 4.2 was obtained. The recoils were launched in the a-silicon matrix with recoil energies of 10, 15, and 20 eV. For these energies, we found that the probability of forming a defect was independent of recoil direction and had a value of 14, 66, and 97%, respectively. Note that for 20-eV recoils, the probability of forming a defect is much higher in the amorphous matrix than in a crystalline lattice, where a defect can be formed only for recoils along [111].

We applied these observations to understanding the motion of an a-c silicon interface that was prepared as follows. The whole crystal was first equilibrated at 1200 K for about 3 ps. The top half of the crystallite was then brought to a temperature well above the melting point for a few picoseconds, while the bottom was held at a constant 1200 K through the application of an isokinetic thermostat. After this period, the full system was quenched down to 10 K through the application of a quasidynamic

algorithm. In this method, only the velocities of atoms for which the product of the velocity and the acceleration is negative are made equal to zero at any given time-step. Prior to launching of the recoils, the system was further equilibrated for several picoseconds. The final equilibrium temperature was 170 K, and the a-c interface was located near the center of the crystallite. The average coordination number on the first neighbor shell is 4.3 for the top (amorphous) half and 4 for the bottom (crystalline) half. A small peak in the inner part of the second peak in $g(r)$ for the amorphous half is due to the rapid quench of the liquid and is consistent with results for the amorphous zones produced by 5-keV silicon recoils in silicon. A nonequilibrium a-c interface was prepared that is consistent with irradiation experiments where it is well known that the amorphous phase produced is highly unrelaxed and contains large numbers of defects.

The recoil-induced motion of this interface was studied by sequentially launching 20-eV recoils from either the crystalline or amorphous sides of the interface. The time interval between recoils was 2.5 ps, which was sufficient to avoid direct temporal overlap of the damage regions. The spatial location of the recoils was chosen at random, but for simplicity was kept to within two atomic planes of the a-c interface. As the interface moved, the planes from which the recoils were launched were moved as well. The direction of the recoil was always toward the interface, but the azimuthal angle was chosen at random.

For 300 recoils started from the amorphous side of the a-c interface, solid-phase epitaxy

was found to occur. The potential energy-per-atom (E_p/N) for the crystalline and amorphous halves of the original system varies as the number of recoils is increased. Clearly, E_p/N decreases toward the baseline value of the crystal half as the recrystallization of the amorphous material takes place by solid-phase epitaxy. The slope of this curve is -3.4×10^{-4}, which indicates that the efficiency for recrystallization of these 20 eV recoils is about 1. That is, one atom is transformed from the amorphous to the crystalline phase per recoil. However, if the same 20-eV recoils are initiated on the crystalline side of the interface, little motion is detected even after 120 events.

In summary, we have seen that the motion of an a-c interface in silicon may be induced by recoils with energy below the threshold for producing Frenkel pairs in crystalline silicon. We also found that this threshold is substantially lower in a-silicon, which explains the experimentally observed recrystallization of a-silicon in an electron microscope with electron energies below the crystalline threshold. For 20-eV recoils launched from the amorphous side of the interface, the defects produced, which are mostly single vacancies, mediate the solid-phase epitaxy at the interface. Further studies of the recrystallization of planar a-c silicon interfaces during high-energy ion irradiation are underway.

Reference

1. Sigmund and Norgett et al.

Ductile-Phase Toughening of Refractory Metal Intermetallics

G. A. Henshall and M. J. Strum

Overview

The continuing search for improved lightweight structural materials for high-temperature service has led to the investigation of intermetallic compounds based on the refractory metals. The major barrier to their use is the lack of ambient-temperature toughness required for damage tolerance. To solve this problem, we are exploring ductile-phase toughening, where a high-melting-point ductile phase is dispersed within the intermetallic matrix. The ductile phase may increase toughness by

- "Bridging" the crack faces, thereby inhibiting crack opening,
- Blunting the crack tip, or
- "Trapping" the crack at interfaces

between the phases.

To produce these composites, we are investigating in situ synthesis methods in which the two components of the composite form by phase separation during solidification.

Experimental Investigations

During this reporting period, we performed another set of room-temperature fracture-toughness experiments on directionally solidified (DS) eutectic V/V_3Si composites. These composites have a microstructure consisting of aligned 2-μm-diam V_3Si rods in a vanadium–silicon solid solution, (V), matrix. In these experiments, the direction of crack propagation was designed to be parallel, rather than transverse, to the axes of the V_3Si rods, or growth direction.[1] A fracture toughness, K_Q, of 14.4 MPa · $\sqrt{m}$ was measured for this orientation (DS–L), compared with 18.5 MPa · $\sqrt{m}$ for the same material tested with the crack propagating transverse to the growth direction (DS–T). Preliminary analysis suggests that the toughness decrease for the DS–L orientation

may result from either an increased constraint in the (V) or a reduction in the amount of crack renucleation required in the V_3Si.

For specimens with a random or transverse orientation of the crack with respect to the axes of the V_3Si rods, analysis performed during this reporting period revealed that the fracture toughness decreases with increasing "effective" interstitial impurity content, defined as [N]+1.33[O]+9[H].[1] As shown in Fig. 1, these data include specimens that were arc melted (AM), cold-crucible induction melted (IM), and (DS–T) data. Fracture toughness is predicted to increase above 20 MPa · $\sqrt{m}$ (the industrial target value) for effective interstitial impurity concentrations below about 300 ppm. In summary, the chemistry and microstructure required to achieve a toughness meeting the industrial target value and the synthesis methods required to achieve them have been largely determined.

The steady-state creep properties of the AM V/V_3Si eutectic composite were measured at 1200°C by strain-rate-change testing. Together with earlier data at 1400°C, the results indicate that the stress exponent for creep of the com-
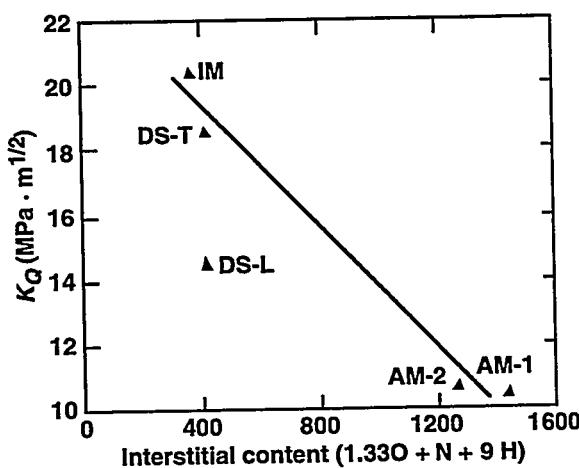

Figure 1. The fracture toughness of V–V$_3$Si eutectic composites as a function of effective interstitial content.

posite is about 5, similar to many metals, and that the activation energy for creep, Q_c, is about 470 kJ/mol. The measured Q_c is greater than that for self diffusion in vanadium (330 kJ/mol) or for creep in V_3Si (140 kJ/mol).[2,3] The measured Q_c may be high because of internal damage (voiding) produced during testing at 1400°C, which results in strain softening and erroneously low stresses at the higher strain rates. For the composite deformed at 1400°C, transmission electron microscopy shows the presence of a dislocation substructure, including subgrain boundaries, in the V_3Si. These findings confirm that high-temperature deformation in the intermetallic phase of the composite occurs by dislocation slip.

Stress Analyses

One of the major goals of the continuum stress analyses performed as part of this program is to determine how severely the addition of a ductile phase degrades the creep resistance of a strong refractory metal intermetallic. Efforts during this reporting period have clarified the quantitative relationships. The addition of the weak ductile phase is predicted to degrade the creep resistance of the intermetallic more severely with increases in (1) the stress exponent of the intermetallic, (2) the creep rate of the ductile phase, and (3) the volume fraction of the ductile phase. Figure 2 illustrates these trends for the case of a strong matrix material with weak short fibers. The creep rate of the composite, ε_c relative to that of the strong matrix, ε_s, is plotted as a function of A_w/A_s, where A is a constant in the creep constitutive law and the subscripts refer to the weak and strong phases.

For the case in which the stress exponent, n, is the same for each phase, A_w/A_s defines the ratio of the monolithic steady-state creep rates; an increasingly weak ductile phase is simulated by increasing A_w/A_s. Note that for $n = 1.0$ (relevant to many intermetallics, such as V_3Si and Nb_5Si_3), the addition of up to 51.2% of a very weak ductile phase is not predicted to significantly degrade the creep resistance of the intermetallic. For the case in which the stress exponents for the two phases are unequal, the composite creep behavior "tracks" that of the phase with the lower creep rate. Thus, if the curves of creep rate vs applied stress for the

two individual phases cross each other, a change in composite stress exponent occurs at the applied stress where the cross occurs.

To compare the composite creep predictions with data for a system with a strong intermetallic matrix, we have collaborated with P. R. Subramanian and coworkers at UES, Inc., who are measuring the creep behavior of Nb_5Si_3/Nb in situ composites. Using their data, model predictions of the steady-state composite creep rate have been compared with the experimental results for a Nb–10 at. % Si alloy. While accurate at low stress, the models underestimate the composite creep rate at large stresses because the composite stress exponent is underestimated. However, the model properly predicts that the composite, which is about 73% (Nb), has a steady-state creep rate much lower than might be expected, e.g., by a rule-of-mixtures calculation. In the case of primary creep, the models somewhat overestimate the composite creep strain but are reasonably accurate given uncertainties in the primary creep data. Finally, FE predictions of large tensile stresses within the matrix between adjacent (Nb) dendrites are qualitatively consistent with the location of cracks observed experimentally during tertiary creep.
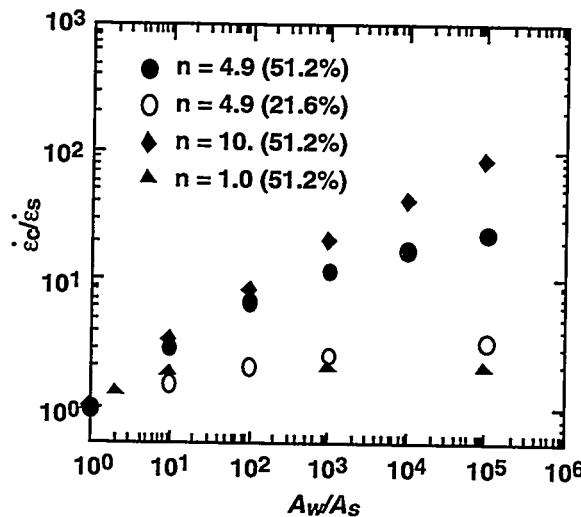

Figure 2. The predicted effect of A_w/A_s ratio on the relative composite strain rate for short fiber composites with a strong matrix. In all cases, $n_w = n_s = n$, and the volume fraction of weak fibers is given in parentheses.

References

1. M. J. Strum, G. A. Henshall, B. P. Bewlay, J. A. Sutliff, and M. R. Jackson, in *Proc. Mat. Res. Soc. Symp. High Temperature Silicides and Refractory Alloys*, B. P. Bewlay et al., Eds. (Materials Research Society, Pittsburgh, PA, 1994), pp. 511–516.
2. R. P. Agarwala, S. P. Murarka, and M. S. Anad, *Acta Metall.* **16**, pp. 61–67 (1968).
3. D. M. Shah and D. L. Anton, *Mater. Sci. Engin.* **A153**, pp. 402–409 (1992).

Publications

G. A. Henshall and M. J. Strum (1994), "Simulations of Deformation in Composites with Two Steady-State Creeping Phases," *Scr. Metall. Mater.* **30**, pp. 845–850.

M. J. Strum, G. A. Henshall, B. P. Bewlay, J. A. Sutliff, and M. R. Jackson (1994), "The Effects of In Situ Processing Methods on the Microstructure and Fracture Toughness of V–V$_3$Si Composites," in *Proc. Mat. Res. Soc. Symp., High Temperature Silicides and Refractory Alloys*, B. P. Bewlay et al., Eds. (Materials Research Society, Pittsburgh, PA), pp. 511–516.

G. A. Henshall, E. Zywicz, and M. J. Strum (1994), "Numerical Simulations of Interfacial Debonding in Ductile-Phase Reinforced Intermetallic Matrix Composites," in *Proc. TMS Symp. Fatigue and Fracture of Ordered Intermetallic Materials*, W. Soboyejo et al., Eds., pp. 39–54.

G. A. Henshall and M. J. Strum (1994), "Numerical Simulations of Creep in Ductile-Phase Toughened Intermetallic Matrix Composites," in *Proc. Mat. Res. Soc. Symp., Intermetallic Matrix Composites III*; J. A. Graves, R. Bowman, and J. J. Lewandowski, Eds. (Materials Research Society, Pittsburgh, PA), pp. 65–70.

G. A. Henshall and M. J. Strum (submitted), "Continuum Predictions of Deformation in Composites with Two Creeping Phases—I. Model Systems," *Acta Metall. Mater.*

G. A. Henshall, P. R. Subramanian, M. J. Strum, and M. G. Mendiratta (submitted), "Continuum Predictions of Deformation in Composites with Two Creeping Phases—II. Nb$_5$Si$_3$/Nb Composites," *Acta Metall. Mater.*

G. A. Henshall, M. J. Strum, P. R. Subramanian, and M. G. Mendiratta (in press), "Simulations of Creep in Ductile-Phase Toughened Nb$_5$Si$_3$/Nb In Situ Composites," in *High Temperature Ordered Intermetallic Alloys VI*, J. Horton et al., Eds.

G. A. Henshall, M. J. Strum, B. P. Bewlay, and J. A. Sutliff (in press), "The Influence of Chemistry and Microstructure on the Fracture Toughness of V–V$_3$Si In Situ Composites," in *Fatigue and Fracture of Ordered Intermetallic Materials: II*, T. S. Srivatsan, W. O. Soboyejo, and R. O. Ritchie, Eds.

Laboratory Directed Research and Development

Glenn T. Seaborg Institute
for Transactinium Science

Cation–Cation Complexes of Actinides

N. J. Stoyer, D. C. Hoffman, and R. J. Silva

Actinyl(V), An(V), cations form cation–cation complexes with a variety of cations, including other oxidation states of actinides. However, these other oxidation states of actinides do not form cation–cation complexes with any cation other than An(V). The interaction between Np(V) and U(VI) forming the Np(V)–U(VI) complex in an acidic noncomplexing media was the discovery of cation–cation complexes.[1]

Since 1961, about two dozen cation–cation complexes have been studied. Of the four actinides forming An(V) cations (uranium, neptunium, plutonium, and americium), Np(V) was studied the most, while Pu(V) was studied the least. Pu(V) is the only An(V) without an equilibrium constant determined for a cation–cation complex. The equilibrium constants for cation–cation complexes are small, ranging from 0.095 to 16.0 M^{-1}. The purpose of this study is to measure the equilibrium constant of at least one Pu(V) cation–cation complex and to study other cation–cation complexes. This is a challenge because the constant is likely to be small, Pu(V) has small molar absorptivities, and Pu(V) disproportionates into Pu(IV) and Pu(VI). The method chosen to study these complexes is laser-induced photoacoustic spectroscopy (LIPAS).

Because LIPAS had never been used to study cation–cation complexes, the first goal was to verify that this method could be used to measure the equilibrium constant of a known cation–cation complex. Using LIPAS, a value of 2.4 ± 0.2 M^{-1} at an ionic strength of 6 M ($NaClO_4$) was measured for the Np(V)–U(VI) complex. This result is consistent with the reported equilibrium constants of 2.25 ± 0.03 M^{-1}, 2.5 ± 0.5 M^{-1}, and 3.7 ± 0.1 M^{-1}, at ionic strengths from 6 to 7 M obtained using absorption spectroscopy or Raman spectroscopy.[2–4]

An experiment was conducted to study the formation of the Np(V)–Th(IV) complex. Previous reports indicate that this complex does form; however, its equilibrium constant had not been measured.[5,6] The result obtained using LIPAS is 1.8 ± 0.9 M^{-1} at an ionic strength of 6 M ($NaClO_4$). Figure 1 shows the spectra.

We conducted an experiment looking for the previously unknown Pu(V)–U(VI) cation–cation complex, using the 569-nm peak of Pu(V). The equilibrium constant for the Pu(V)–U(VI) complex is 2.2 ± 1.5 M^{-1} at an ionic strength of 6 M ($NaClO_4$). The previously unknown Pu(V)–Th(IV) complex was also studied using LIPAS. Results indicate formation of such a complex. Only a rough estimate for the equilibrium constant was obtained. A value of approximately 0.8 M^{-1} at an ionic strength of 6 M ($NaClO_4$) was measured.

The exploratory experiment looking for a Pu(V)–Np(V) cation–cation complex was not encouraging. LIPAS is so sensitive that the background from Np(V) around 569 nm is too large when working at the higher concentrations that is required to form the complex. Competition from the Np(V)–Np(V) cation–cation complex is expected to occur and might also interfere.

We also performed an exploratory experiment to determine the feasibility of looking at Pu(V)–Fe(III) cation–cation complexes. Because the disproportionation of Pu(V) is acid dependent, it appears that the acid concentration needed to prevent the hydrolysis of Fe(III) will make such complexes extremely difficult, if not impossible, to find using our method. This is because Pu(V) and Fe(III) are not present in the same solution for very long. An interaction between U(VI) and Th(IV), although not expected, was looked for. Results indicate no interaction between these two species.

The results presented here along with the results from previous years are detailed in the Ph. D. thesis of Nancy Jane Stoyer, University of California, Berkeley, December 1994 (reprint also available, LBL-36455).

References

1. J. C. Sullivan, J. C. Hindman, and A. J. Zielen, *J. Am. Chem. Soc.* **83**, 3373 (1961).
2. B. E. Stout, G. R. Choppin, F. Nectoux, and M. Pages, *Radiochim. Acta* **61**, 65 (1993).
3. B. Guillaume, G. M. Begun, and R. L. Hahn, *Inorg. Chem.* **21**(3), 1159 (1982).
4. C. Madic, B. Guillaume, J. C. Morisseau, and J. P. Moulin, *J. Inorg. Nucl. Chem.* **41**, 1027 (1979).
5. B. Guillaume, G. M. Begun, and R. L. Hahn, *Inorg. Chem.* **21**(3), 1159 (1984).
6. J. C. Sullivan, *J. Am. Chem. Soc.* **84**, 4256 (1962).
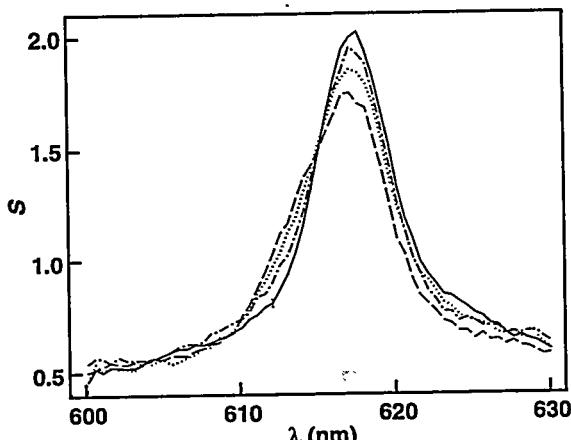
Figure 1. Spectra for the Np(V)–Th(IV) complex experiment at an ionic strength of 6 M. The spectra shown are for a calculated Np(V) concentration of 0.297 mM (solid line), 0.297 mM Np(V) with 0.218 M Th(IV) (dashed line), 0.297 mM Np(V) with 0.1088 M Th(IV) (dotted line), and 0.297 mM Np(V) with 0.0544 M Th(IV) (dot-dashed line). The error bar at 612.0 nm on the solid line is typical for these spectra. Note the ordinate scale does not begin with 0.

Electron-Capture Delayed Fission as a Probe of Nuclear Structure

S. A. Kreek, H. L. Hall, K. E. Gregorich, and D. C. Hoffman

Overview

Electron-capture delayed fission is a nuclear decay process in which a parent nucleus undergoes an electron-capture decay to excited states in the daughter nucleus that then fissions. Study of this process is valuable in understanding nuclear superdeformation, nuclear structure, fission barriers, and the astrophysical *r*-process. Potentially, information obtained from this study will elucidate previously unobserved details of nuclei far from beta stability. Currently, no other practical method is available that might provide the same insight.

As part of a joint collaborative effort between LLNL, Lawrence Berkeley Laboratory, and University of California, Berkeley, we are developing an x-ray–fission coincidence detector system and an automated sample-handling system for use in conjunction with Gammasphere (a large germanium gamma-ray detector array at Lawrence Berkeley Laboratory). Upon completion of the x-ray–fission coincidence detector system and sample handling system, we will measure ^{232}Am at the Lawrence Berkeley Laboratory's 88-Inch Cyclotron facility.

Technical Activities

We have completed the design of the x-ray–fission coincidence detector apparatus and the sample transport mechanisms. Necessary procurements are underway, and construction of the mechanisms has commenced.

Issues Addressed

The ^{232}Am will be produced via the ^{237}Np(α, 9n) reaction at the Lawrence Berkeley Laboratory's 88-Inch Cyclotron. The material will be transported via potassium chloride aerosols carried in helium to the automated sample collection and transport mechanism for positioning inside the x-ray–fission coincidence apparatus.

The x-ray–fission coincidence detector apparatus will consist of two thin silicon detectors for detection of fission fragments and two thin germanium detectors for measurement of low-energy gamma rays and x rays in coincidence with fission fragments. This detector assembly will be situated inside Gammasphere for simultaneous detection of higher-energy gamma rays.

The sample handling mechanism will consist of a four-station automated planchet changer and a slider assembly that will position the sample inside the x-ray–fission coincidence detector array inside Gammasphere. Station one will be a reservoir of clean polypropylene foils on which samples will be collected. One foil will be moved to station two by the automated planchet changer, and the potassium chloride aerosols containing the sample will be collected on it. The polypropylene foil and sample are then moved to station three where the transport slider assembly will remove the sample and polypropylene foil and position the sample inside the detector array. The sample will then be counted for a specified interval.

At the end of the counting interval, the transport slider assembly will reposition the sample in the planchet changer mechanism at station three, and the planchette changer will rotate the counted sample to station four. At the same time, a new sample will be positioned in the transport slider assembly for transport to the counting array. The previously counted sample foil is stored for subsequent manual inspection and cleaning in preparation for reuse of the foil.

Chemistry of Actinide–Mineral Interactions Investigated with Inner Shell Spectroscopies

L. J. Terminello and E. Hudson

Overview

The focus of this project is to establish and develop an effort through the G. T. Seaborg Institute for Transactinium Science to use inner shell spectroscopies to characterize the chemistry and physics of actinide–mineral interactions. The synchrotron radiation techniques of x-ray absorption spectroscopy (XAS) in both the extended (EXAFS) and near-edge (XANES) regions, x-ray photoelectron spectroscopy (XPS), and x-ray emission spectroscopy (XES) are used to characterize the chemical state, valency, and atomic and electronic structure of model actinide–mineral sorption complexes. Conventional methods that are generally used to characterize these types of complex materials frequently cannot handle dilute or hydrated real-life samples. To address these limitations, we are developing new techniques to apply these analytic methods to sorption complexes. In this project we are collaborating with B. Viani and C. Colmenares at LLNL and the Actinide Group headed by N. Edelstein at Lawrence Berkeley Laboratory.

Progress

Since the project began in October 1993, it has advanced in four main areas. First, two separate proposals requesting beam time for hard x-ray absorption measurements were submitted in early November to the Stanford Synchrotron Radiation Laboratory (SSRL). These new proposals were necessary to gain access to this Department of Energy user facility because any new program or project requesting beam time at the SSRL is required to undergo peer review. Reviews of these proposals were favorable and several periods of beam time were scheduled for the April–July period.

Second, experimental XANES spectra of several actinide compounds were theoretically modeled with remarkable success. This work is a collaboration with Professor John Rehr from the University of Washington. His modeling code FEFF can accurately simulate the final-state multiple scattering that a photoejected electron experiences during the photoabsorption process. The compounds modeled include uranium metal, UO_2, UO_3, UTe, and UCu_5. This capability will facilitate the interpretation of experimental results from SSRL.

Third, a high-performance soft x-ray beamline at the Advanced Light Source (ALS) at Lawrence Berkeley Laboratory was commissioned, and x-ray fluorescence experiments were performed. Technical improvements and new equipment in development will increase the range of experiments possible. For example, we are designing and fabricating a fluorescence cell that can be used in the ultrahigh-vacuum environment of the synchrotron radiation beamlines and analyzers, yet will still permit the introduction of "wet" or partially hydrated mineral samples. This device includes a thin x-ray transparent window that allows the excitation radiation into the cell and concurrently permits the passage of fluorescence x rays out of the cell and into the detector.

Fourth, sample preparation techniques were developed at LLNL, allowing the production of well-characterized actinide–mineral sorption systems for experiments at SSRL and ALS. Systems to be studied include uranium and thorium sorbed on layered silicates, zeolites, and carbonate minerals. X-ray diffraction and particle-size measurements on mica samples were used to determine the optimal mineral preparation techniques. Several micas were exposed to uranium in solution, and based on that experience, more extensive sorption experiments were designed.

Publications

E. A. Hudson and J. J. Rehr (submitted), "XANES Spectra of Uranium Compounds Calculated by High-Order Multiple-Scattering," submitted to the Eighth Int. Conf. X-Ray Absorption Fine Structure.

Author Index

B

Balooch, M., 6, 69
Barbee, Jr., T. W., 75
Bedrossian, P. J., 9, 12

C

Campbell, G. H., 52
Chaiken, A., 78
Chapline, Jr., G. C., 75
Chase, L. L., 2
Comsa, G., 9

D

Diaz de la Rubia, T., 80
Dresselhaus, M. D., 75

E

Elmer, J. W., 38

F

Farmer, J., 75
Foreman, R. J., 75
Fröba, M., 38

G

Gallegos, G., 32
Gonis, A., 21, 44, 46, 48
Gourdin, W. H., 17, 21
Gregorich, K. E., 92
Guinan, M. W., 80

H

Hall, H. L., 92
Hamza, A. V., 6
Henshall, G. A., 18, 20, 83
Hicks, L. D., 75
Hoffman, D. C., 87, 90
Hudson, E., 93

J

Jankowski, A., 68
Johnson, P. E., 21
Jorritsma, L., 9

K

Kanna, R. L., 26
Kaschmitter, J. L., 65
King, W. E., 52
Kinney, J., 70
Kioussis, N., 21
Kreek, S. A., 92

L

Lipkin, N. N., 9

M

MacLaren, J. M., 44
Matthews, M. J., 75
Mayer, S. T., 65
Michel, R. P., 78
Mitchell, A., 30
Moalem, M., 6

P

Pagoria, P., 30
Pekala, R. W., 65
Poelsema, B., 9
Pruneda, C. O., 26

R

Rosenfeld, G., 9

S

Schmidt, R., 30
Schwartz, A., 32
Seikhaus, W., 69
Silva, R. J., 90

Simpson, R. L., 25
Singh, P. P., 46
Smith, P. M., 21
Souers, P. C., 60
Sterne, P. A., 3, 48
Stoyer, N. J., 90
Strum, M., 18, 83
Summers, L. J., 75

T

Tamura, E., 3
Terminello, L. J., 72, 93
Tobin, J. G., 3
Tran, T. D., 65
Turchi, P. E. A., 50

U

Upadhye, R. S., 26

V

van Ek, J., 44, 48

W

Waddill, G. D., 3
Wagner, A. V., 75
Waide, P. A., 38
Watkins, B. E., 26
Wien, W., 52
Wong, Joe, 38